2018

Residual Stresses Analysis of 3D Printed Plate By using Wire Arc Additive Manufacturing -WAAM-

Abdulrahman Amer Alrumayh
Lehigh University, aaa216@lehigh.edu

Residual Stresses Analysis of 3D Printed Plate By using Wire Arc Additive Manufacturing -WAAM-

by

Abdulrahman Alrumayh

A Thesis

Presented to the Graduate & Research Committee

of Lehigh University

in Candidacy for the Degree of

Master of Science

in

Mechanical Engineering

Lehigh University

August 2018

This thesis is accepted and approved in partial fulfillment of the requirements for the Master of Science.

_____

Date

_____

Thesis Advisor

Herman F. Nied

_____

Chairperson of Department

D. Gary Harlow

Acknowledgment

My thanks go firstly to my parents and my family for their support through my life.

After them, the thanks must be for my teachers and professors through my learning path even who taught me a letter.

My successes and achievements are their efforts outcomes, so thanks for them from bottom of my heart.

I would like to thank especially my supervisor Professor Herman F. Nied for his support, guidance, and understanding through my master program.

Table of Contents

List of tables

List of figures

Abstract

Additive manufacturing represents a relatively newly developed technology with many rapidly changing innovations . One of the most important processes in additive manufacturing is 3D printing. For a couple of decades, polymers have dominated the materials used in 3D printing. In the last few years, 3D printing of metals has had a high impact on interest in this technology. One 3D printing process that uses metals is Wire Arc Additive Manufacturing (WAAM). This technique has some technical obstacles that may detract from its use in commercial applications. One of the crucial issues concerns the control of residual stresses and related distortions. The evolution of residual stresses can theoretically be simulated by using computational software for the WAAM process, in a manner similar to welding process modeling, using nonlinear finite element codes such as ABAQUS, ANSYS, SYSWELD, etc. This study focuses on using SYSWELD to model the WAAM process.

In this thesis, the key reference problem is the simulation of the WAAM process for a vertical 3D printed plate. This “reference” problem was chosen because =WAAM printed plates have been fabricated at Lehigh University and thus, comparisons can easily be made between simulations and experimental measurements. The simulated WAAM parts examined in the study compare two types of steel alloys: 1) austenitic stainless-steel grade 316L and, 2) Low carbon steel S355J2G3. The residual stress components of particular interest were determined to be: 1) Longitudinal stresses across the width of the plate and, 2) the maximum principle stress. The distortion of the WAAM plate after the metal deposition processes are complete illustrate the difficulty in maintaining dimensional tolerances. The simulation process predicts higher residual stresses and lower distortion for the low carbon steel alloy, when compared with the austenitic stainless steel.

Chapter 1 introduction

Additive Manufacturing

3D-printing is a trending method of manufacturing that presents researchers with a myriad of promising outcomes as well as challenges. 3D-printing has gained enormous attention recently and is perhaps the break-through technology of this manufacturing era – just as the steam engine and combustion engine once were. 3D-printing is also known as additive processes, or additive manufacturing [1]. The Principle of Additive manufacturing starts many years ago when mankind started to build houses, for example building walls uses additive manufacturing in large scale using stacked blocks. The wide difference in the materials used in additive manufacturing, or building, and the variety of designs and properties of the materials, made it hard to precisely define 3-D printing, at least until 3D CAD was developed. Powerful 3D CAD software now makes it easy to build a shape for virtually any desired shape and specified material properties [2].

History

The history of additive manufacturing is not new; in fact, the concept of additive manufacturing started by using photo sculpture back in the 1860s, which was further developed later [3]. It started with the concept of building layer by layer in the early of 1900's , "back to Peacock for his patented laminated horse shoes in 1902" [4]. About a quarter a century later, Baker patented "The use of an electric arc as a heat source to generate 3D objects depositing molten metal in superimposed layers" in 1926 Figure 1.1[5]. He used a new technique to build a 3D object , which had not yet been employed, by using welding processes [6]. So, this attempt could be considered as the oldest attempt to use welding technology in additive manufacturing, which is known later as Wire Arc Additive Manufacturing WAAM.

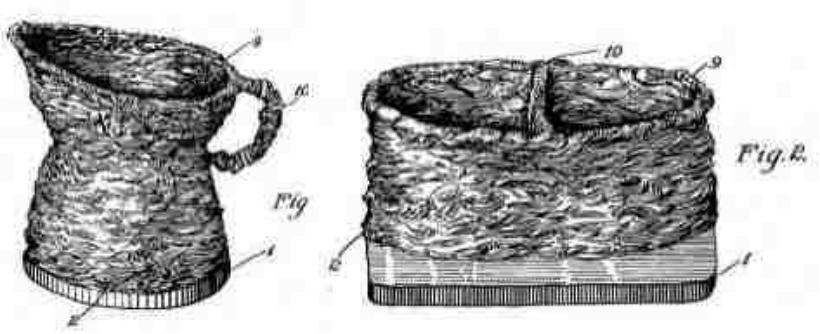

Figure 1.1 : Baker's models in 1926 using molten metal [5].

After 25 years in 1951, a new technique was patented ''Photo-glyph recording'' technique[3]. In 1952, Kojima indicated the importance of layer-by-layer processes, and in the next 30 years, many patents were filed related to 3D printing processes by using layer-by-layer techniques. The more modern patents and new research were based on the 1950s' principle[4] of 3D-printing. In the 1960s, and after, many attempts were made to use a laser to solidify specific points on a polymer sheet, these attempts were not used until they were developed with other techniques. Later in 1987, Stereolithography (SL) for 3D was established, which used a laser to solidify thin layers of light-sensitive ultraviolet liquid polymer[7].

Definition

ASTM defines additive manufacturing as the "process of joining materials to make parts from 3D model data, usually layer upon layer, in contrast to subtractive manufacturing and formative manufacturing methodologies" [8]. This definition makes the concept of additive manufacturing very broad, so as to include many processes, not just 3D printing. Also ASTM "specifies other commonly used synonyms for AM (additive manufacturing) including additive fabrication, additive processes, additive techniques, additive layer manufacturing, layer manufacturing, and freeform fabrication" [9].

Importance and Promise able Future

In recent years, AM has received considerable attention from many institutions and research centers around the world. One of the best aspects of AM is the potential for zero waste during the manufacturing process, which will likely reduce costs [10]. Traditional manufacturing processes for complex parts can often be quite expensive and may not offer efficient solutions for the manufacturing of complex shapes. AM potentially offers an inexpensive solution for complex manufacturing problems [11]. Another crucial point is AM has the ability to repair and fix broken parts. Furthermore, it has the ability to collaborate with conventional manufacturing processes[12]. AM has another advantage that distinguishes it from other manufacturing processes, which is the ability to deal with most kinds of materials: polymeric materials, composites, ceramics, and metals. Of course, traditional manufacturing processes will never be completely displaced by AM, but for a large class of applications AM may provide the most effective manufacturing solution [13].

Cost and mass production are very important in nearly all industries. AM offers a sort of balance between cost and mass production. On the other hand, traditional manufacturing has an inverse relationship between cost and volume, which makes traditional methods much cheaper than AM Figure 1.2 when a large number of identical components are being produced. In contrast, complexity of the product often makes traditional manufacturing more expensive than AM Figure 1.3 [12].

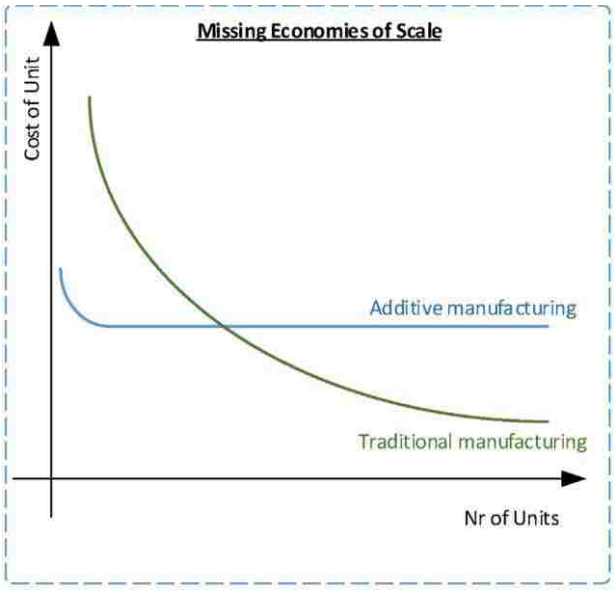

Figure 1.2 : Relationship between the cost and Number of products for AM and traditional ways[12].

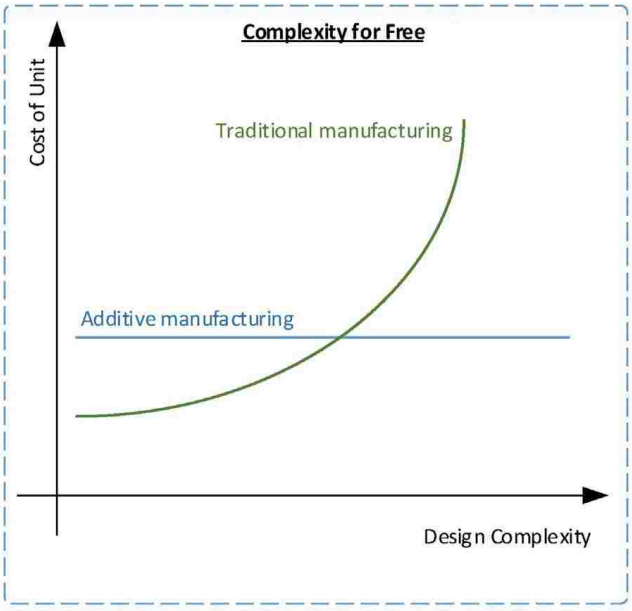

Figure 1.3 :Relationship between the cost and design complexity for AM and traditional ways[12].

Throughout the last thirty years, AM research has grown exponentially. Nowadays, AM is the subject of, or included in a variety of, research topics [4]. AM has huge economic impacts as well; Wholers report [14] mentioned that the AM market could reach $7 billion by 2019. In the past, AM has had a high growth rate of approximately 26% [9], also AM is expected to grow

continuously through the years. AM is sometimes called the “third industrial revolution”, because industries and factories are starting to use AM in the manufacturing of their products on a large scale. Some AM techniques are available commercially, such as 3D by laser or electron beam deposition. But some additive processes are still not commercially available, e.g., WAAM (Wire Arc Additive Manufacturing), which still has some technical challenges such as residual stresses, deformation, microstructure grain, and low quality of surface finishing. These challenges directly related to the enormous heat input [15] associated with an electrical arc. One may also consider the protection of the existing patents and trademarks as obstacles for some of the additive technologies to be commercially available [16].

Overview 3-D Printing

3D printing, or AM, provides the user more freedom to fulfil the desire of the consumers in many aspects of the manufacturing process, such as volume, cost, weight, design, and properties[17]. 3D printing in a simple definition is a way of joining many elements by using heat source to melt and join. 3D printing has different techniques, which depend on the heat source, feeding technique, and feed material. Most feeding systems use blown powder, powder bed, and the wire feed techniques, and the heat source is typically a laser, electron beam, or electric arc [10]. However, other techniques also exist, such as selective laser sintering, direct metal deposition, electron beam freeform fabrication, shape deposition manufacturing, wire and arc additive manufacturing (WAAM), etc.[18].ASME includes many types in their classification for AM technologies. ASME has created seven categories for the types of AM using metal and other materials : (1) material extrusion, (2) powder bed fusion, (3) vat photopolymerization, (4) material jetting, (5) binder jetting, (6) sheet lamination, and (7) directed energy deposition[3]. Concerning metal applications, directed energy deposition can be divided into two subcategories of feeding, powder and wire. The wire feeding system could be used with a different heat source,

but the simplest system uses an electric arc heat source and is designated WAAM. WAAM is efficient for large size components. Also, it is considered the lowest cost and safest method with a high metal deposition rate. As a comparison, WAAM can attain deposition rates of 50-130 gram/minute, whereas powder-based systems can only offer 2-10 gram/minute. WAAM is essentially a multi-pass welding process, utilizing one of the most common welding techniques, i.e., GMAW (Gas Metal Arc Welding) [15]. For metal applications, titanium and its alloys, steel, aluminum, and nickel alloys are typically used in WAAM processes. Despite the benefits of AM, some of the techniques have defects and issues, such as the residual stress and the surface finishing. This leads to poor quality of the mechanical properties of the desired product[14]. Overall, AM is a manufacturing process that uses continuous heat input localized to a specific feeding material to change its matter from solid to liquid for a specific size in the melted pool. In order to be solidified in a certain shape that makes the final design of the deposited layers[19].

Polymers are the most dominant materials used in AM, because of their low melting point and high viscosity, which assists with the layer-by-layer deposition process. However, the metal AM developed techniques increase the portion of metal AM application in the market.[17].

Metal 3-D Printing

This thesis focuses on metal AM, especially on WAAM. As mentioned previously, metal AM can be divided into two categories and each category has three main sections. The two categories are the feeding system and the second is the heat source. The sections of the feeding systems are powder bed, powder blown, and wire. And the heat sources are laser, electron beam, and electric arc. Electric arc AM is the main subject in this research. The performance of metal printers is based on the final products' residual stresses, distortion, microstructure, and mechanical properties [20]. Also, the feeding systems have been divided into two main types, direct and

indirect deposition systems. The direct deposition system melts all the particles to obtain the final design, while indirect systems use a binder to join particles [21].

The deposition efficiency of wire-based AM is higher than other types, for example wire based AM deposition efficiency can approach 90%, while in powder-laser is around 40%[22]. That gives some credit for wire feed systems. deposition efficiency is calculated by the amount of metal is used vs the amount of metal is remain after the processes.

Powder Bed

Powder bed uses a container full of powder that allows the heat source to melt layer by layer. Between two layers, the container moves down to allow for an out slide to feed more powder [23]. This yields a new powder layer above the old melted one as shown in Figure 1.4.

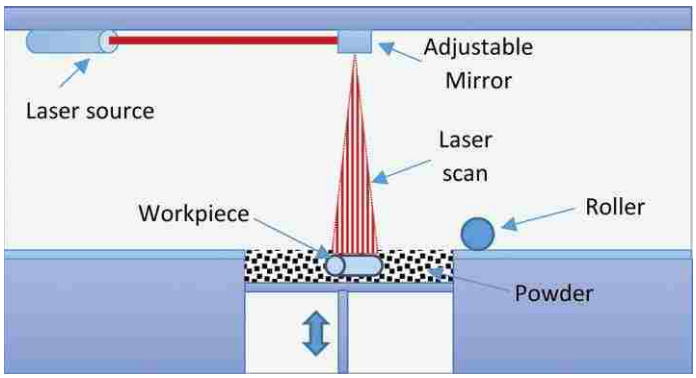

Figure 1.4 :diagram shows powder bed with laser[24]

Powder bed uses either a laser or electron beam as a heat source, because of their accuracy and precision. However, powder bed is best suited for small-sized products, since the size depends on the container itself [10] and because the deposition rate is low for this technique. The larger commercial size powder bed-based AM is around 0.16 m^3 with deposition rate of 0.2 kilogram/hour[22]. Powder bed processes utilize several deposition techniques, which include ALM (Additive Layer Manufacturing) , SLM (Selective laser melting) , DMLS (direct metal laser

sintering) , DMLM (Direct metal laser melting) [25]. Some of these processes, e.g., LM (Selective laser melting), have issues with the fast cooling rate, which cause distortion in the final product [26].

Powder blown

Powder blown was used as a welding manufacturing process even before its application in AM. This process uses a nozzle to blow powder to a certain area where the heat source focuses on this area, so that the heat melts the powder as shown in Figure 1.5.

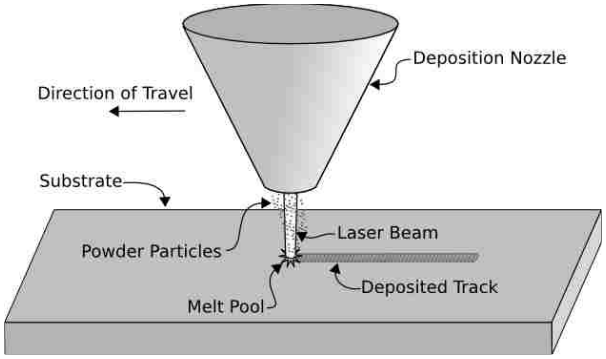

Figure 1.5 :diagram for powder blown system with laser heat input [27]

As in powder bed, blown powder has different techniques such as DLMD (Direct Laser Metal Deposition), LMD (Laser Metal Deposition), LENS (Laser Engineered Net Shaping) [25].

Wire Feed

The third AM metal feeding system is wire feed, which is considered the most efficient system in terms of materials usage. Moreover, it is considered the cleaner and safer for the environment in addition to the low cost [28]. Of course, the wire feeding system is not a hazard to the atmosphere, in contrast to powder processes [29]. The wire feed system as shown in Figure 1.6 uses the same principle as the powder blown system, i.e., the feeding materials are blown or deposited by the feeder in the interest area where is the heat is applied [30].

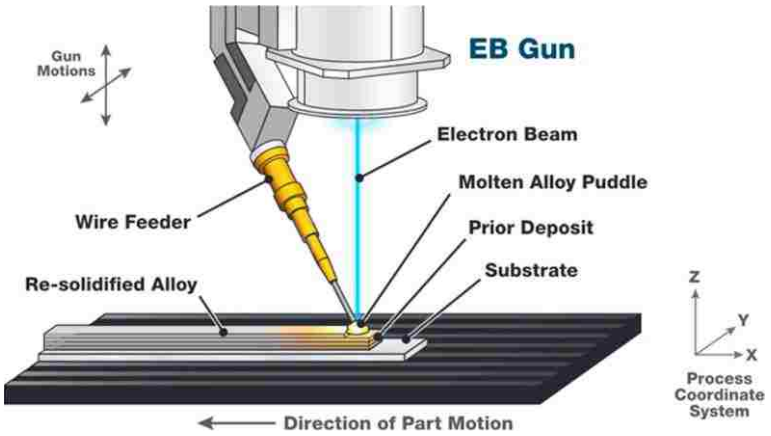

Figure 1.6 : diagram of wire feed system with electron beam heat source[31]

There is plenty of research that has studied wire feeding systems in welding processes. But AM uses this process repetitively many times in one product, and this is the primary difference between welding processes and AM. The AM deposition process is simply a multi-pass welding process. In contrast to the previously discussed AM processes, wire feeding systems have the lowest accuracy because the diameter of the wires are larger than the size of the powder in other processes, so it is hard to build a very intricate product using a wire feeding system[19].Heat source power types

AM uses a variety of heat sources and joining processes to build a product. However, metal-based AM typically uses a laser for the heat source, as well as an electron beam or electric arc. Each one of these is used in certain applications, depending on the desired product.

Laser AM is most popular and can be used for the three aforementioned feeding types. In addition, laser processes have a high accuracy, around 20 µm, which gives it an advantage [32]. On the other hand, laser AM has a fast cooling rate, which can introduce defects in the final product [33]. Furthermore, laser AM has poor energy efficiency compared to other processes, around 5% [34].

The fundamental principle behind electron beam AM is that an electron beam ,i.e., a stream of electron, passes through the feeding materials. Electron beam AM is more efficient in energy term than laser AM, around 20%. On the other hand, it has disadvantages that make the process cost more, e.g., electron beam AM requires a vacuum environment. Although, some consider this to be an suitable for aerospace applications since the vacuum environment is already exist [34].

Electric arc systems also use the same principle as electron beam AM, but there is a slight difference between the electric arc and the electron beam AM regarding the lower energy density heat source. This difference makes the melting rate lower than electron beam and laser systems [35]. The energy efficiency of the electric arc in certain circumstances can be as much as 90%, as in gas metal arc welding (GMAW) or gas tungsten arc welding (GTAW) processes. Further, electric arc AM is capable of handling large-sized products[28]. Electric arc and wire feeder AM can be combined, which is called WAAM. WAAM has a high deposition rate, lower system and material costs, and a lower probability of oxide contamination [34] [36].

WAAM

WAAM (Wire Arc Additive Manufacturing) offers a promising area for research and has many advantages. WAAM is often favored over electron beam and laser systems. The main reasons for this are the cost, the vacuum environment, easier operation, and non-reflectivity problems [37]. The most frequently employed techniques used in WAAM are Gas Metal-Arc Welding (GMAW) and Gas Tungsten-Arc Welding (GTAW). These methods have a high deposition rate and the ability to build large and small products, up to few meters[38]. Further, compared to traditional manufacturing processes, these methods efficiently use raw materials[11]. Unfortunately, it is generally conceded that WAAM processes can introduce enormous residual thermal stresses; which is usually not the case in powder bed systems [39]. WAAM is based on the welding process.

However, automation of the WAAM process is what has significantly increased printed product quality. Figure 1.7 illustrates two diagrams of GTAW and GMAW. Both processes use electric arcs that are created by applying an electric potential between the base metal and the welding electrode; in GTAW the electrode is non-consumable, while in GMAW the electrode is the feeding material. The melting pool is protected by an inert shielding gas. The processes are operated by a robot, so the feeding rate and heat input are systematically controlled and there is a high deposition rate – up to 10 kg/h [40].

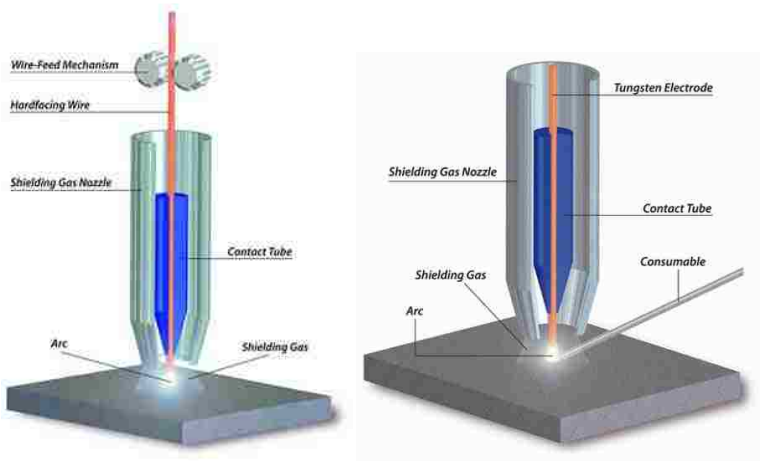

Figure 1.7 :diagrams describe GMAW (left) and GTAW(right) welding processes[41]

WAAM has not received the same attention as other AM technologies, because of the unresolved technical problems described in this chapter. Further, it is important to mention that WAAM has poor accuracy around ±0.2 mm vs ±0.04 mm for powder based, one of the reason is the size of the melting pool , and high distortion effects that render WAAM unacceptable for many manufacturers [30].

WAAM is a type of welding process, so the parameters relevant to the welding process are equivalent.

The most important parameters are the arc voltage, arc current, shielding gas, nozzle-base distance, travel speed, feeding speed, and wire diameter. These parameters effect the weld bead geometry, resultant distortion, and resultant residual stress[42]. For example, variation in the distance between the nozzle and the base leads to poor shielding quality and introduces deposition defects, or creates a spatter areas on the product [43]. In addition, the high deposition rate leads to a thicker bead, which affects the microstructure grain patterns growth, since the thicker bead needs more time to solidification processes[44].

Advantages

WAAM impacts the environment by 70% less than traditional machining impacts on the environment such as raw material extraction issues, recycling ability[9]. WAAM has the potential to be a non-waste technique through development of the process toward ready-to-use products, especially for mechanical properties and surface finishing [37]. In addition, WAAM is an easy system to build and supply.. Considering costs, a WAAM system is still one of the cheapest AM technologies. Moreover, WAAM is suitable for building small or large sized products with medium complexity[42]. In certain situations, a thermal gradient causes a tendency towards anisotropic material properties [45].

Disadvantages

Despite its advantages, WAAM is considered to be an unsuitable technology for some applications. Since the diameter of the wire is large compared to powder systems, the accuracy of WAAM is lower than powder (±0.2 m-wire, ±0.04 mm-powder). For complex products, WAAM may not a great choice for manufacturing [42]. WAAM has a high heat input with thermal concentrations in certain areas, which leads to deformations and may cause cracks. This is due to thermal gradient effects [46]. WAAM works using the same principles as EB, where electrons

are transferred to the work area. However, WAAM has a lower energy density than EB or laser AM with a slower rate of transferring. This causes larger melting pools than in other AM processes and techniques. The melting pool for WAAM is affected by fluid flow effects, which controls the shape of the melt pool and initiates its penetration. These considerations must be accounted for in order to obtain good surface finish and uneven ends of the final geometry [35].

Applications

WAAM machines are currently not commercially available because of the shortcomings described above[18]. Nevertheless, WAAM is greatly developing in aerospace, biomedical, automotive, and energy applications [32] [21]. Also for printed parts, there some companies has successfully printed a verified and tested parts by using WAAM , such as Damen Shipyards who announce a 3D printed boat propeller as appear in Figure 1.8 [47].

Figure 1.8 Ship propeller has been made by Damen Shipyards[47]

Metal 3-D Printing Issues and Challenges

In order for AM to be widely implemented in society, it must meet the expectations of the consumer and stand up against economic barriers. Unfortunately, there are obstacles preventing AM from replacing traditional manufacturing processes. Many of these problems are related to a lack of fusion, porosity, vaporization, mechanical properties, grain structure, surface finish,

deformation, residual stress, cracking, and uneven geometry.[10] Some of these issues are the result of thermal effects, which could be solved by a heat treatment [9].

Porosity is a common defect in welding processes, including WAAM. Porosity refers to any unwanted cavity inside the work piece. Typically, these unwanted porous defects are caused by gas trapped inside the work piece during the welding process that is unable to escape prior to solidification. Poor control of the shielding gas often results in unwanted porous defects. Other reasons for such defects are raw material impurities and insufficient flow rates. Regularly, cavities occur near the edges of the molten tracks. As porosity increases, material properties such as ductility, strength, and stiffness decrease[8] [48]. Figure 1.9 illustrates a porous area, whose defects formed during the welding process for an aluminum alloy involving only a single pass.

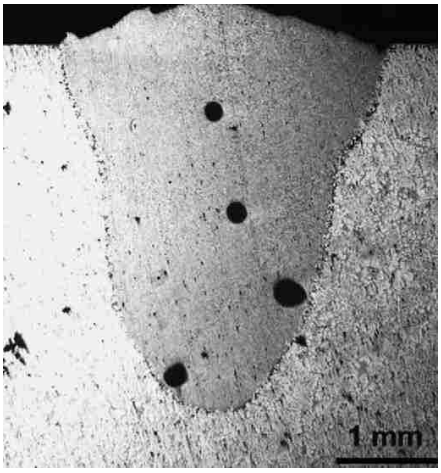

Figure 1.9 :Porosity defects for an aluminum alloy[49]

The quality of the weld bead profile is a common controllable issue, caused by three main factors: humping, undercutting, unsymmetrical beads. Humping refers to an uneven bead profile in the direction of the welder, which causes ups and downs on the layer. Undercutting and unsymmetrical beads refer to the bead located in an undesired position or having an undesired shape. Undercutting occurs between the two different layers, or the base, while unsymmetrical

bead occurs for a single bead. These issues are usually caused by a high travel speed and with an uncontrolled deposition. As a result, any missed spot will affect subsequent layers, which results in defects in the final desired product[48] [50]. With GMAW, the profile assumed at both ends of a square plate, built by AM, assume a different shape than the middle of the plate. This is caused by the shape and depth of the weld penetration, which causes differences in the thermal distribution, which in turn leads to sloping at the end and humping at the start [15]. Figure 1.10 shows the unbalanced endings, which are created by thermal distribution and surface tension effects.

Figure 1.10 :a plate AM based, start(right) , end (left) [43]

Grain structures contribute in the cracking behavior in the work piece, which are dictated by the thermal distribution while cooling. Shrinking leads to crack formation at the grain level. Furthermore, shrinking occurs when high thermal gradients are present, which leads to a high cooling or heating rate. Generally, materials with low ductility are the first to exhibit cracking. Chemical degradation and oxidation are two more minor issues relevant to AM for metal applications because they are easily controllable, [8].

Deformations and distortions are very common issues in welding. Thermal gradients cause deformations that eventually may lead to cracking. We know from the basic principles of thermal expansion that most materials shrink upon cooling and expand upon heating. So, when these cases happen at a certain spot, then distortion occurs at this location due to differences in the local thermal stresses. Figure 1.11 shows a concaved work piece. Clamping temporarily stops deformations, but heat treatment is required for a more complete solution[8].

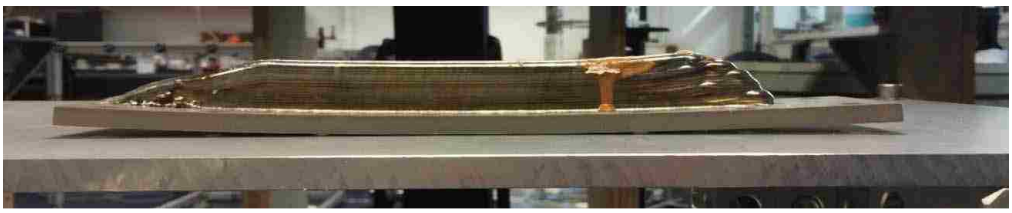

Figure 1.11 :3D printed work piece is concaved[41]

Poor surface finishing is a concern for most AM technologies. Usually powder feeding systems are concerned with the coarse surface; while in wire feed systems the surface is fine. Interestingly, the sides form a sort of sinusoidal surface, like what happened in the side of the shown piece in Figure 1.10. Moreover, coarse surface could happen in WAAM if the shielding gas is inadequate or welding parameters are inappropriate. Usually, the solution for a good quality surface finish requires traditional machining processes[8]. Figure 1.12 shows undesirable and uneven sides of an AM work piece, i.e., it needs further processing prior to its use.

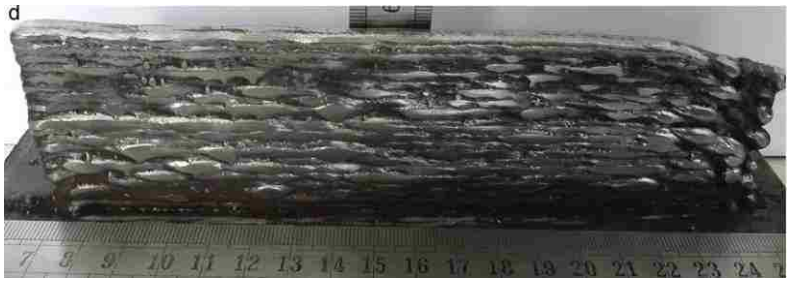

Figure 1.12 :Poor profile caused by uneven bead[13]

Of critical concern in WAAM are the welding residual stresses, which are associated with distortions in the finished work piece. Throughout AM, the first layers are reheated several times, due to the heat of subsequent bead layers. This induces a thermal cycle for each layer, which ends on the final layer or by steady cooling rate[51]. WAAM, as mentioned, is a high heat input process, which makes the affected zone large and may lead to shrinking in the affected areas. If the thermal gradients are large enough, and the workpiece is sufficiently constrained, the residual stresses will be high. In some cases, the internal stresses are relieved when the work piece is unclamped. Usually, the largest residual stresses arise in the direction of the deposition[50]. There are two residual stress states of particular interest. The first is the residual stress state immediately after the manufacturing process is finished, but before the part has completely cooled The second residual stress state is the final state after the work piece has been cleaned up and cooled [34].

Experimental Processes

CAD technologies have revolutionized manufacturing at large, and is responsible for the accuracy of AM. The first step is product design using CAD software. Then the design transforms to an acceptable file for the various slicing software such as STL files or G-code files to be rendered as 2D layers [52] [53]. After that, slicing software slices the design into special properties for the layers (layer dimensions, slice thickness, etc.) [39]. Then, using the new layer shapes, the software creates path trajectories (such as raster, zigzag, contours, etc.) to build each layer by using the digital information[18]. And the final step is a robot follows the paths and prints [37]. In WAAM systems, usually GTAW and GMAW are used so any system must contain (CAD software, slicing software, path software or tool, deposition controller (robot with multi-degree of freedom), heat source, materials supply) [37]. Typically, the controller regulates the power and heat input such that the process results in the deposited layers exhibit the desired material

properties. The travel speed and the distance between the nozzle and the substrate can also be controlled to obtain the desired final product. In many applications of 3D printing of metal materials, there are two types of area characterizing the work piece: the total area and the effective area. The effective area is the desire area, while the rest of the total area must be removed to clean the effective one. For certain cases, 90% of total area is the effective area, while the remaining surface material must be removed. As shown in Figure 1.13 the substrate and the first few layers are removed intentionally to obtain the desired surface finish[12].

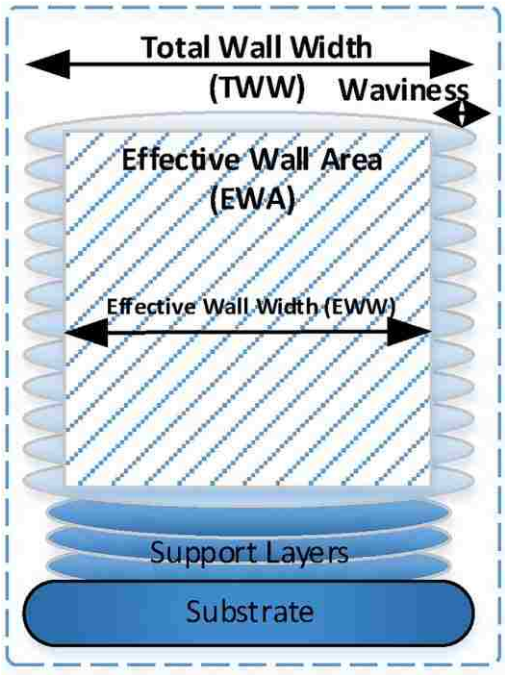

Figure 1.13 :A diagram shows the effective area as part of the total area[12].

Simulation Software

Recently, software has made it easier to simulate many AM processes by using numerical analyses based finite elements methods (FEM). Many approximations are made to model the real physical system, of course[54]. For welding manufacturing processes, common software packages are SYSWELD, ABAQUS, and ANSYS. SYSWELD is a specialty heat treatment and welding process software that uses numerical analyses such as FEM, to simulate the actual process at a relatively high level, up to three spatial dimensions[55]. "SYSWELD can obtain: temperature fields and thermal fluxes, phase proportions, hardness, distortions, residual stresses, and plastic strains distributions" [56]. Since AM is based on a well-known welding process, we can use these commercially available software packages to model and simulate AM processes in order to study mechanical properties. AM requires control of process parameters more than traditional processes[3]. Using such software in order to predict residual stresses and deformations saves time and money. The degree of accuracy predicted by the software is closely related to the computational time required, but generally speaking all of the aforementioned software packages yield reasonable results[6]. Figure 1.14 shows the actual and the predicated shape for a t-tube joint obtained from SYSWELD after a welding and loading process [57]. The accuracy of the SYSWELD software for estimating post-weld stresses and distortion is generally considered to be quite good.

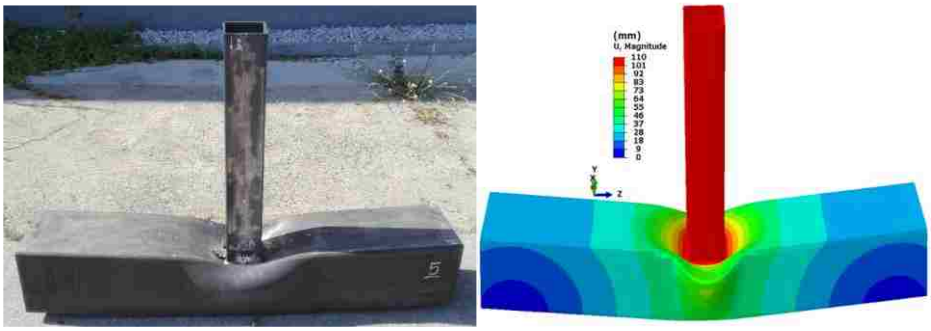

Figure 1.14 :A comparison between experimental (left), and computational (right) [57]

Residual Stresses Curing Researches

Lehigh University has WAAM capabilities and is being used for research studies in this AM technology. Haden and others said, “The 3D metal WAAM printer at Lehigh University is currently configured with a Millermatic 250 gas metal arc welder (Miller Electric Manufacturing Co.) and a roughly 0.53m Cartesian gantry positioning system (Macron Dynamics, Inc. and Parker Origa OSP-E25). The welding nozzle position is determined from CNC commands derived from a computer aided design (CAD) rendition of the desired part. The part is converted using open source software Slic3r engine (slic3r.org) to GCODE which dictates motion commands to the microcontroller.” [58]. The two biggest challenges for Lehigh University and others in the field are the residual stresses and distortions obtained from WAAM processes. These two challenges are present due to the large thermal gradients present during the WAAM process.

In the past, thermal simulated models for arc welding did not consider convection heat transfer as a main part of the cooling rate for welding processes, despite its huge importance in arc welding processes, especially in the melting pool [59]. However, the available FEM software packages simulate the welding process with accurate results; so large heat input with high thermal gradients produce high residual stress and distortion [60] [61] [62]. Since deposition layers are cyclically reheated, some research aims at fixing the sequences of this process by using adjacent droplets numerical models and to simulate the real physics of welding, which is the metal contact to the base as drops[63] [64] [65]. Additionally, the substrate conducts heat, so the shape and condition of the substrate will have significant effects on the performance of the layers deposited and the resulting surfaces. Any defect in deposition will be magnified during deposition of the subsequent layer[15]. Many studies have focused on the thermally-driven residual stresses and distortions, although geometric simple differences between the simulated and real part does not considered [66].

One study revealed that the last few layers of any AM deposition process have high hardness because they experienced less cyclic reheating[67]. It was determined, the residual stresses effect of the final deposited layer does not exceed five layers. It is proposed that the thermal cycling results in softening and annealing for nearest layers [67] [58]. Thermal recycling is the reason for the high residual stress and deformation in AM [68].

In order to mitigate these undesired outcomes, there are three stages of processing: pre-processing, online processing, and post-processing. The best strategy for reducing the distortion is by using clamping and building strategies, while online strategy (rolling) has a high impact on residual stress.[69] [70] [71] [6] [48].

Some research examined pre-bending as a way to reduce residual stresses and distortions in welding processes[72] as well as to reduce thermal and mechanical tensioning [73] [74] [75] [76]. Optimized deposition sequences are also used to reduced distortion in welding [77] [78] [79] and AM [80] [81] [82] [11]. Others researched have reported achieving zero net distortion by preheating the weld area prior to deposition[83]. Other researchers have reported similarly – preheating the substrate alone reduces distortion in AM processes [84] [85]. Further, heating the substrate prior to deposition decreases residual stresses[11].

Since multi-pass welding is almost identical to WAAM, it is probably acceptable to use mitigation processes from welding in WAAM processes, and reducing the heat input is a significant factor in reducing deformation in multi-pass welding processes[86]. Also, mechanical constraints have the ability to change the final deformation[87] . Moreover, surface quality could be changed by reducing the heat power input or increasing the velocity of the deposition. [13]. Welding processes employ many techniques to control heat input through the introduction of a double heat source (electrode) [88] [89] [90] [91]. Cooling the layers to $50^{O}C$ after each depositing

process significantly reduces residual stresses after the clamps are removed, the cooling process could be better controlled by introducing a waiting time between layer deposition [6].

One of the way to reduce residual stresses online is by using induction heating as a second heat source to follow the deposition process [92]. A high pressure rolling line is also a successful way to reduce residual stresses [10]. Since one of the reason for the residual stresses is the grain structure [12], the rolling enhances grain refinement. Rolling reduces enormously the peak of longitudinal residual stresses [69]. For different metals, path tracks have been studied and the effect of reduction in residual stress and deformation has been demonstrated[81] [93]. It has been reported that one way to reduce residual stresses is through layer deposition in reverse directions, which refers to the high heat diffusion[94] [95] [20]. In order to reduce residual stresses and deformations, one solution is to deposit continuously without any period of cooling time [96], [97]. However, this method leads to high heat input in some locations that induces poor surface quality [98]. It has been shown with different materials that incorporating time delays between layer deposition allows for better cooling of the layers, which reduces distortions and residual stresses[84] [99] [100]. Introducing time delays between layer depositions changes the microstructure significantly [101] [102]. A study showed the effect of controlling temperature through the use of an infrared thermometer on the mechanical properties and surface quality[103]. Other researchers used a passive vision sensor system to control deposition process parameters in order to obtain the desired surface qualities[104] [105]. Others tried to increase GMAW AM accuracy by controlling the deposition process factors in an automated weld-based rapid prototyping (RP) system [106] [107].

In order to improve surface finish, some researchers combine AM processes with traditional milling processes [108]. “Bai et al. (2013) [109]developed electromagnetically confined weld-

based additive manufacturing to build overhanging structures or tilt structures at a large slant angle."

Thesis Statement

Residual stresses play a huge role in creating the defects and the distortions that have been observed during the 3-D printing process. It would be very useful if residual stress can be accurately predicted in order to prevent or reduce the effects of these stresses. Since WAAM uses arc welding for printing, it is obvious that simulation software for welding processes could accurately simulate WAAM. Lehigh has made many samples using an experimental WAAM machine, so in this research, one model will be studied and simulated using SYSWELD; the goal is to observe the residual stress and the distortion of 3D printed plates by using simulation software (SYSWELD). The materials used in this research are: 1) austenitic stainless steel 316L and, 2) low alloy carbon steel S355J2G3.

Chapter 2 Simulation setup

Experiment

Lehigh has made many 3D printing samples of WAAM using the machine which was previously described, one of them was done by Prof. Haden, Gordon and their group. Gordon has made and tested a 3D printed 304 stainless steel plates for Fatigue crack growth and Microstructural characterization. Also, he repeated the tests after heat treatment. For fatigue test, he took samples from horizontal and vertical orientation[110]. As shown in the picture below Figure 2.1, this is the 3D printed part of the sample using welding process as WAAM. Also, it is clear the distortion of the base metal is due to the stress of the printed part.

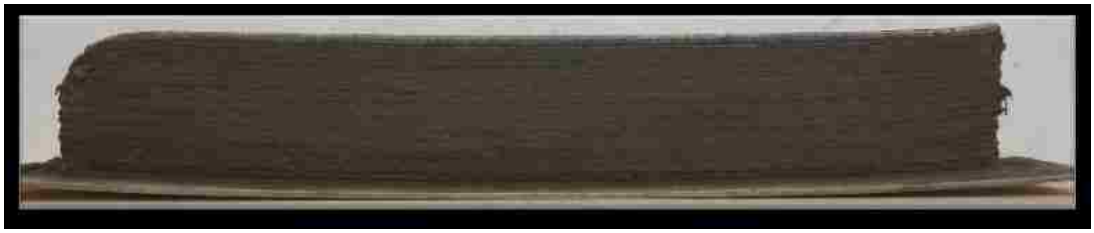

Figure 2.1 : The experiment sample after it cooled

Additionally, some milling and cutting are done on 3D printed part to get the fine area. Figure2.2 shows the length with both sides; from this figure, it is clear the distortion of the base plate released some of the residual stress after it was cut from the substrate. Figure 2.3 shows the two ends of the printed part, they are cut from the original part because they have higher rate of distortion as appear

Figure 2.2 : The experiment sample after machining

Figure 2.3 : Two ends of the real sample (start welding, right) (end welding, left)

This sample was printed with the welding parameters, as shown below in Table 2.1

Table 2.1 welding parameters for AM in Lehigh Lab

Wire feed rate	voltage	Substrate Type	welding speed	Wire Type	Shielding Gas
9.3 mm/s	22V	Stainless Steel Grade 304	2.54 mm/s	ER308L	90% He, 7.5% Ar, 2.5% C02

Number of layers	Layer length	Layer Height	Layer Thickness	Substrate Dimension
38 Layers	670 mm	1.778 mm	6.35 mm	5 X 101 X 762 mm

Figure 2.4 shows the cross section of the beginning cut. It is clear from the figure the cutting process does not leave any impression of layers on the cross section of the sample. The height of the sample is around 95 mm. and the width around 0.39 inch = 9.9mm (which are the extreme parameters of the sample).

Figure 2.4 : Dimensions of the cross section (height on left and width on right)

Since the goal is to perform a welding simulation process, it is important to observe the shape of each layer by conducting electric etching process. Before drawing the shape of layers into the simulation software, the part of interest needs to be suitable for photographing by cutting the appropriate part, as seen in Figure 2.5 with red lines. After the cutting process and before the etching process, it needs to be mounted, grinded and polished.

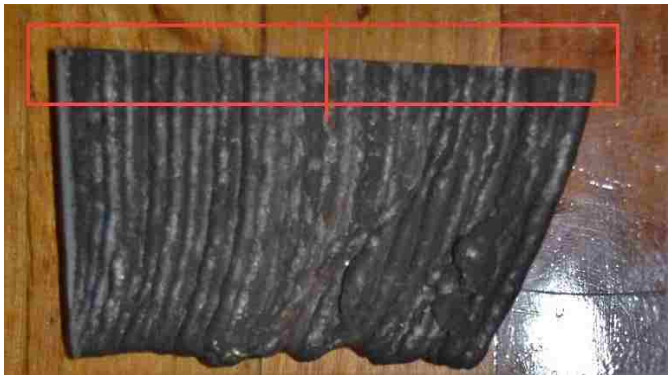

Figure 2.5 : Section of the intent cut for displaying the microstructure

Figure2.6 shows the cut piece after conducting the electric etching process, electric etching process demands to put the piece inside an acid and contact the ends of the piece by an electric circuit, and the original one, which is done for make the microstructure features clearer. The left side of Figure 2.6 shows the mounted pieces cut in half to fit into the mold.

Figure 2.6 : The cut pieces with the left original piece

Checking the dimensions again for the etched parts Figure 2.7.

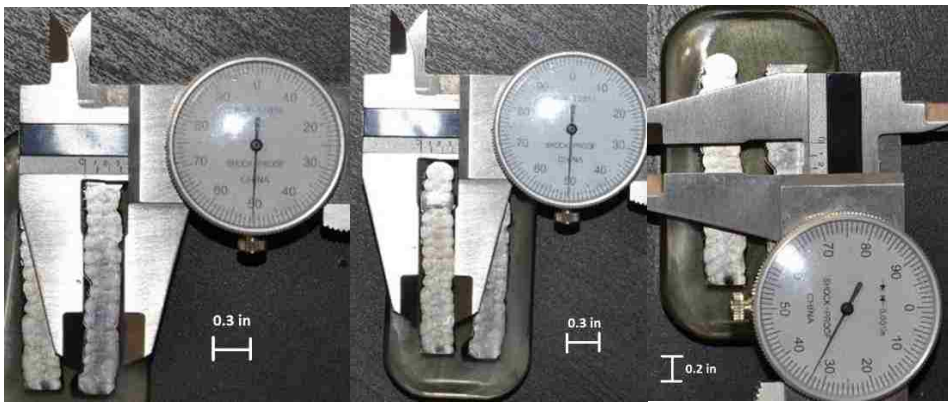

Figure 2.7 : Three pictures showing the dimensions of the printed layer.

Figure 2.8 shows the cut piece (cross section cut) under two different light degrees for showing some features for the layers. These pictures have been taken by using a canon camera 600d.

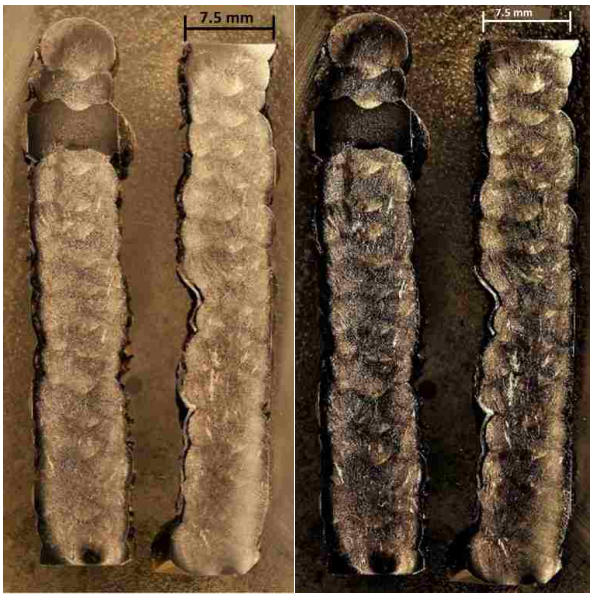

Figure 2.8 : Two different colored images for the microstructure printed part

Mathematical Molding

For heat input

$$Heat\ Input = \frac{V\ I}{S}\eta \qquad Watts * \frac{s}{mm} * Joule/s$$

$$V = Electric\ Voltage\ (Volt)$$

$$I = Electric\ Current\ \ (Amp)$$

$$S = Torch\ Velocity\ (mm/s)$$

$$\eta = efficiency$$

For this sample, the voltage used was 20V, and the current varied depending on the process of welding (average currents are around 77 Amp). The torch velocity was 2.54 mm/s. If we consider the efficiency of the welding heat input to be 0.8, the heat input required for the simulation processes was found to be around 480 Joule/s. By using Smart Weld, Smart Weld is a software was created based on a scientific data in order to help engineers to determine the welding parameters before starting the actual processes, we can get the shape and the dimension of the penetration area. Figure 2.9 shows the result for the given parameters (speed, depth and type of metal) then Smart Weld has been developed depending on experiment test. Smart Weld gives the input power as 1231 Watts (which is voltage multiplied by the current and efficiency of the processes). After dividing it by the speed, it gives 473 Joule/s, which is almost as the same as the calculated power.

Figure 2.9 : Smart Weld screenshot shows the parameters of the welding processes

Simulation

In order to know the mechanical properties for this sample or a portion of it, it is efficient to use some of the capable software: one of them is SYSWELD. In this case, the sample has been developed using approximate dimensions to make the processes easy. By using SYSWELD, the simulate design has been made According to the real design (as shown in Figure 2.10) and by using the following dimensions: length, width, and height. In Figure 2.10 the red rectangles represent rigid clamps, which prevent the sample from moving in the Z-axis direction.

X = 800 mm for substrate, 700 mm for the welding passes, and the longest distance is 800 mm

Y = 100 mm for substrate, 10 mm for the welding passes, and the longest distance is 100 mm

Z = 5 mm for substrate, 85 mm for the welding passes, and the longest distance is 90 mm

For a single bead, length is 700 mm, width is 10 mm, and height is 2mm

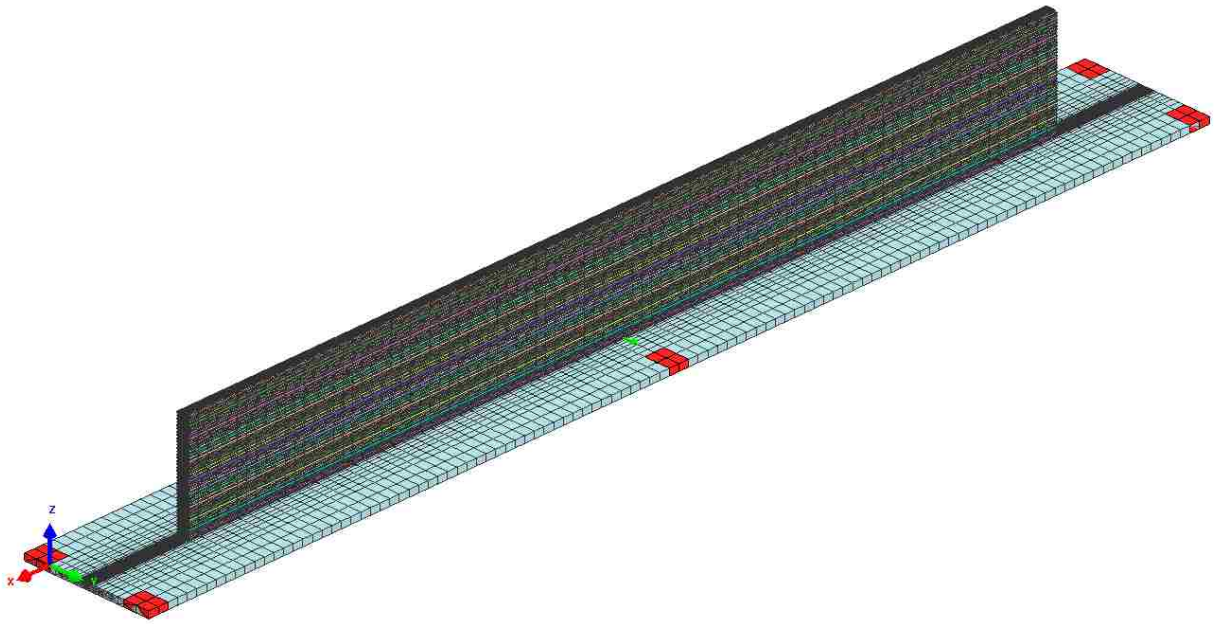

Figure 2.10 : The simulated sample constructed using SYSWELD

Figure 2.11 compares the actual measured cross-sectional area with the cross sectional area used in the finite element simulation.

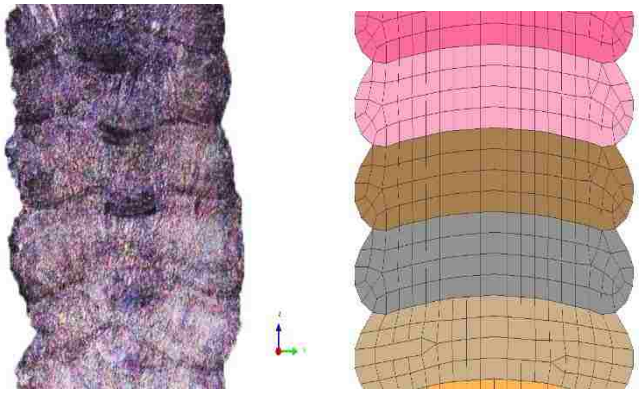

Figure 2.11 : Comparison between the shape of layers (real, left; simulated, right)

Before proceeding with the main model calculation, the simulation process needed some tests to validate the model setup – These tests are as follows: Heat test, Path test, Mesh test, Penetration test, and Clamping test – The purpose of the Heat test was to observe the behavior of temperature around the test model. As the full computational process took considerable time, it was effective to decrease the time by one half by taking advantage of symmetry. The heat behavior looked symmetric around the path of the power source. So, the test may have decreased the time to half of the original time. Furthermore, the Heat test could show the temperature behavior for each layer; so, nodes were chosen on top of layers for showing their behavior.. The Path test was used for showing the effect of the deposition direction during the process. The third test was the Mesh refinement test: the test displayed the effect of the number of elements (mesh) on the result. From the result, the number of elements were chosen in accordance with reasonable match on the result. The fourth test was the Penetration test: in this test, the melting pool dimensions were found to be different in three cases. This had been done because SYSWELD gives the choice to setup the dimensions of the penetration size; also, the arc

welding processes have different arc shapes depending on the welding parameters, which effected the melt pool size and shape. So, the purpose was to look at the heat effects of the different penetration dimensions on the layers. Ideally, the shape of the melted layers had to be as close as possible to the final layer shapes observed in the actual welding process – as shown in Figure 2.11. The real sample had the fluid effect on the melting part. So, the purpose of the penetration test was to look at the shape of the melting pool during computational process and to try to simulate as same as possible of the actual shape. The Clamping test was the last test: this test was conducted to test the computational process on two models. One was half the other model, the half is on X-axis that makes positive Y-axis is symmetric of negative Y-axis. Since the mechanical properties were symmetric around the X-axis and Y-axis, they may be used in saving time to compute the half model instead of the whole model. So, several conditions were established to get the matched results between the two models. In summary, integrating these tests allowed the main model to give the most accurate results possible for the existing conditions.

Heat test

Before the simulated real sample was processed, simulation processes needed to be tested for validating its reality. In addition, for that, it was great to have a coherent picture about the running processes of SYSWELD. The first test was the heat distribution test between two samples (seen in Figure 2.13) that were made from the main sample on Figure 2.12. So, the test was conducted using a base metal with 3 layers in the middle. The first run was made for the whole sample and the second run was made by a half of the complete sample was created by a symmetric plane of the sample into the middle of Y-axis, which left one part of the positive Y-axis and decreased the power into half as shown on Figure 2.12.

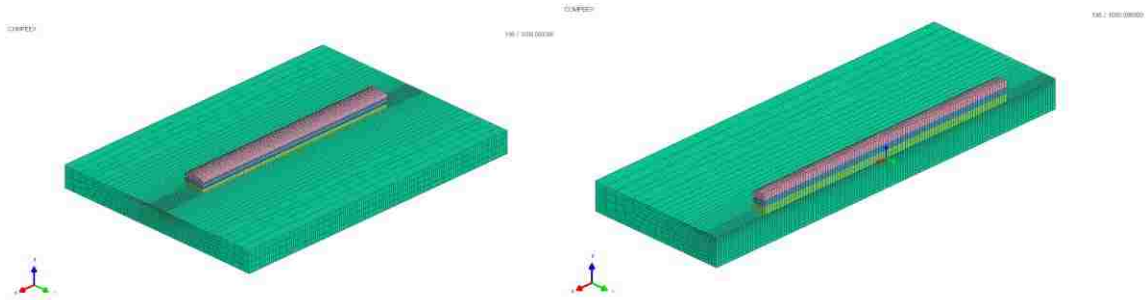

Figure 2.12 : The main (complete) sample on left, and the half sample on right

After running the two tests, cross section was made into the middle of X-axis to show the temperature distribution.

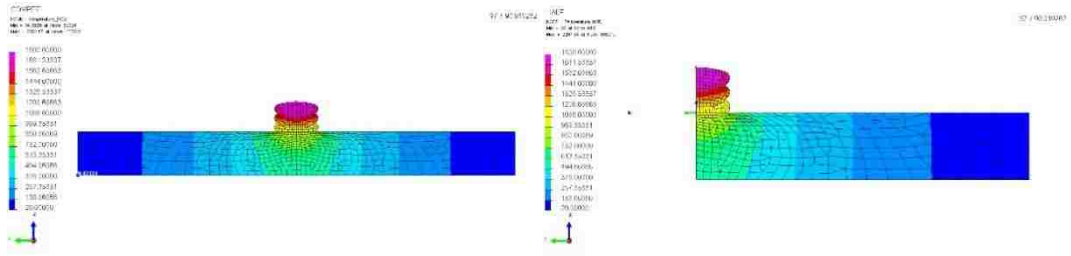

Figure 2.13 : Test result for the complete sample on the left and the half sample on the right

So, the main point was that heat was equally distributed and symmetric around the weld line, as shown in Figure 2.13 and Figure 2.14, and showed the cross-section on Y-axis for the whole sample and the half-running sample. It was clear from these two figures that the heat distributed was similar between the running tests, which gave the opportunity to run the samples faster because of the smaller sample size; besides, the result was found to be the same in both cases.

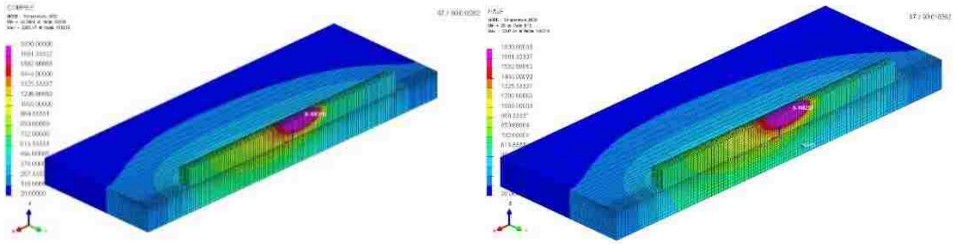

Figure 2.14 : Temperature distribution contours for two samples (complete, left; half, right)

The second Heat test was on the seven layers for half sample since the result was concluded and reasonable for the half sample. The sample geometry is shown on Figure 2.15; the cross section of the right side of the sample was insulated for the heat transfer in such a way that the boundaries looked like a complete sample.

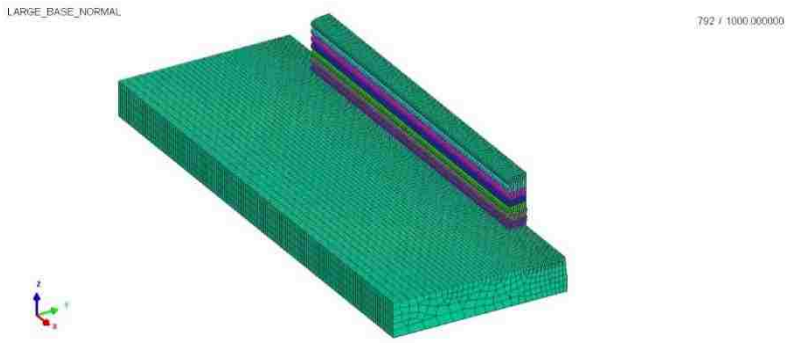

Figure 2.15 : The used half sample in the next tests

For understanding the temperature behavior, seven nodes were selected in the beginning – for each pass (layer) –on the meeting point between the heat source and melting metal. In the first attempt, the heat was found to be constant for each layer, which meant that it remained 240 Joules/s; the original power was found to be 480 Watts after the efficiency was calculated, and 240 Watts after it decreased to half, since the used geometry is half of the main geometry (with 480 Watts). Figure 2.16 shows temperature profiles for the seven passes. It is clear here that the peak temperature increased as the next layer started to build. The difference between the highest and the lowest temperature was around 600° Celsius, which was huge for a metal with a melting point of 1400 ° Celsius: This made the previous layer melt completely.

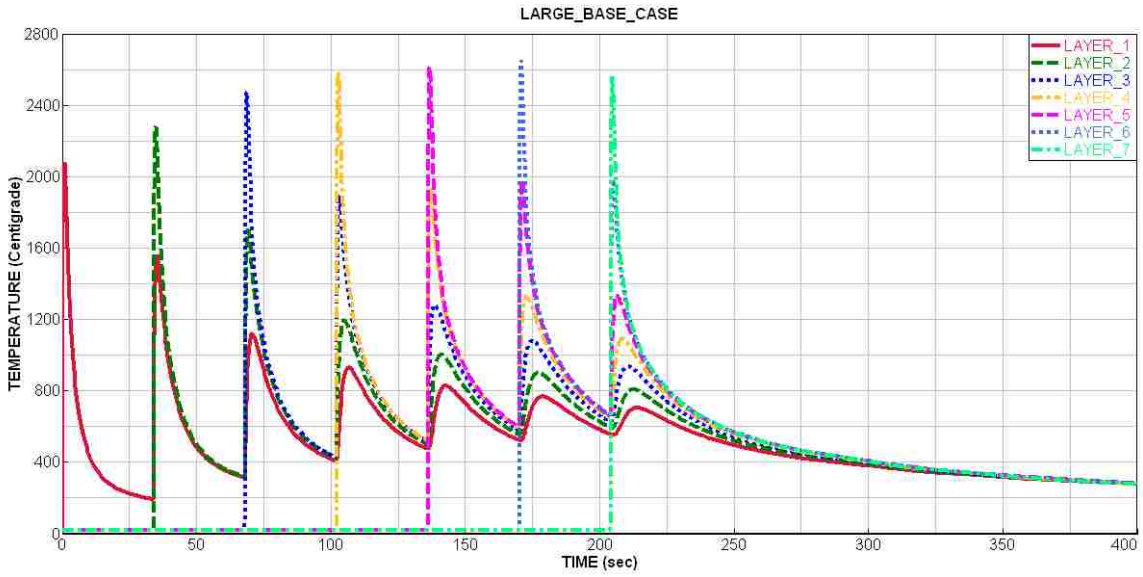

Figure 2.16 : Temperature profiles for heat constant and series deposition timing

So, in order to decrease that big difference, two different techniques had been used. The first trick was to cool down the sample with time gaps between the deposition of the layers, and the second one was decreasing the power for some simple relation rule. Figure 2.17 shows the temperature profiles for the time gaps case. From the curves, the difference between the highest

and the lowest peak temperature was found to be around 200 ° Celsius. This was a great technique to reduce the peak temperature, but it needed long time to build the whole sample.

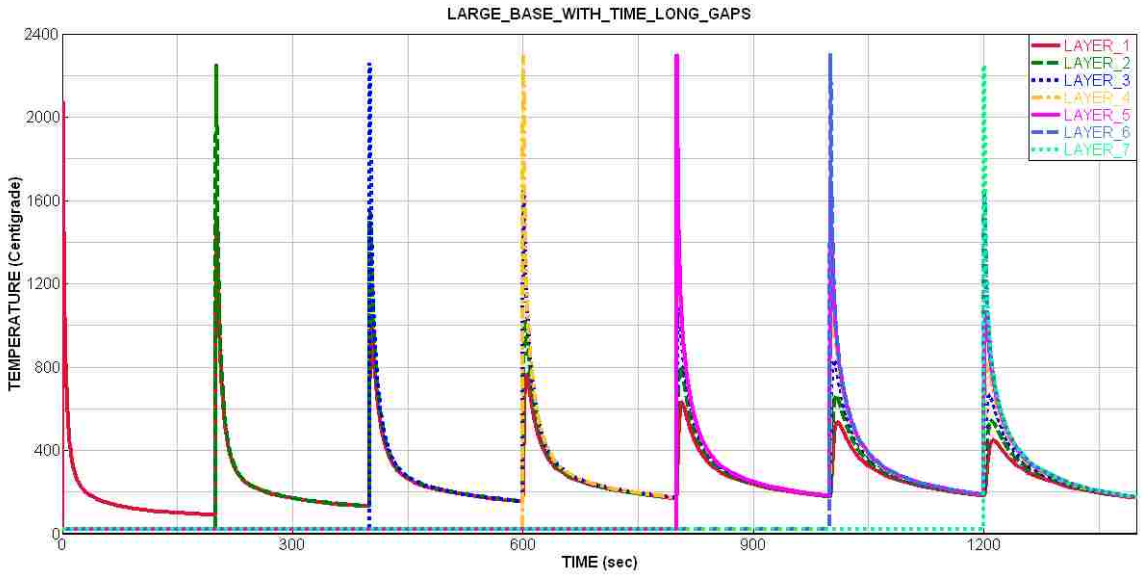

Figure 2.17 : Temperature behavior for the seven layers with time gaps between them

The second technique was to use the law

$$NP\ \ layer_{n+1} \approx OP\ layer_n \frac{OT\ \ layer_n}{OT\ \ layer_{n+1}}$$

$$NP = new\ power\ rate\ for\ the\ desired\ layer\ (n+1)$$

$$OP = old\ power\ of\ the\ last\ layer(n) before\ the\ deisred\ one(n+1)$$

$$OT = old\ peak\ Temp.\ for\ layer\ (n)\ or\ the\ melting\ temp.\ for\ the\ metal$$

By using this approximated relation, the new power rate was found as: 333, 304, 279, 268, 268, 263, 274 Joule/s, with η=0.8, from layers 1 to 7 respectively. So, the result was as expected (shown in Figure 2.18). The difference between the highest and the lowest peak temperatures had decreased, and the peak temperature also decreased for each pass after another, which made this way appropriate for saving time with suitable heat input.

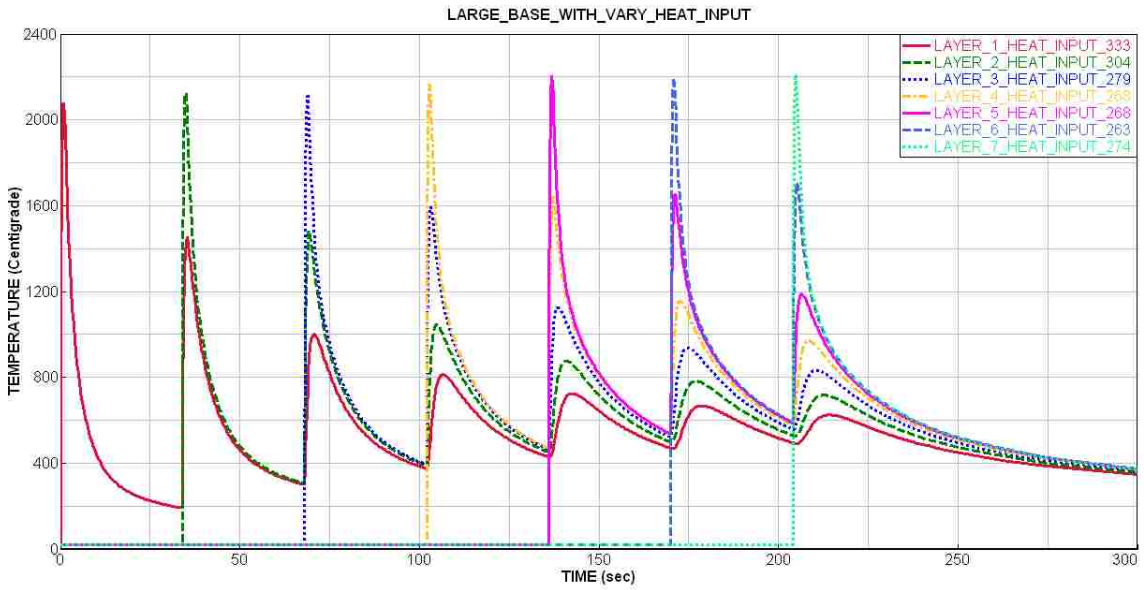

Figure 2.18 : Temperature behaviors for the seven layers with new proposed heat input

Another way of controlling the peak temperature was by decreasing the heat sink or the big consumption, which in our case was the substrate. So, the base metal had been designed to fit the width of layers and the longer length as shown in Figure 2.19. Temperature profiles (shown in Figure 2.20) showed quite a change in the difference between the highest and the lowest temperatures as 650 ^{o} Celsius, but it was not that efficient for heat transfer.

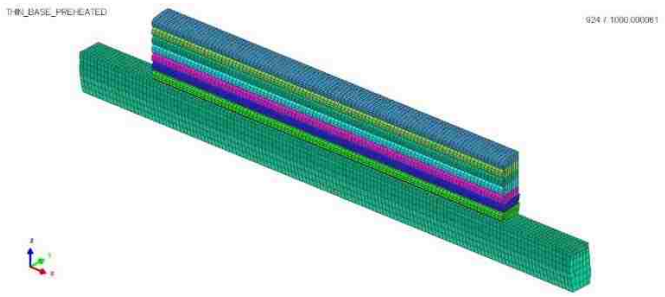

Figure 2.19 : The used half sample in the next test with a small base

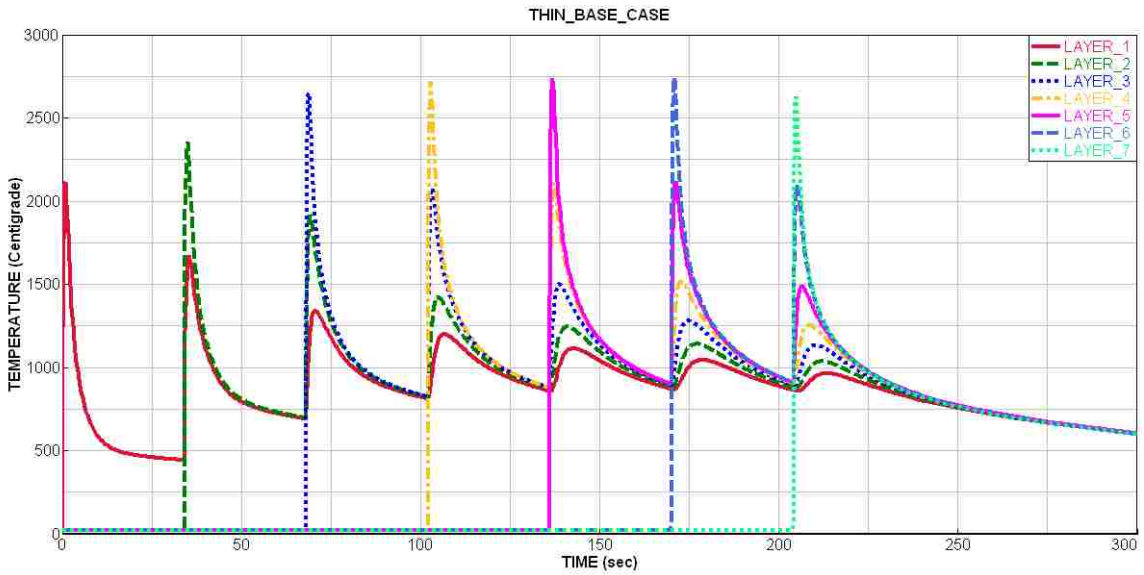

Figure 2.20 : Temperature behaviors for the seven layers with small bases

Another trick was preheating the substrate for a certain temperature to equalize the temperature between the base and the layers. It showed a lower difference than the last trick, but it had a disadvantage: it needed to modify the power to lower rates, since the base was already heated up. The result is shown in Figure 2.21

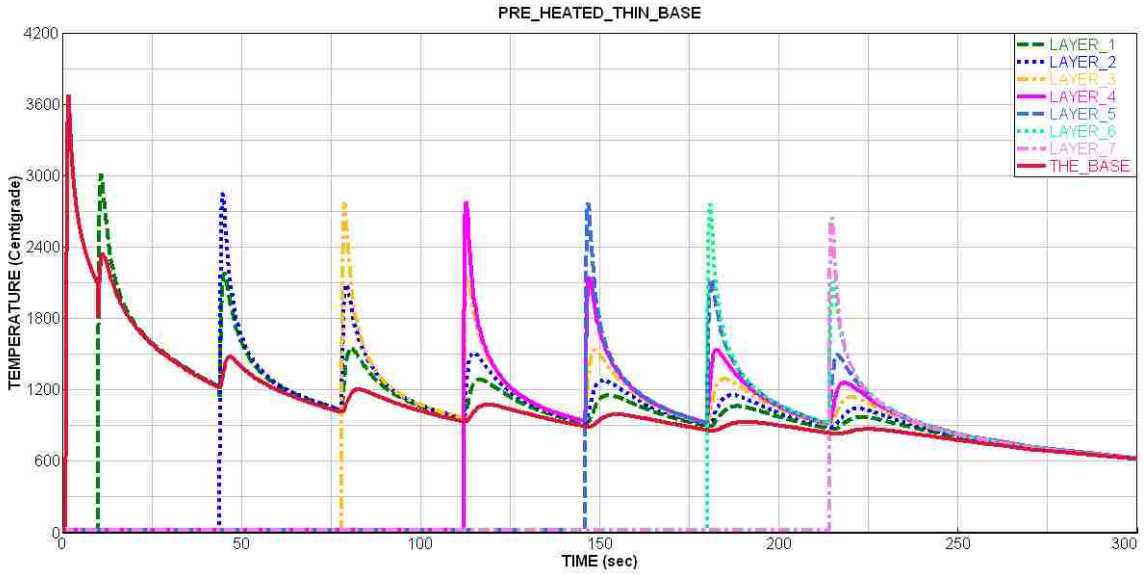

Figure 2.21 : Temperature behaviors for the seven layers after the base was heated up

Path test

One of the parameters for manufacturing by AM processes is the deposition path. As, common welding machines use a single torch, so for printing a plate requires two schemes paths. The first path was to start from one side and stop at the other, then return to the beginning to build the next layer. This is forward deposition. The second path was to start at the beginning and not stop at the second side; instead, continue to build the second layer from the other side, to the end, and back forward, as shown in the figure below Figure 2.22.

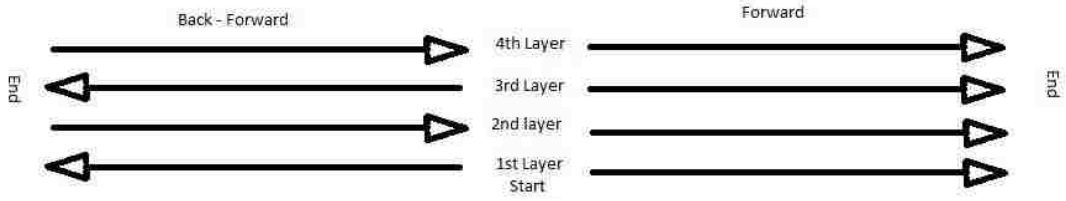

Figure 2.22 : The schemes description for forward path and back forward

So, for this case, the samples had five layers each and they underwent thermal and mechanical tests. For the heat distribution overall, both the ways had diffused the same amount of heat on the samples; cross section in the middle of the samples shows the identical temperature contours, as seen in Figure 2.23.

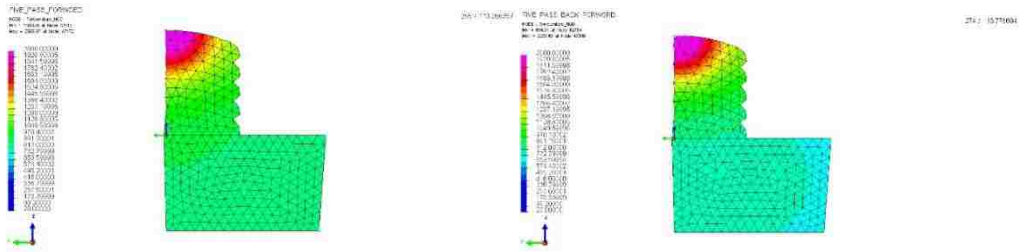

Figure 2.23 : Temperature contours for forward path (left) and back forward (right)

Also, the temperature profiles for certain nodes correlated to the heat input paths. These nodes have the same locations on both samples, the nodes located on the top of each start for each layer on forward path; so, they have the same Y and X coordinates, but changing Z coordinates. For the forward path, the result was same as that observed in the Heat test (see Figure 2.24). But, the more interesting is the back forward path, as seen in Figure 2.25 the layers had higher temperature than that's in the forward path. In both paths, the peak temperature was found to be around 2500 ° Celsius; but, forward path took five layers to reach it, while back forward path took two layers. So, that gave an idea about the heat around the ends, which was hotter on the end for forward and have the same for the both ends in back forward. For the timing condition, the deposition did not stop at any point between the start and end, which meant there was no time for cooling down the whole sample. The figure below for forward deposition path shows how the peak temperature increased by 500 ° Celsius between the first and the last layer, and by almost +100 ° Celsius for each layer.

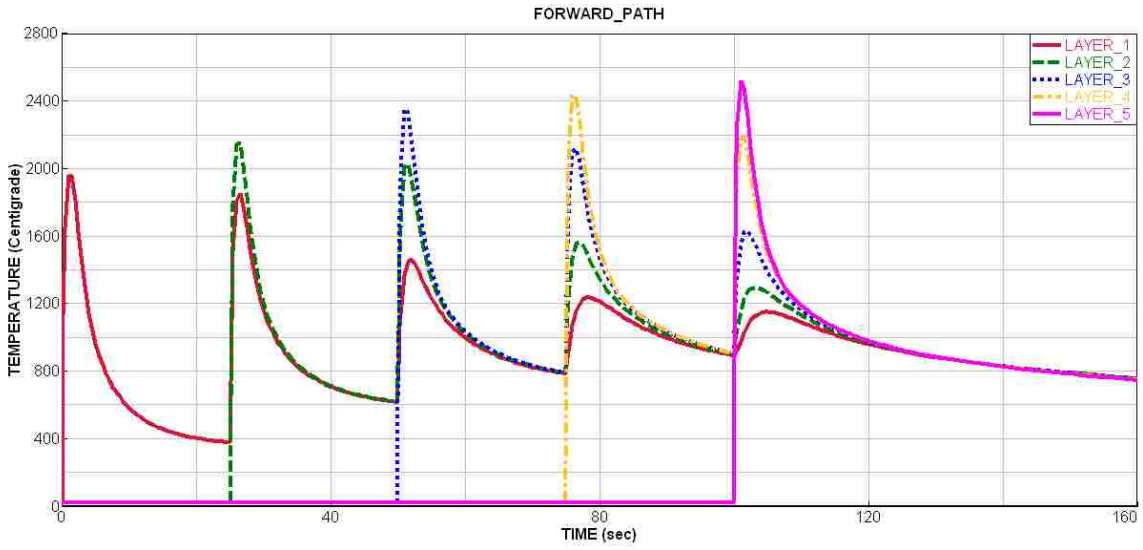

Figure 2.24 : Temperature profiles for forward path deposition

From the figure shown below the back forward deposition path – it was clear there was a high difference between the first node and the second. But, it also had a disadvantage: early deposition. SYSWELD needed to identify each filler material for each welded path. The filling materials were deposited part, not as continues deposition processes, and that can be observed by the temperature increase for the second node (second layer-green curve) at a time of 25 seconds. The node was deposited but not applied to the heat; instead, it was affected by the last layer temperature. So, it worked as a small heat sink for the previous layers. It could be considered as the preheat process, but the difference between preheating and this case was small in terms of the peak temperature, the region would melt, and the properties would be constructed again.

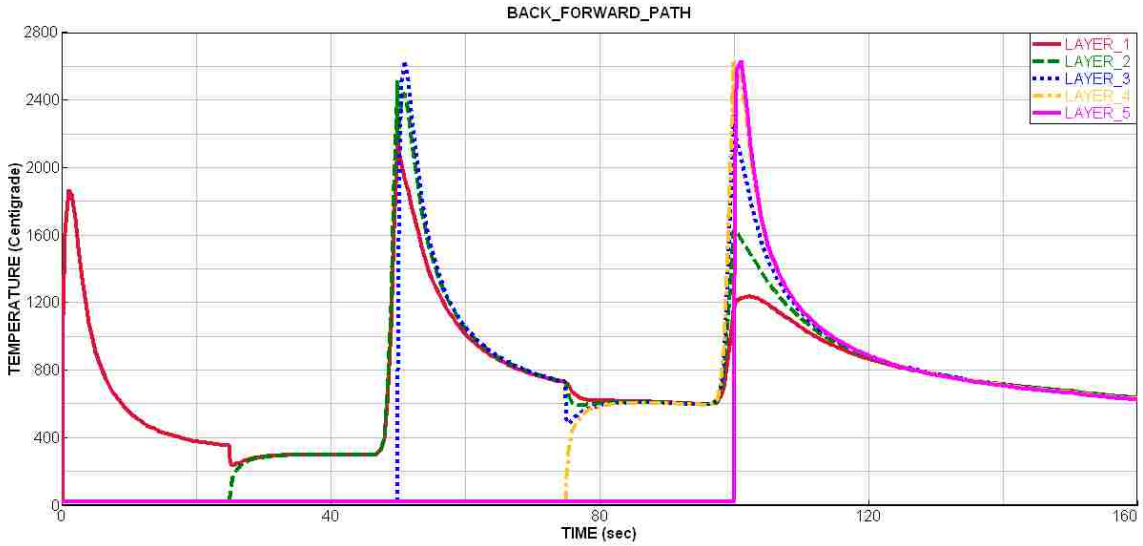

Figure 2.25 : Temperature profiles for back forward path deposition

Both paths have surface tension effects on the ends. Figure 2.26 shows the deformation caused by the heat on the end of forward path and the start has less deformation. The start also has lesser deformation than the middle. These were also comparisons made between the experiment of the actual sample and the simulated one.


[43]

Figure 2.26 : Distortion after printing (real, bottom; simulated, top) for forward path

Figure 2.27 shows the deformed ends for both back forward path and the actual sample. In contrast to the forward path, both endings have been deformed by the heat input, since the peak temperature occurred at the ends, as described on the temperature profiles in Figure 2.25


[43]

Figure 2.27 : Distortion after printing (real, bottom; simulate, top) for back forward path

These two techniques deform the ending in non-useful way, so it made the endings as non-active area. Figure 2.28 shows 3D contours for the σ_{XX} residual stress for the working pieces. Parts A and B show the outer part: they were almost equal in terms of stress. But, Parts C and D show the inside of the pieces, which were insulated thermally with some difference between these paths. The red region is tension (positive stress) and the blue region is compression (negative stress). Parts E and F show the clear difference between these paths by these cross-section contours. At the least, the similarity between them were the regions remaining in their position of comparison or tension but with difference in the values. In conclusion, these two paths had almost the same properties with trivial difference in the middle area, while the ends had the noticeable deformation difference.

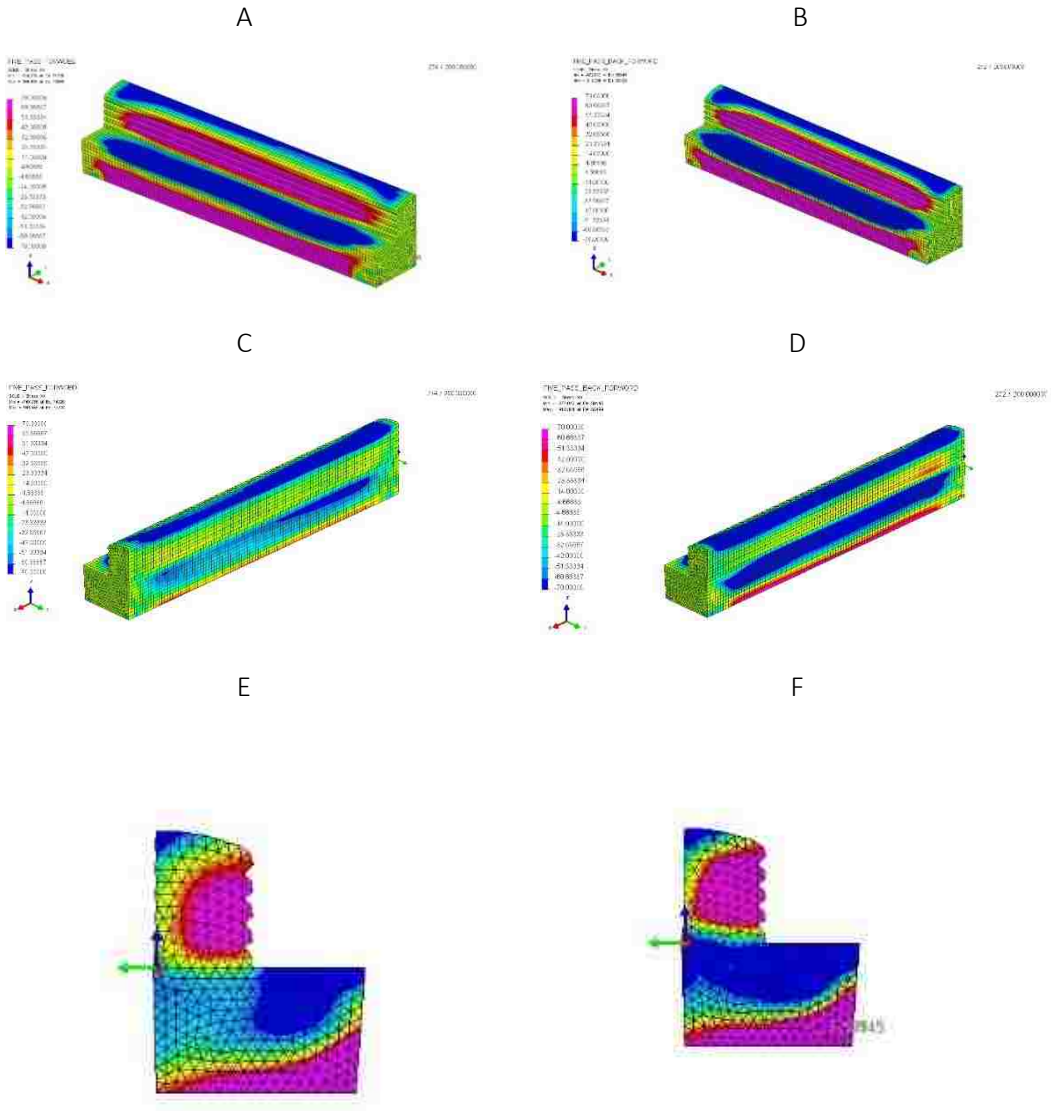

Figure 2.28 : Stress σ_{xx} contours for forward (left) and back forward (right)

Mesh test

Mesh test was important for result reliance; so, a single weld bead was tested thermally and mechanically. Also, the number of elements for the same sample was doubled: the less mesh sample had 7400 elements and the other sample had 14800 elements for the same dimensions. In Figure 2.29, the temperature disruptions were identical for both the samples at the same time (at 21 seconds). This made use of the less mesh sample more useful than the higher one in terms of thermal changes, because it needed lower time as well.

A B

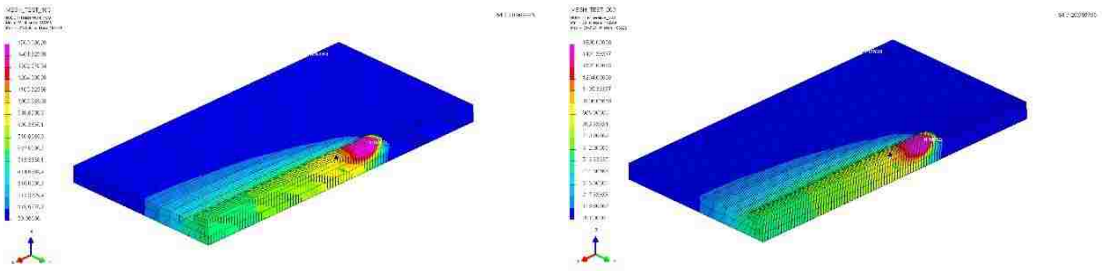

Figure 2.29 : Thermal contours for 7400 elements (left) and for 14800 elements (right)

The second aspect was the mechanical contours, as shown in Figure 2.30, for σ_{XX} residual stress. Similar to the thermal aspect, the contours looked identical in both mesh tests for 7400 and 14800 elements. So, that gave the less mesh elements the preference for time saving in the computational processes.

A B

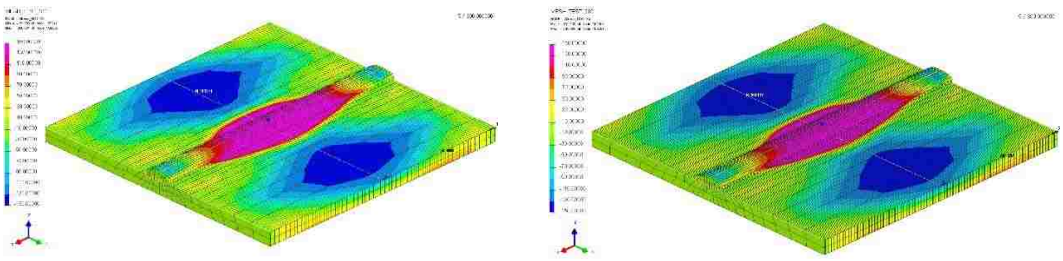

Figure 2.30 : σ_{XX} stress contours for 7400 elements (left) and for 14800 elements (right)

Moreover, for accuracy purposes, curves show a clearer picture of the relation between these two tests. Six node lines had been selected on the same position for both sample tests: three along X-axis (left, right, and wire) and three along Y-axis (front, rear, and middle), as seen in Figure 2.31.

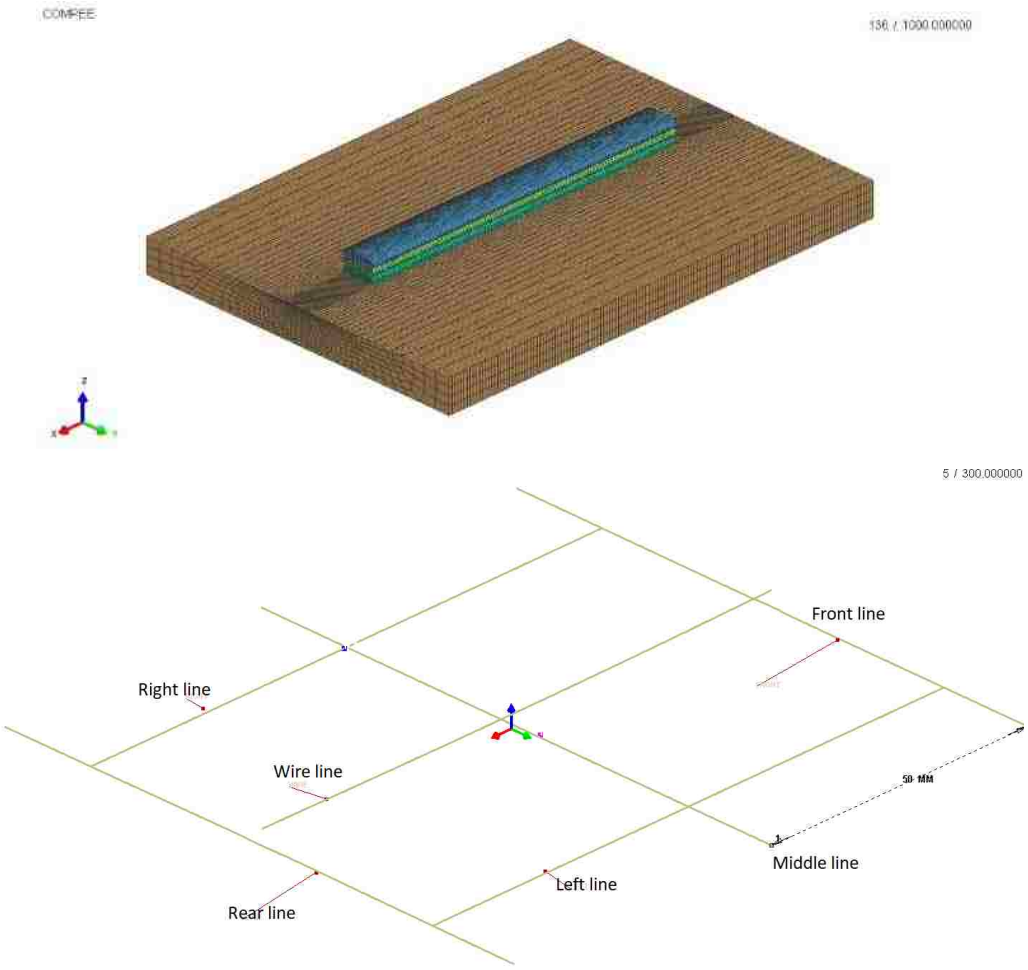

Figure 2.31 : Six lines on the work pieces for testing the mesh

Figure 2.32 shows σ_{XX} residual stress for the middle line. The profiles take the expected curves from welding process for single bead. At the center is the highest value, while it decreases from the center. The aim was to look at the similarity in the curves for 7400 and 14800 elements mesh tests. And, the highest difference between these two curves was found to be almost less than 0.01%, which made it easier to trust the less mesh sample for certain level of accuracy.

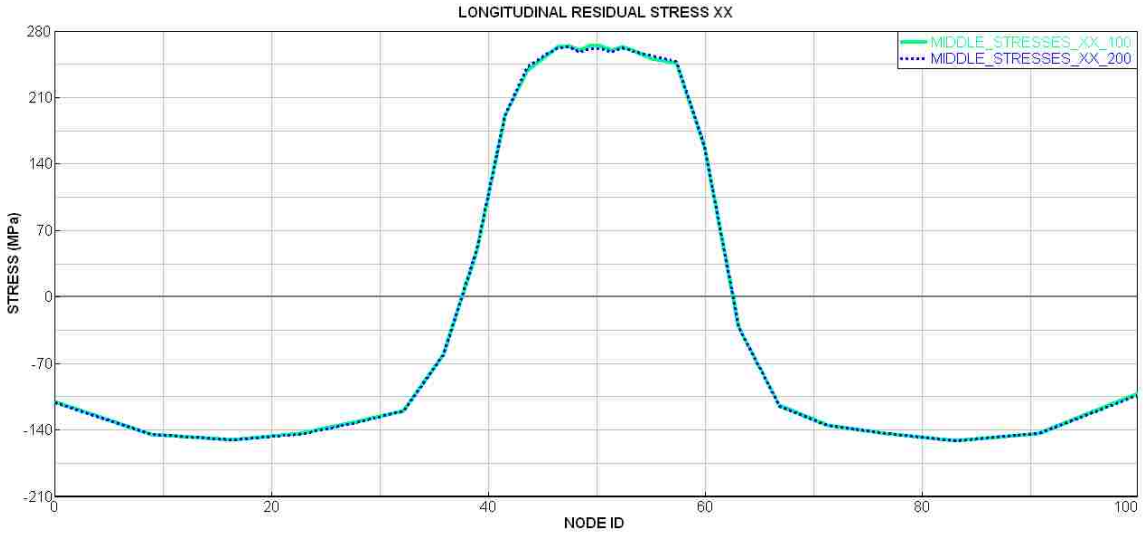

Figure 2.32 : σ_{XX} residual stress for the middle profiles in both the cases (7400 and 14800)

The second two test lines were placed on the wire for self-welding Figure 2.33. For the same curves, the σ_{YY} residual stress behavior was reasonable as the expected stress for welding single pass, and the same for both cases with the error less than 1% in certain areas.

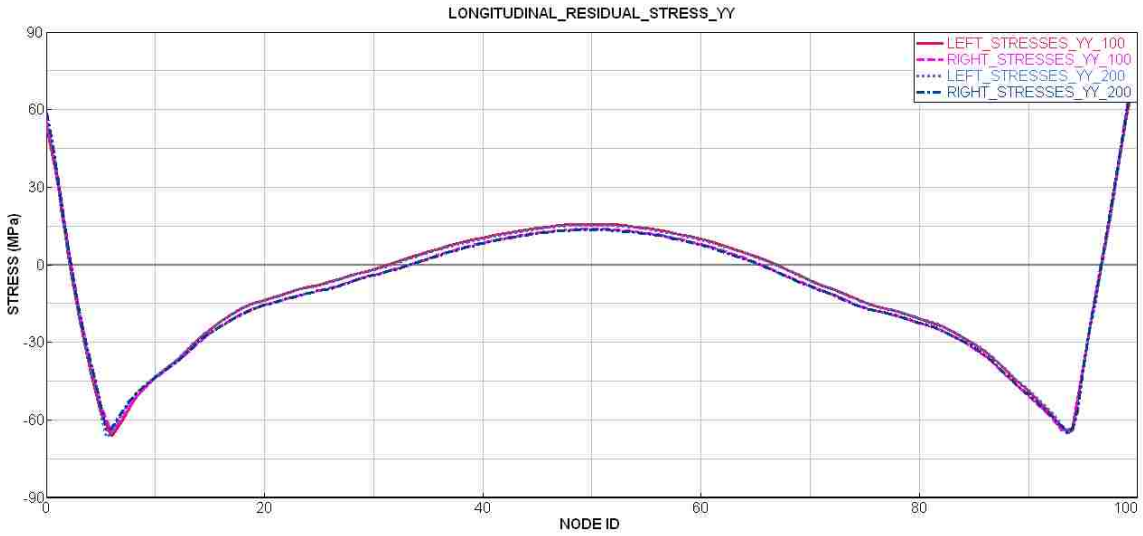

Figure 2.33 : σ_{YY} residual stress for the wire profiles in both the cases (7400 and 14800)

By looking at the σ_{XX} residual stress contours above in Figure2.30, both the left and right sides have the same behavior in terms of stress. Figure 2.34 shows the σ_{XX} residual stress for four lines,

taken from two positions of the two samples: left and right line for samples with 7400 elements and left and right line for samples with 14800 elements. Thus, the four lines have the same behavior.

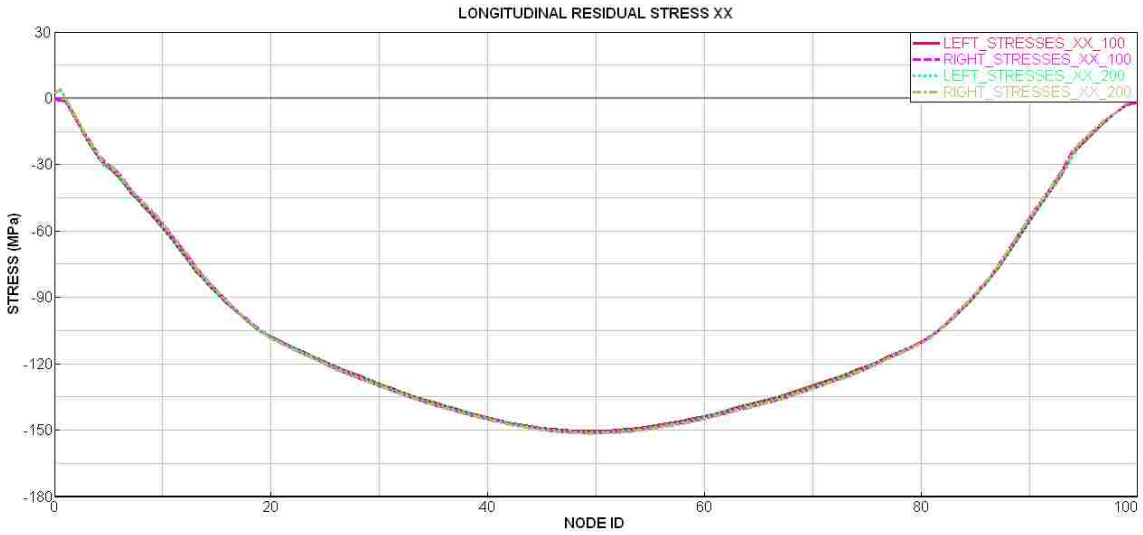

Figure 2.34 : σ_{XX} residual stress for the right and left profiles in both the cases (7400 and 14800)

In addition, these four lines, shown in Figure 2.31, were tests for σ_{XX} residual stress. To make sure even the other mechanical aspects had the same similarities, these four lines tested with σ_{XX} residual stress. For the same result Figure 2.35, the four lines had the same curvature for left and right lines in both the cases.

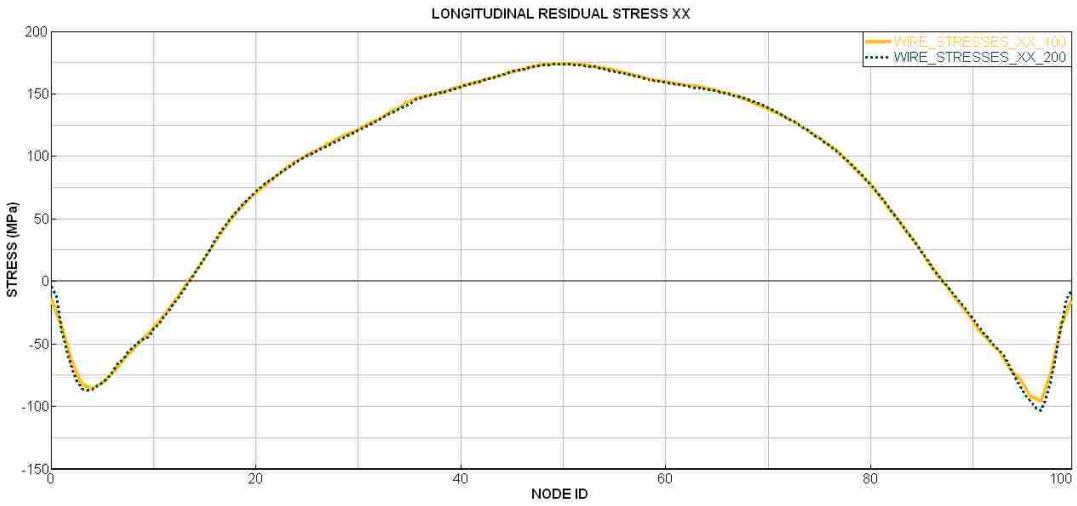

Figure 2.35 : σ_{XX} residual stress for the right and left profiles in both the cases (7400 and14800)

So, for all the previous lines the mesh size does not make difference to the importance of the mesh size; but, for front and rear lines from the samples they were found to be different. Figure 2.36 shows many unfitting areas for both cases: for the front lines, in the middle the behavior (sign) were the same. But, at the ends, the values did not follow at all.

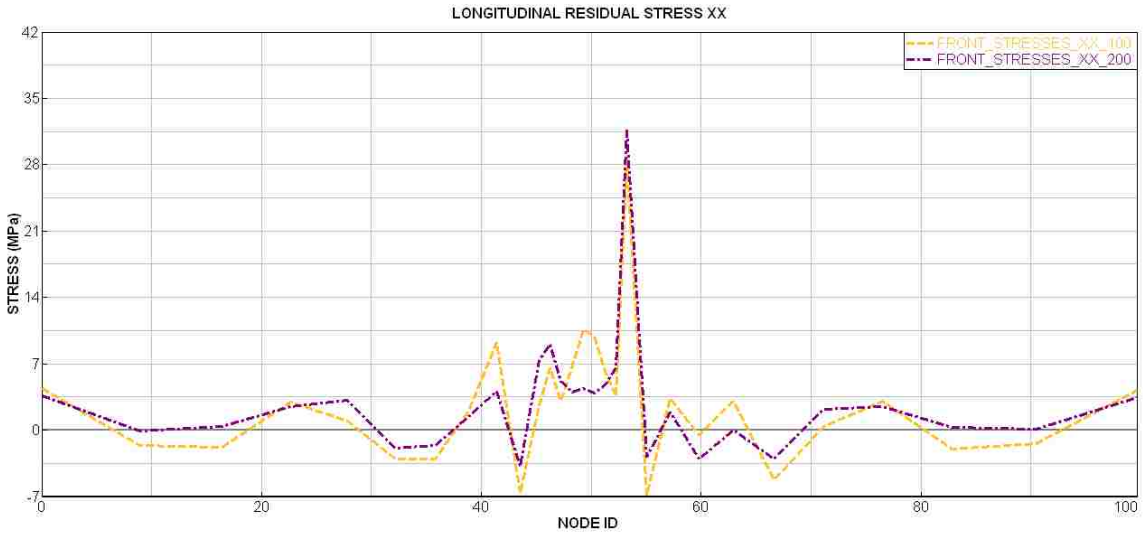

Figure 2.36 σ_{XX} residual stress for the front profiles in both cases (7400 and 14800)

Also Figure 2.37 shows rear lines σ_{XX} residual stress. These curves, as seen in B part of the figure, do not fit in most of the profiles, except in the middle, which is has the same sign, but different

values. And by looking to the original mesh in Figure 2.30, it was noticeable that the size of elements got bigger at the ends, unlikely to the middle. As a conclusion, the size of the elements was important to a certain level, and t no matter the size, the result would be identical. Also, for the least affected areas from the heat, the results were not accurate. For research purposes, AM simulation needed smaller mesh size on the active and interest area, at least a couple of millimeters for an edge.

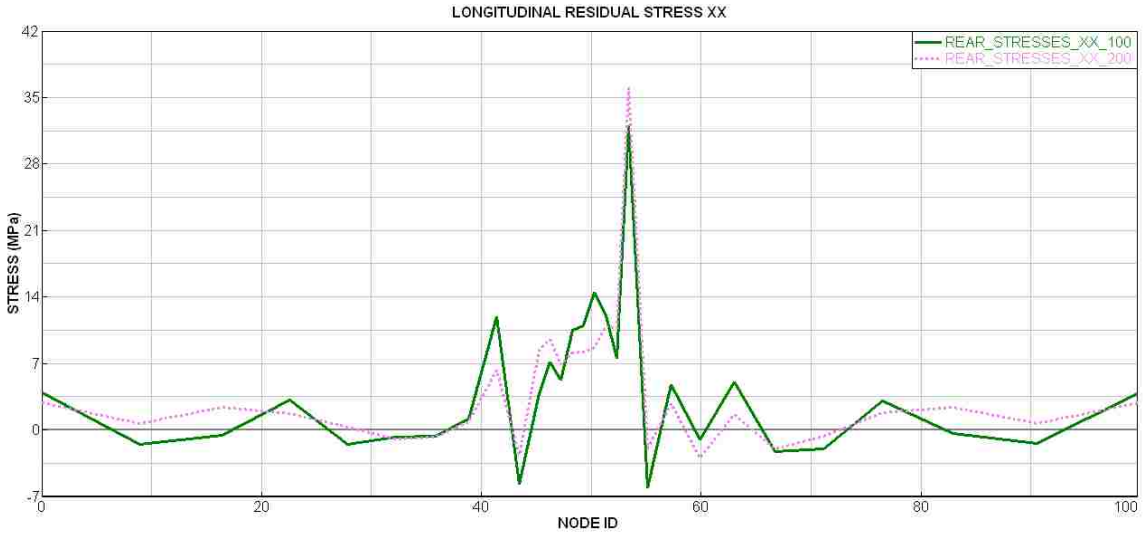

Figure 2.37 σ_{XX} *residual stress for the rear profiles in both the cases (7400 and 14800)*

Penetration test

For the simulation processes, the parameters of the melting pool and power parameters had been grabbed from Smart Weld. But, SYSWELD had the opportunity to fix the melting pool shape. AM needed that because the layer was not shaped as the regular melting pool in any welding processes. So, in order to look at the effects of these estimated dimensions for the melting pool on SYSWELD, three shapes were tested. The shape parameter is described in Figure 2.38 for the melting pool, and in Figure 2.39 A, the three-dimension parameters are shown as regular and large regular. The last shape was created to fit the layer (proposed) for all these shapes: the depth (penetration) was constant and the parameters were the width and the length. Figure 2.39 B, C, and D are the side views for the three shapes (back, left, and right).

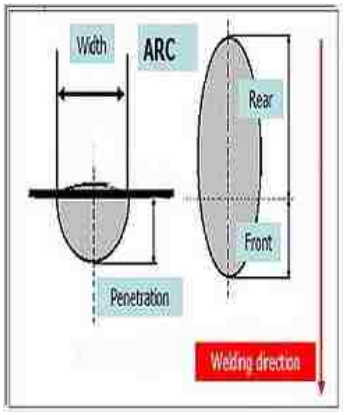

Figure 2.38 : The estimated dimension for the arc of welding from SYSWELD

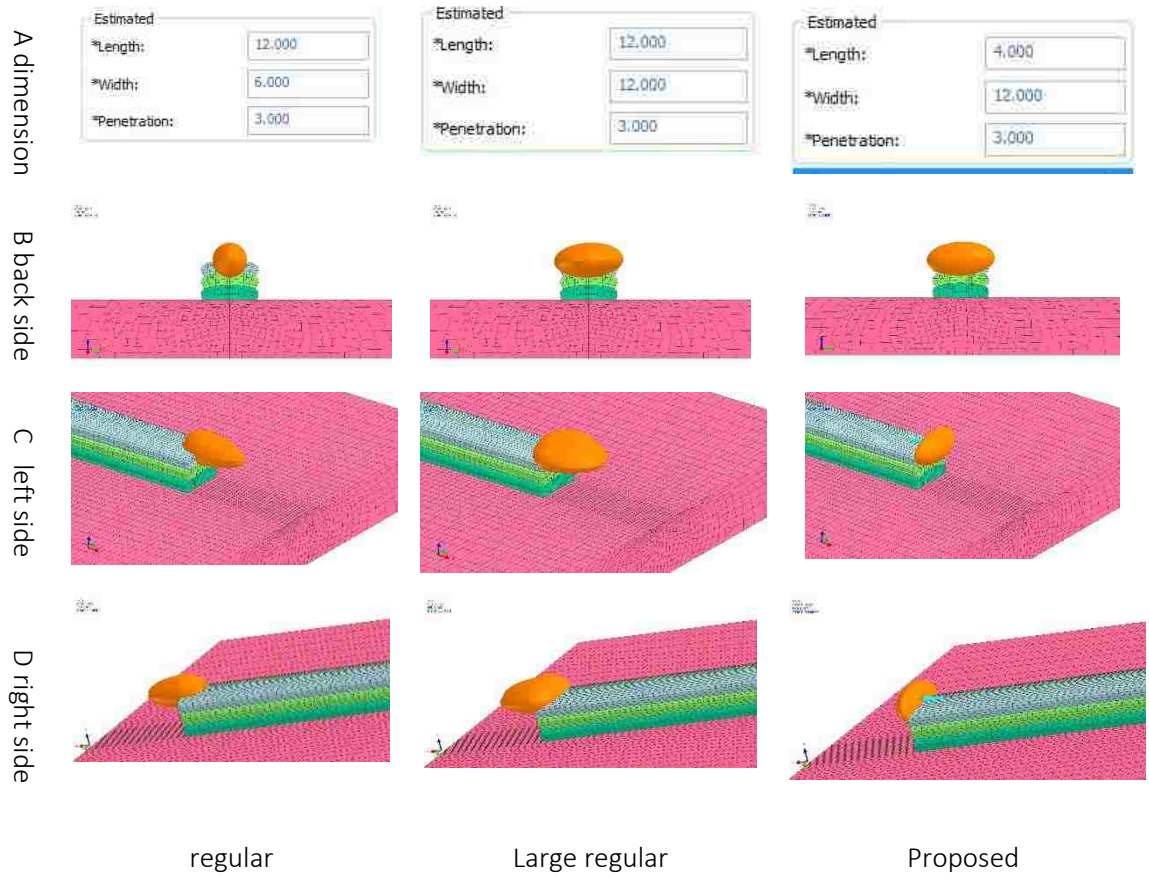

Figure 2.39 : The shape of the estimated arc of the welding

Therefore, the best way to judge was to draw the thermal contours at the 21st second. These images had been captured for the processes of the deposition of a third layer with different shapes for the estimated melting pool with same temperature color bar scale. Figure 2.40 A shows the right side for the melting pool, and it seemed the shapes were similar for the highest temperature and the heat regions. Figure 2.40 B shows slight difference on the front regions. The proposed shape received more sudden heat than other. Figure 2.40 C shows the cross section of the middle of the samples with the same estimated penetration depth. But, the simulated shapes were different among these three. On the large regular and the proposed shapes, the re-melting areas were bigger than the regular shape; besides that, all the top surfaces of the previous layer

were re-melting, which was not the case. Figure 2.11 shows that the re-melting area is in the middle of the previous layer surface, and Figure 2.40 C (regular) shows the simulated re-melting similar area to the actual one. As a conclusion, the more realistic melting pool for the simulated process was the regular even if the shape of the welding bead was different from the regular welding processes.

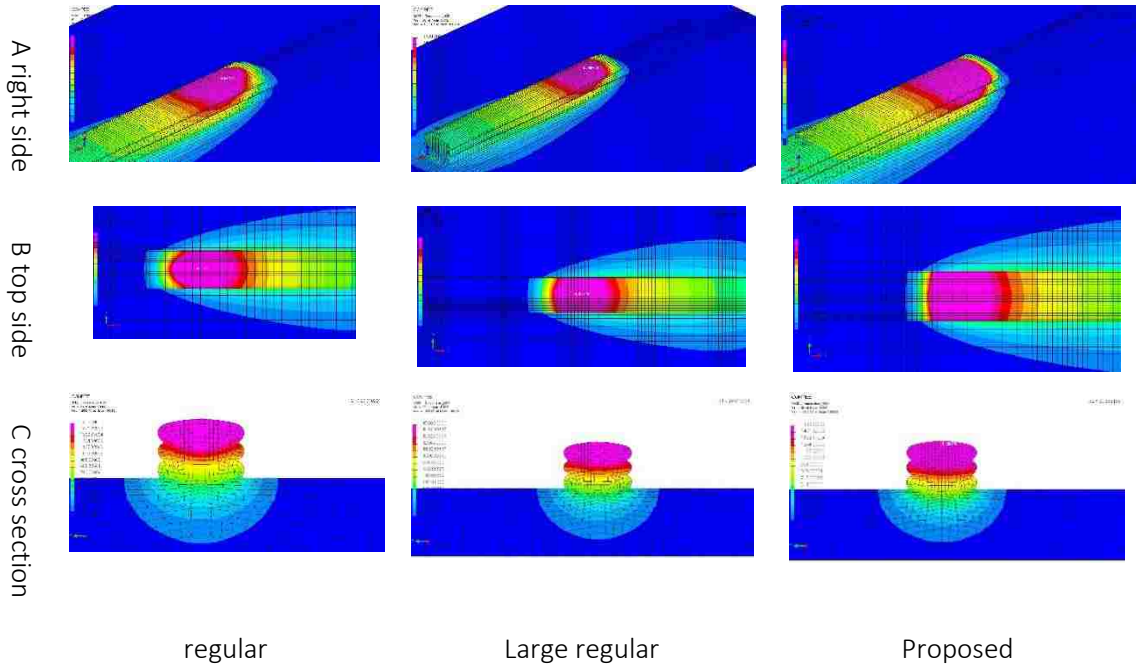

Figure 2.40 : Thermal contours from different sides for three estimated arc dimensions

Clamping test

As the previous Heat test proved that there was no difference if the sample was computed by the half or not, the temperature distribution around the sample was symmetric around the symmetric plane if the heat boundary conditions remained appropriate conditions. And, the purpose of that was to decrease the running time for computational processes. So, it was required to do the same for the residual stress, as they were interest areas for the research. This could be considered as the clamping effect or the clamping test for the AM for few layer depositions. The test had two samples: one was the complete sample and the second was half of it. The second sample was half of the complete one – at the middle of the large one – one of the tests was created from symmetric plane through the sample on the X axis; all the samples were tested for showing the σ_{XX} residual stress contours. Figure .2.41 A shows the symmetric plane of sample around X-axis and the complete one. Figure 2.41 B) shows the complete sample with three layers for decreasing the time of computation. Also Figure. 2.42 shows (in red) the clamping element for the first next tests.

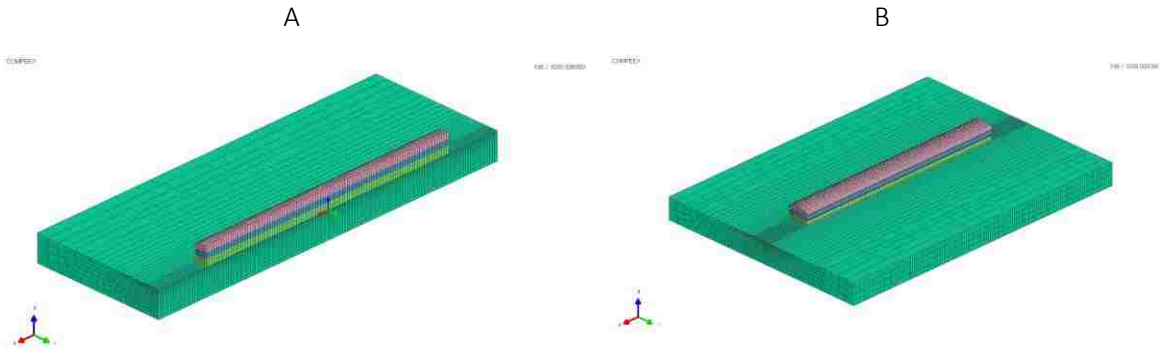

Figure 2.41: The complete sample(right) and the half sample (left)

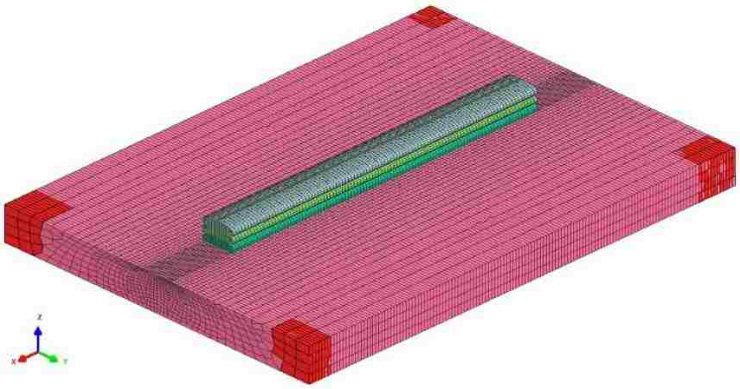

Figure 2.42 : The clamping condition for the whole sample.

The test was conducted when the clamping held the sample in one dimension (Z-axis): this axis was fixed. That meant the clamping elements were prevented from moving in this direction, which made them resistant to changes from neighboring elements. The half sample had another clamping condition: it was symmetrical assumption on the cross section cut. So, the cross section was fixed on moving Y axis

Figure. 2.43 shows the color scale for the residual stress, besides the used unit for the stresses on the test samples.

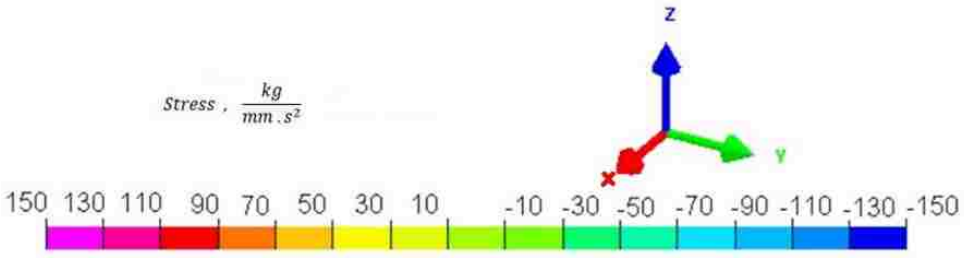

Figure 2.43 : Color scale for the stress

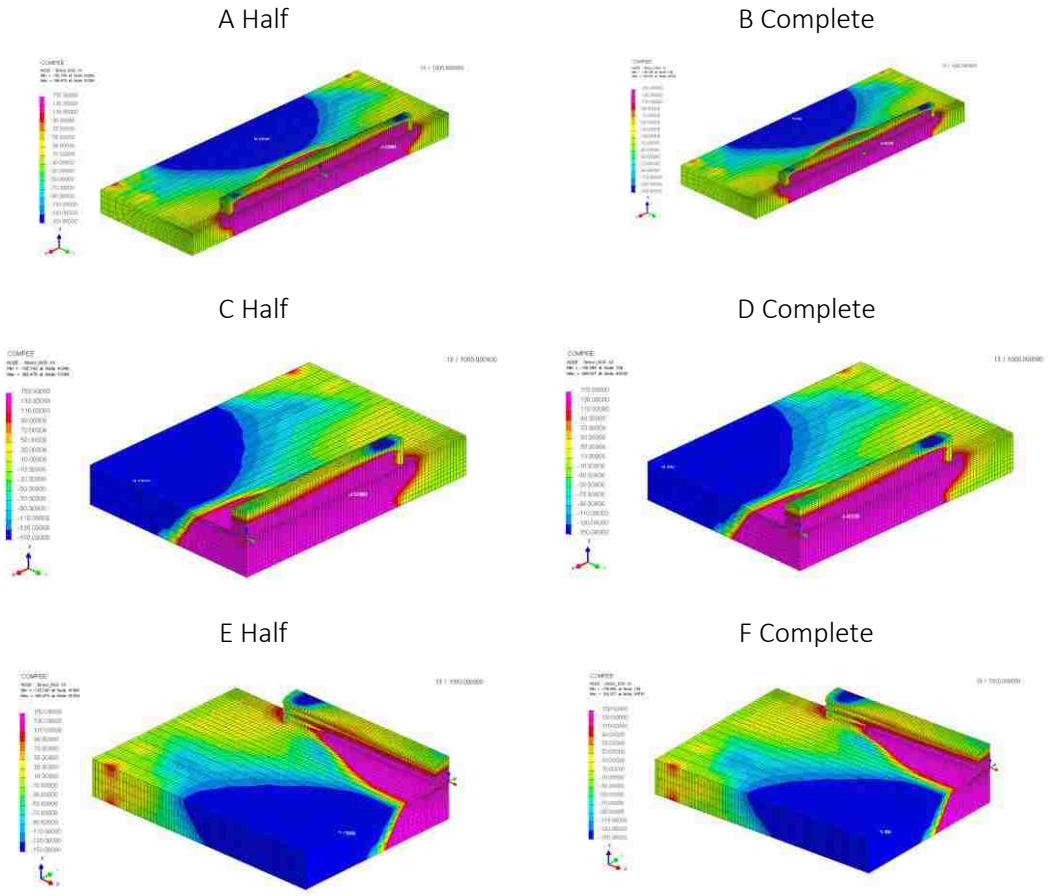

Figure 2.44 : Isometric σ_{XX} residual stress contours for regular clamping (fixed X, Y, and Z)

Figures 2.44 A, C, and E illustrate isometric contours for the σ_{XX} residual stress for the half sample and Figures 2.44 B, D, and F show the same result for the complete sample.

It is clear Figures 2.44 A, C, and E look like Figures 2.44 B, D, and F. Moreover, the complete sample was symmetric thermally and mechanically, as shown in the Mesh test (see Figures 2.29-36), also it was efficient to create a symmetric plane which divided the sample into two parts around the deposition direction to reduce the computation time because the number of elements was reduced to half. Furthermore, the affected factor, which was the welding heat, was on the center of the sample, and the heat contours were symmetric because there were other factors to change the distribution. The clamping effects were as much as the heat source effects

on the mechanical properties. So, knowing the right boundary condition and the state of the models before and after made it easy to create less computational processes: in this case, the boundary conditions were two main conditions thermal and mechanical conditions. For the thermal making, the cross-section symmetric plane was insulated, while for the mechanical, the cross section symmetric plane was fixed for the symmetric axis. Moreover, Figure 2.45 shows the result of this test for the displacement on Z-axis. In addition, Figure 2.45 A similar to Figure 2.45 B, they were the same and there was no difference between the complete and the half sample in terms of stress and displacement. For sure, there may have been a slight difference but, overall, it looked the same

A Half B Complete

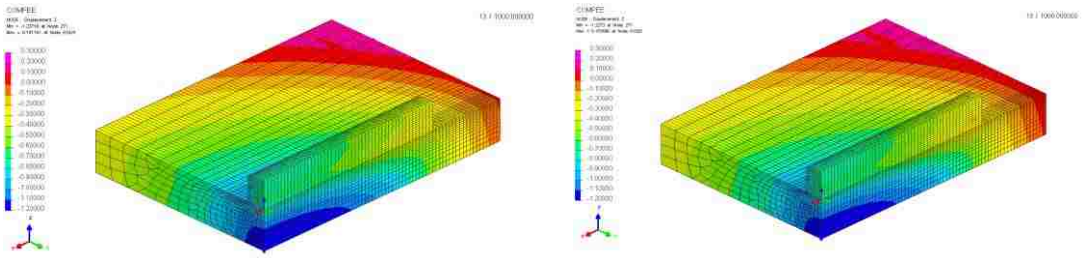

Figure 2.45 : Isometric σ_{XX} residual stress contours for fixed X-axis clamping condition

Chapter 3 Results

The models in Figure 2.1 and Figure 2.7 were formulated using two different materials with the welding parameters given in table 3.1. The purpose was to study the residual stress and distortion of this WAAM printed part as shown in Figure 2.1 using two different materials.

Table 3.1 WAAM simulation processes parameters in SYSWELD

Wire Type					welding speed	
austenitic stainless-steel grade 316L			Low carbon steel S355J2G3		2.5 mm/s	
Layers, Number	length	width	Thickness	Substrate Dimension	AMP	voltage
38 Layers	700 mm	8 mm	2.4 mm	5 X 100 X 800 mm	70	22V

Results for austenitic stainless-steel grade 316L at heat input 325 J/mm

The first simulation process was for austenitic stainless-steel grade 316L, which has specifications as below in Table 3.2 and mechanical properties as in Table 3.3.

Table 3.2 : *Chemical composition of austenitic stainless-steel grade 316L from "ESI Group" software database*

Element	C	Cr	Mn	Mo	Ni	P	S	Si
%	0.03	17	2	2.5	12	0.045	0.03	0.75

Table 3.3 : *ASTM Mechanical Properties of Austenitic stainless-steel grade 316L*

Element	Tensile strength (min)		Yield strength (min)		Hardness (max)	
316L	ksi	MPa	ksi	MPa	Brinell	Rockwell
	70	485	25	170	217	95

As the process was simulation welding, all the elements on the model would have to meet the melting temperature; in order to simulate the real processes as much as we can. For that, a set of nodes around a chosen layer have been selected Figure 3.1.

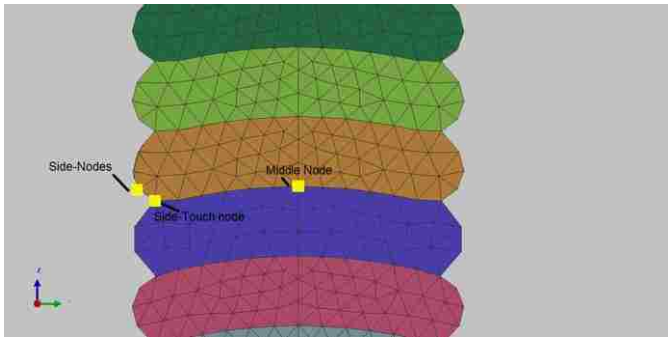

Figure 3.1 : Locations of interest nodes around a layer

Figure 3.2 shows the middle nodes temperature curves for layers 5,16,28, and 37. Knowing that the melting point is between 1371-1400°C, the middle node melts twice during the process; for example, the first melting time when the Layer_2 is formed and the second melting time when the layer_3 is deposited. Moreover, This case of melting the center of two layers describes what happens, as shown in Figure 2.11, when the real layer does not only have one, but two concave shapes.

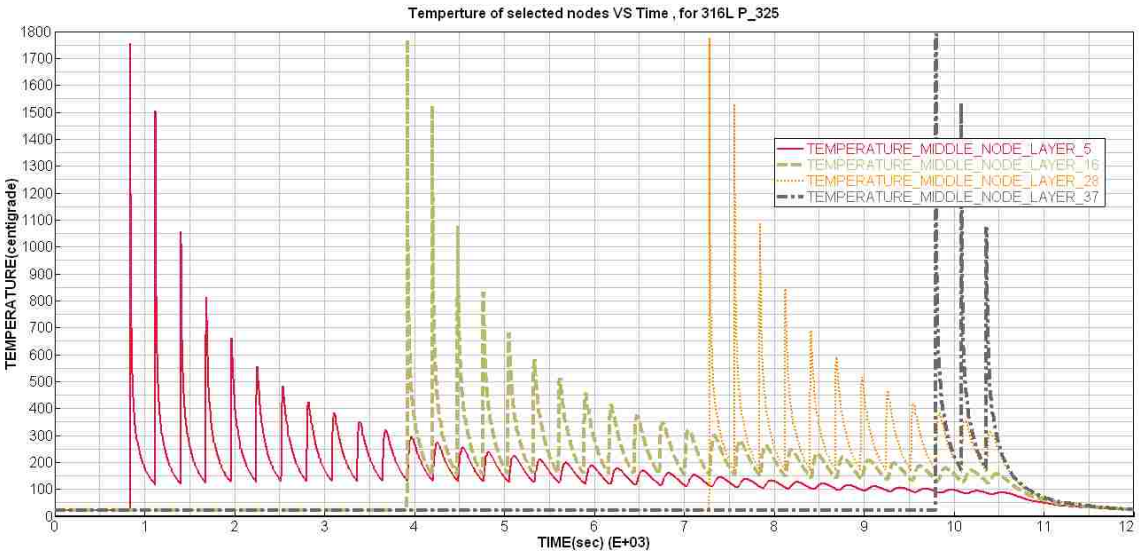

Figure 3.2 : Temperature behavior of Middle nodes for 316L, heat input 325 J/mm of Layers 5,16,28, and 37

For the middle nodes from figures 3.2, the peak temperature reaches 1700°C. This is because these nodes are under the heat source directly. Also, these nodes re-melt again with the next layer. The re-melting temperature reaches 1500°C, which is higher than the melting point. But for the third cycle the temperature reaches 1050°C for the center nodes, which is lower than the melting point by more than approximately 200°C.

Figure 3.3 shows the thermal curves pertaining to side-touch nodes for layers 5, 16, 28, and 37. For the side-touch node, which is the side-node farther from the middle node and has contact to the layers before and after it, this node melts twice, too. For e.g. one from layer 6 and the other from layer 7 deposits. But this particular node has a lower temperature from that of the middle nodes, since the middle nodes are closer to the heat source. In addition, these thermal cycles make the joining processes efficient on AM. But when the heat input is 325 J/mm, the simulation process indicates one full melting cycle. This means that this particular node at this power melted once at the first deposit. But when the latter layer deposited, it did not reach the melting-point temperature; which was approximately 1385°C.

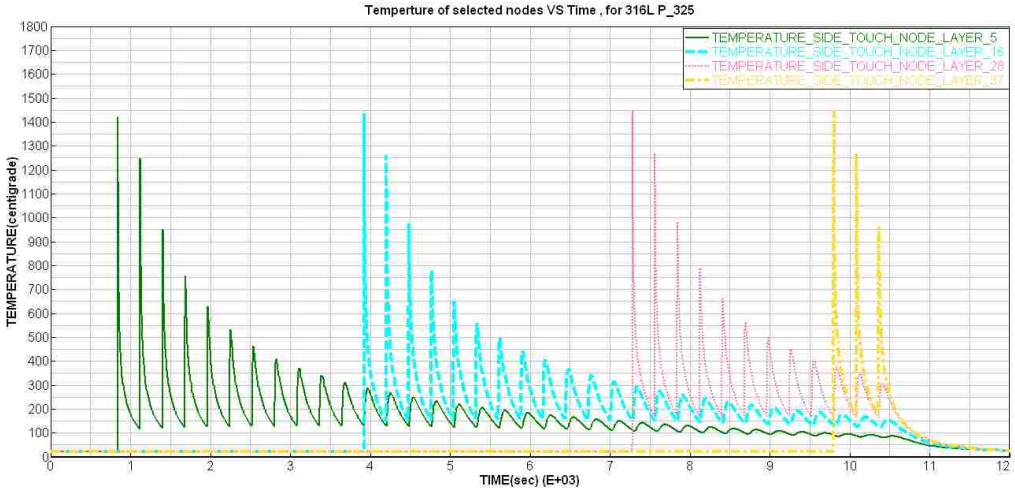

Figure 3.3 : Temperature behavior of side-touch nodes for 316L, heat input 325 J/mm of Layers 5,16,28, and 37

From figures 3.2 and 3.3, the thermal effect of the 25th layer or any layer beyond the first layer did not exceed 50°C. This meant that the WAAM processes are repeated after 25 layers This also meant that the layers repeat the same pattern of the first group of 25 layers. Also, the mechanical properties would not be affected by the heat directly but by the thermal and mechanical impact of the active layers.

The rest of the nodes, as shown in Figure 3.4, are those on the sides of layers 5, 16, 28 and 37. These have to be melted once for the same deposited layer. But, if they melt above the threshold, it will cause worse surface finishing. But, for these heat input parameters the peak of side nodes did not meet the melting temperatures, so it would cause un-melting nodes on the simulation, In the next section, a different heat input was simulated in order to see the effect of melting temperature for the nodes. From the previous figures 3.2 to 3.4, it seemed the peak temperature of a single layer decreased as an exponential function.

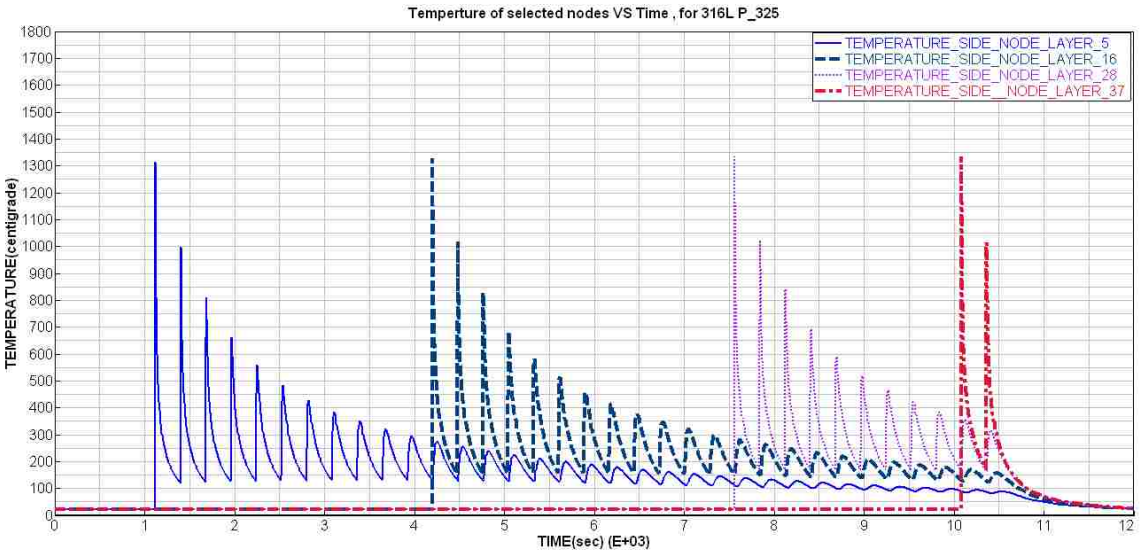

Figure 3.4 : Temperature behavior of side nodes for 316L, heat input 325 J/mm of layers 5,16,28, and 37

σ_{XX}- Residual Stress result of austenitic stainless-steel grade 316L at heat input 325 J/mm

Residual stress can change the shape of the part or its mechanical properties. For 3D printing WAAM, residual stresses are considered higher than that of other manufacturing processes. This was because of the effect of periodic welding heat on the part. This research focuses on two types of residual stresses - 1) Longitudinal and 2) Maximum principle stresses, the longitudinal stress is present to show the stress created in the same direction of the deposition processes, while the maximum is chosen in order to show the other types of stress effects in total. Also, all the results are taken after the sample cooled for 1500 seconds after completion of the welding, i.e., the sample cooled to room temperature.

Figure 3.5 shows σ_{XX}-Residual stresses (Longitudinal) for a cross section on the middle of the sample. The maximum σ_{XX}-residual stress is 361.26 MPa in tension and the minimum is -291.118 MPa in compression. The contour shows three main regions of residual stress. The first region is in the top region of the part, which is around the last 8 layers. The stress in this region is in a state of tension. The second region is between the 5^{th} Layer and the 30^{th} layer and is in compression. The third region comprises the layers around the base, which is in in tension. The right and left sides seem to have lower stresses compared with the regions in the middle. Also, it seems the clamping conditions made an alteration to the residual stresses because the values of the residual stresses in all the regions had a pattern that changes around the clamps either increase in the stress value or decrease .

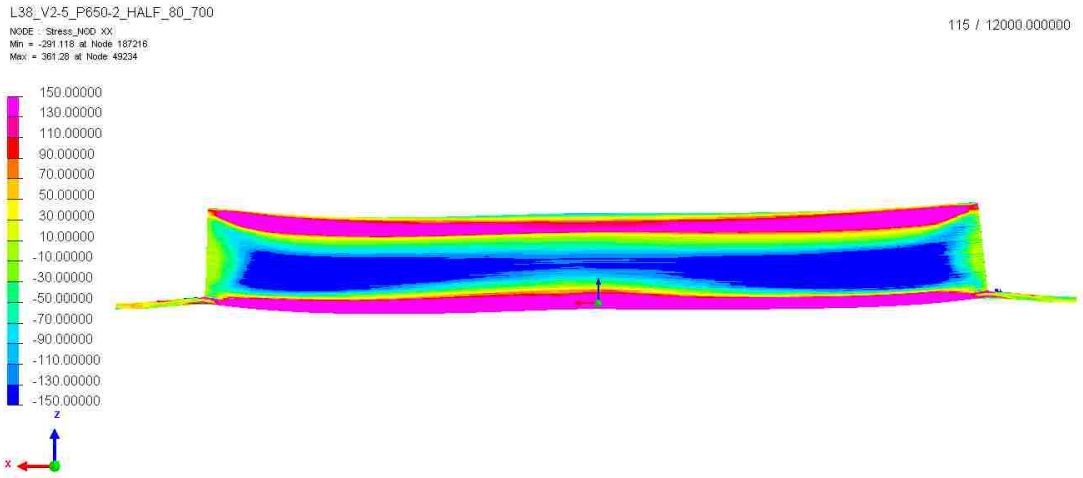

Figure 3.5 σ_{XX} - Longitudinal Residual stress of 3D printed 316L at heat input 325 J/mm X-Z plane -cross section view

Figure 3.6 shows the other side of figure 3.5. In this figure, the effects of clamp places are clearer than those in the last figure 3.5. Also, the regions are in the same state from the outside the pieces and the inside part of the symmetric plane. Furthermore, the base plate is in Compression. At the corners of the base, the stresses tend to be around a zero-stress situation since they are the farthest points from the direct heat effected region.

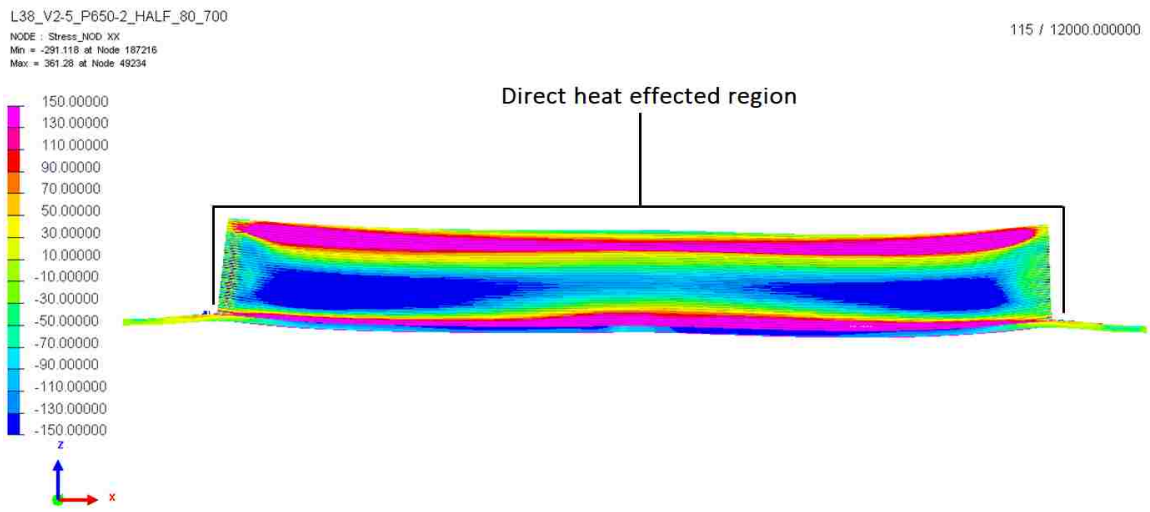

Figure 3.6 σ_{XX} - Longitudinal Residual stress of 3D printed 316L at heat input 325 J/mm X-Z plane view

Figures 3.7 and 3.8 show the same results as in figures 3.5 and 3.6, with an isometric view. These two figures show the effects of the clamps clearer than the last two figures 3.5 and 3.6, especially at the center of the base. Figure 3.8 shows the different regions of the stresses around the base. At the end and the start points of printing, the stress switches from compression to tension. The displacements of the z axis around the end and the start points are the highest among the base.

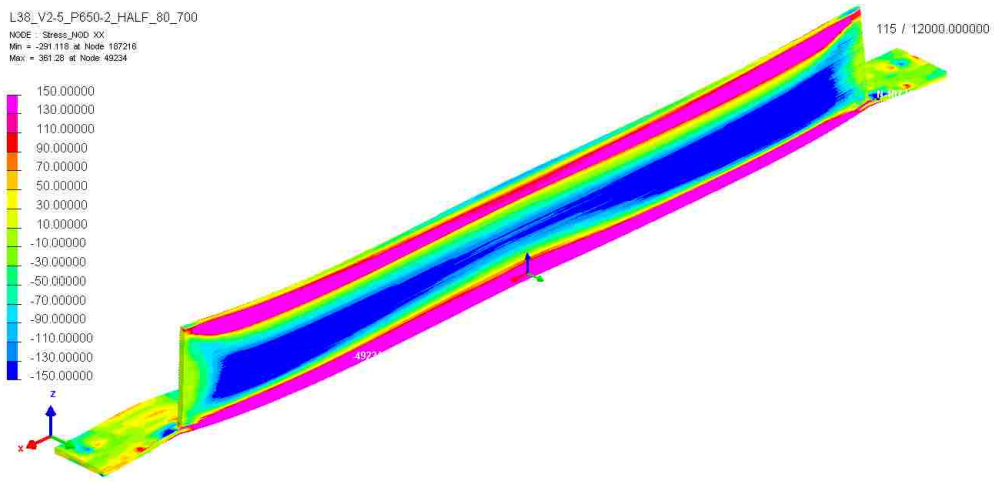

Figure 3.7 σ_{XX} - Longitudinal Residual stress of 3D printed 316L at heat input 325 J/mm Isometric-cross section view

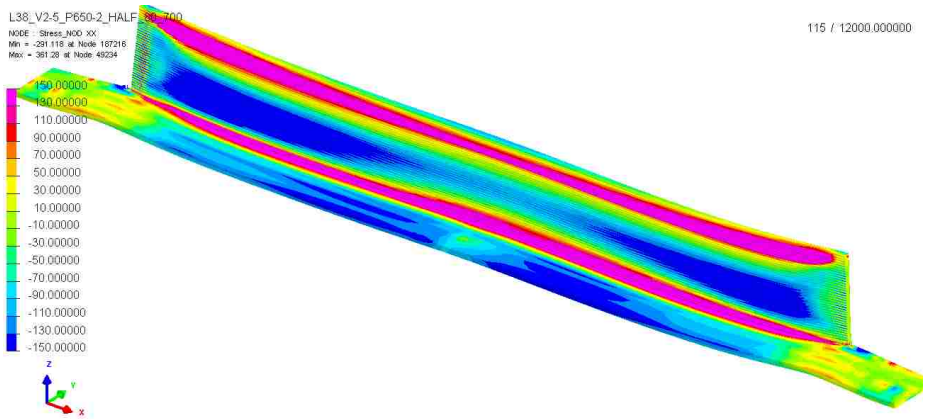

Figure 3.8 σ_{XX} - Longitudinal Residual stress of 3D printed 316L at heat input 325 J/mm Isometric view

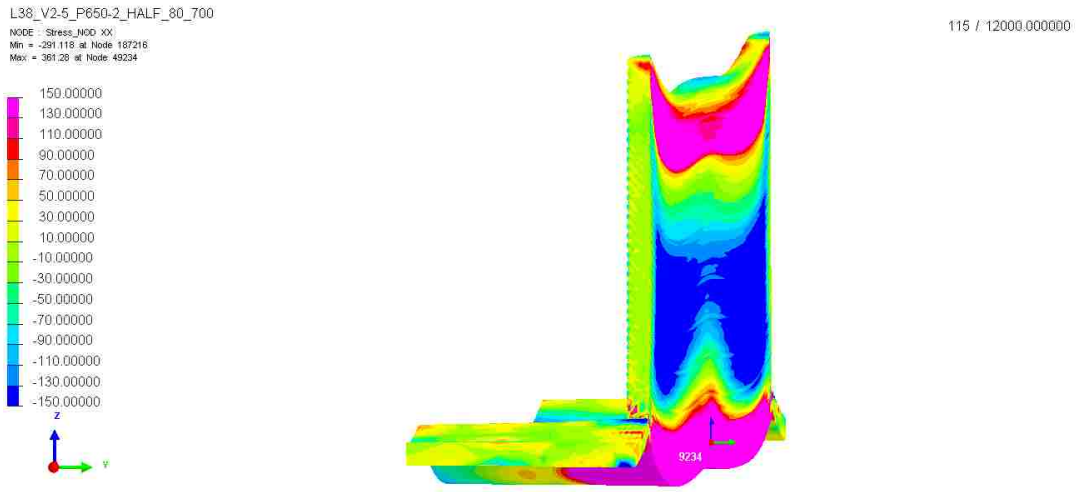

Figure 3.9 σ_{XX} - Longitudinal Residual stress of 3D printed 316L at heat input 325 J/mm Y-Z plane -cross section view

Figure 3.9 shows a cross section on the middle of the sample, as figure 3.5 is viewed from a different angle. From this side, the distortion is clear. It seems that the ends are higher than the center, also they have the lowest stress value. While comparing 3.9 with figure 3.10, the stresses' regions in figure 3.10 had a smaller area than the regions in figure 3.9. which means that the stresses inside the sample are in an 'intense' state.

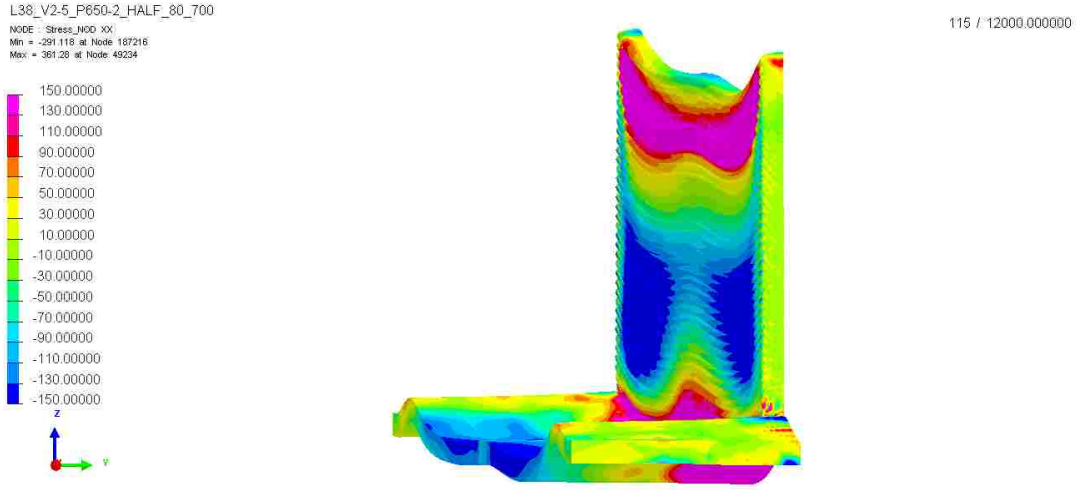

Figure 3.10 σ_{XX} - Longitudinal Residual stress of 3D printed 316L at heat input 325 J/mm Y-Z plane view

Figure 3.11 is an isometric view with slices selected parts and gives more insight into what happens inside the simulated part. It also shows the effects of the base on the printed part. It seems the base is in tension, with the printed part leads to different distortion shapes, if the printed part is cut from the base. In addition, the ends of printing part are not in the same pattern as the middle part. It is also clear here that the parts inside have much higher stresses than the parts outside.

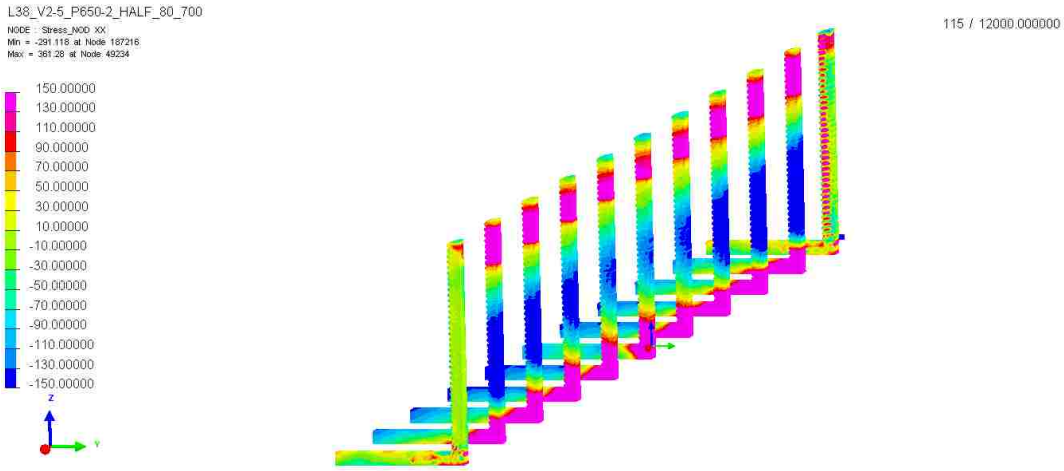

Figure 3.11 σ_{XX} -Longitudinal Residual stress of 3D printed 316L at heat input 325 J/mm Isometric-section-sliced parts view

First principle Residual Stress result of austenitic stainless-steel grade 316L with heat input 325 J/mm

The maximum principle residual stress gives a more general picture of the residual stress state than the contour plots of the σ_{XX} residual stress. As shown in figure 3.12, the contour is a cross section of the sample on the middle on the center line of the X axis. In this figure it appears that the first principle residual stress makes a “frame” around the sample and is very useful for determining the dimension of the frame in order to predict the actual stress distribution.. From figures 3.12 and 3.13, it is clear that the maximum stress value is 463.876 MPa in tension and the minimum is -83.1905 MPa in compression. It can also be observed from figures 3.12 and 3.13, that the stress divides the sample into two regions - the frame in tension and the active area in low compression, relatively. And that is applied on the both the contours, inside and outside.

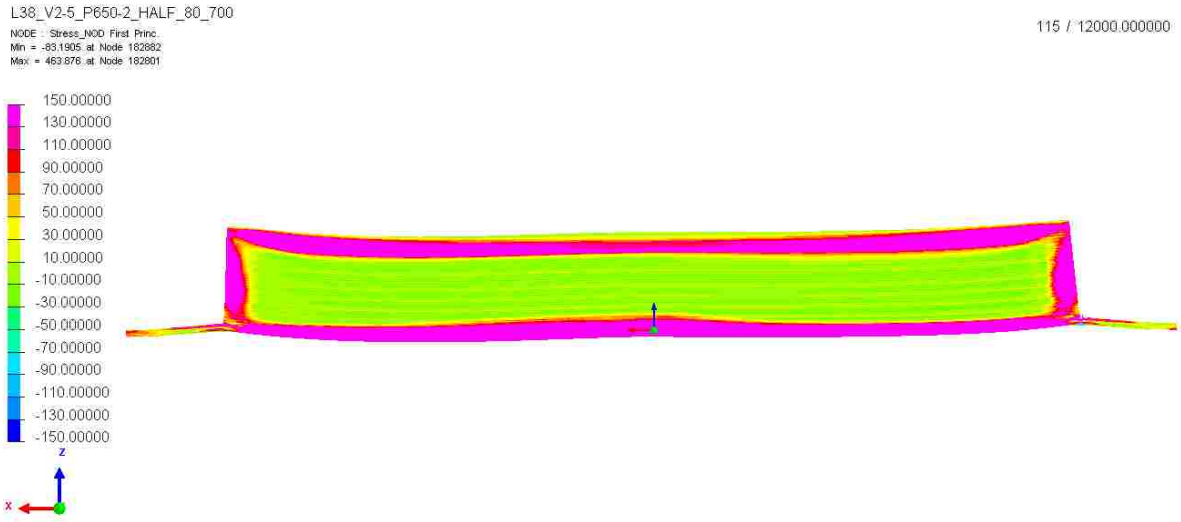

Figure 3.12 First Principal Residual stress of 3D printed 316L at heat input 325 J/mm X-Z plane -cross section view

Figure 3.13 First Principal Residual stress of 3D printed 316L at heat input 325 J/mm X-Z plane view

The figures 3.14 and 3.15 show the isometric views for the sample. These two figures show the base of the printing in low stresses, which means the stress averages are low on the base as compared to the frame of the printed part.

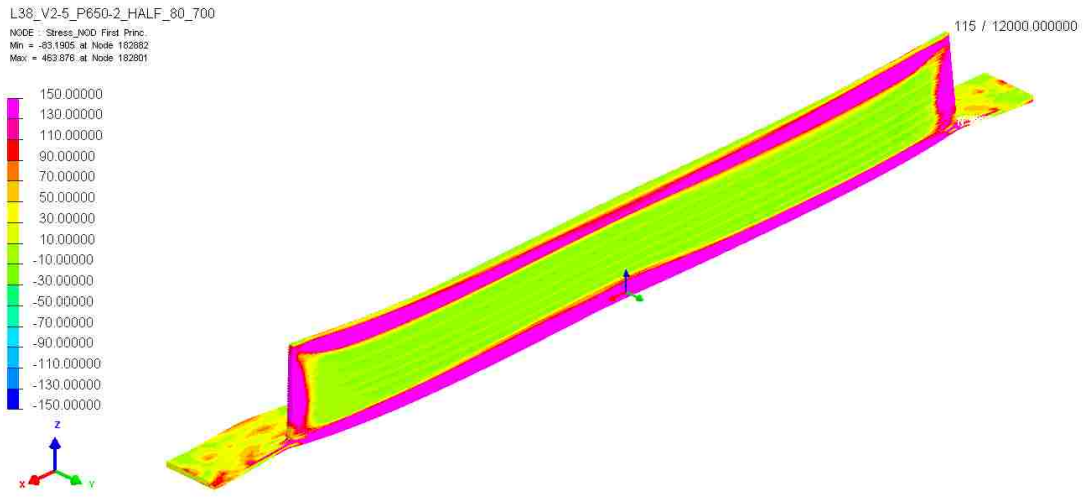

Figure 3.14 First Principal Residual stress of 3D printed 316L at heat input 325 J/mm Isometric-cross section view

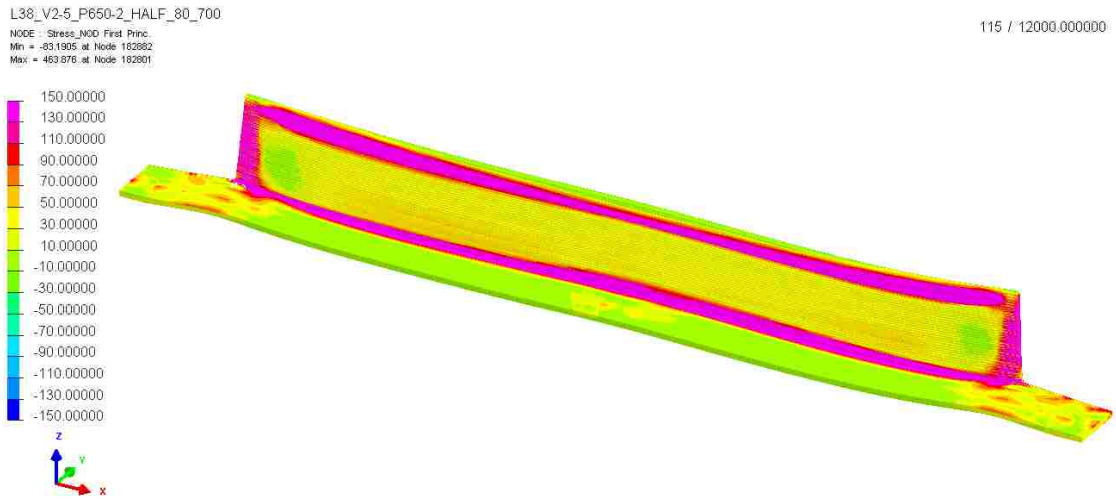

Figure 3.15 First Principal Residual stress of 3D printed 316L at heat input 325 J/mm Isometric view

In figures 3.16 and 3.17, the distortion is clear, but there is a unique occurrence between the layers. It seems that the layers inside are in compression mode while the areas between them are in tension mode. However, both these stresses are low as compared to the frame stresses around the active area.

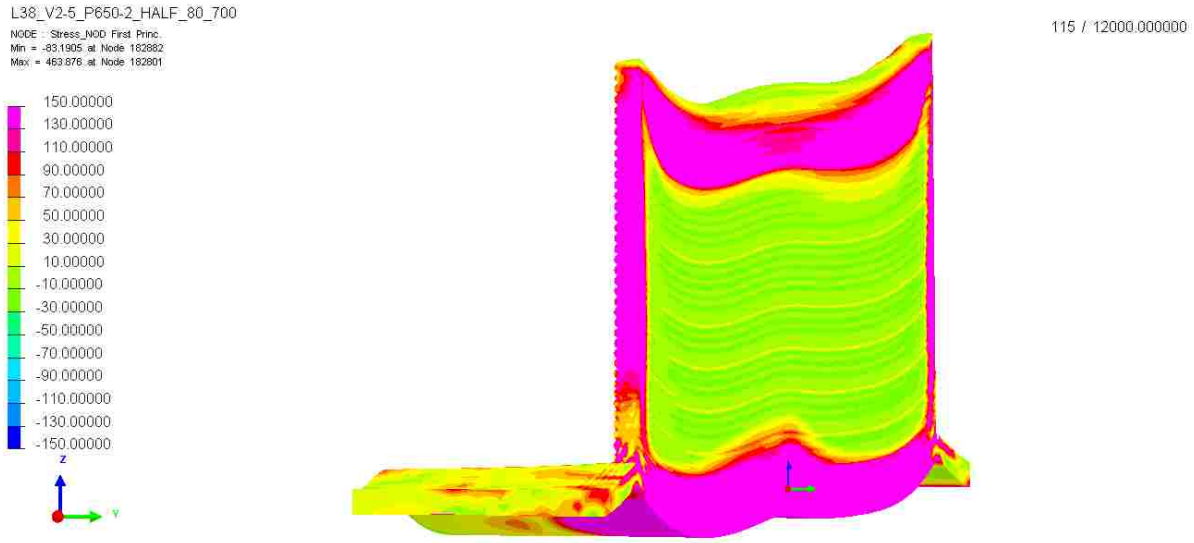

Figure 3.16 First Principal Residual stress of 3D printed 316L at heat input 325 J/mm Y-Z plane -cross section view

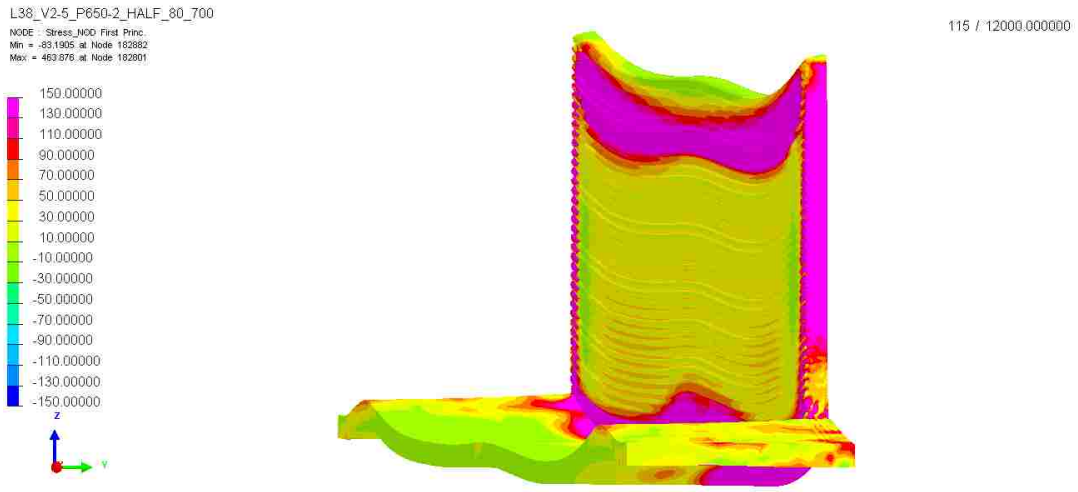

Figure 3.17 First Principal Residual stress of 3D printed 316L at heat input 325 J/mm Y-Z plane view

Figure 3.18 shows the sliced parts of the sample. In this figure the active area which has the lower first principle residual stress has a clear dimension and a clear edge for the cutting processes after printing. It could be because the stress frame has a certain level of layers, which for any 3D printing process has to be considered as a waste section.

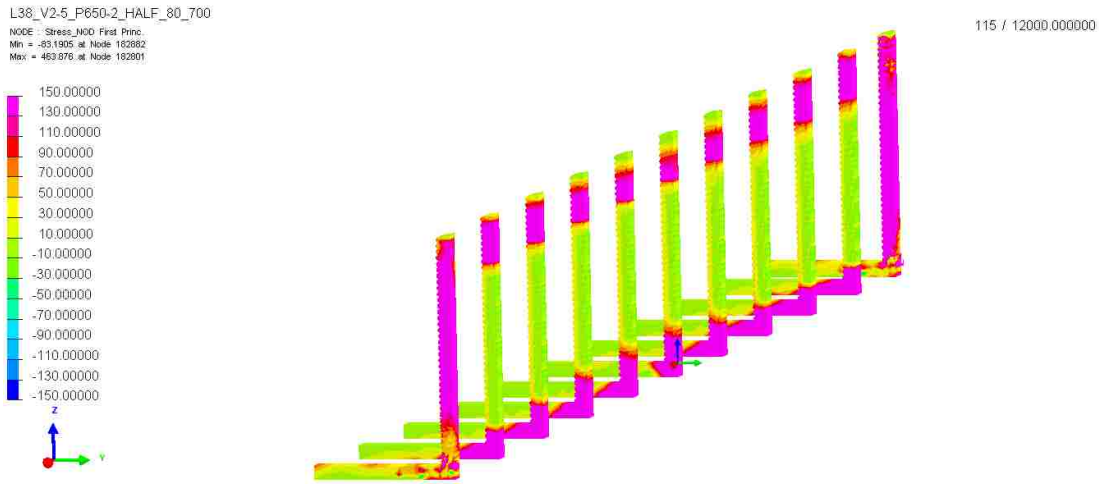

Figure 3.18 First Principal Residual stress of 3D printed 316L at heat input 325 J/mm Isometric-section-sliced view

Figures 3.19 shows the displacements on the Z-axis as curves for layers 3-14-25-36. These curves go below zero, the reason for which is the last free clamps, which distort the sample as if in a

vacuum, without limits. The highest displacement is around 15 cm at the beginning of the 3D printing. Also, the lowest distortion is between the center and the ends. From this figure it appears that the clamps affect the distortion in a destructive manner for the clamp at the center. But it could perhaps be good for other clamping conditions. The highest displacement point relative to the length of the sample is around 2%, a high undesirable value, as a benchmark for good tolerance demands in the industry.

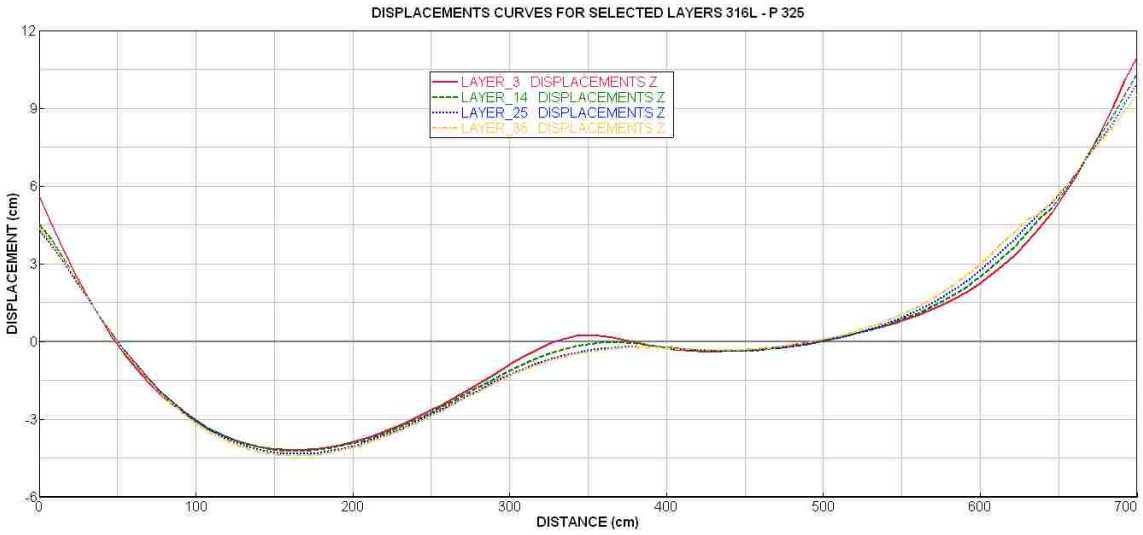

Figure 3.19 Displacements curves for Layers 3-14-25-36 of 316L , heat input 325 /mm after printing

Results of austenitic stainless-steel grade 316L at heat input 345 J/mm

As illustrated in the previous section, the heat input was 325 J/mm. For some nodes it does not meet the melting temperature. So, this case uses a higher heat input, which was determined by testing different heat inputs. Figure 3.20 shows the middle nodes' temperature curve for the same parameters in the last section but with heat input as 345 J/m. These temperature curves reach the melting temperature point twice. For the third cycle it reaches 1200°C. But this is a pattern different from the previous section. In this case (345 J/mm) the peak temperature for the first 16 layers is lower than the previous layers by about 200 degrees Celsius.

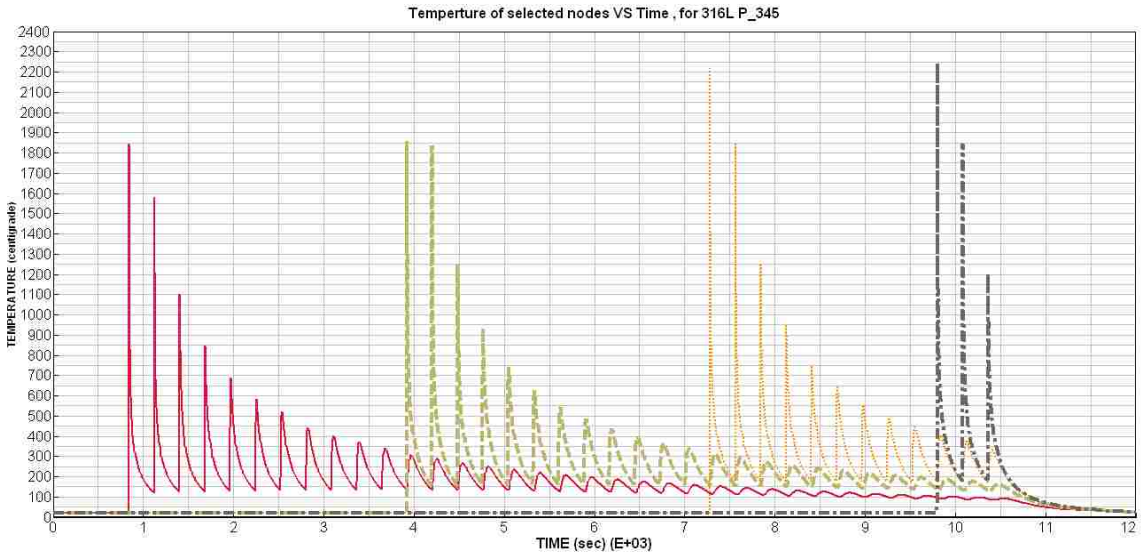

Figure 3.20 Temperature behavior of Middle nodes for 316L, heat input 345 J/mm of Layers 5,16,28, and 37

Figure 3.21 shows the temperature curves for the side-touch nodes, with the heat input as 345 J/mm. The problem of nodes with non-meeting melting temperature is thus resolved. All the side-touch nodes reach the melting-point temperature twice in this case, just as expected in the lab experiment.

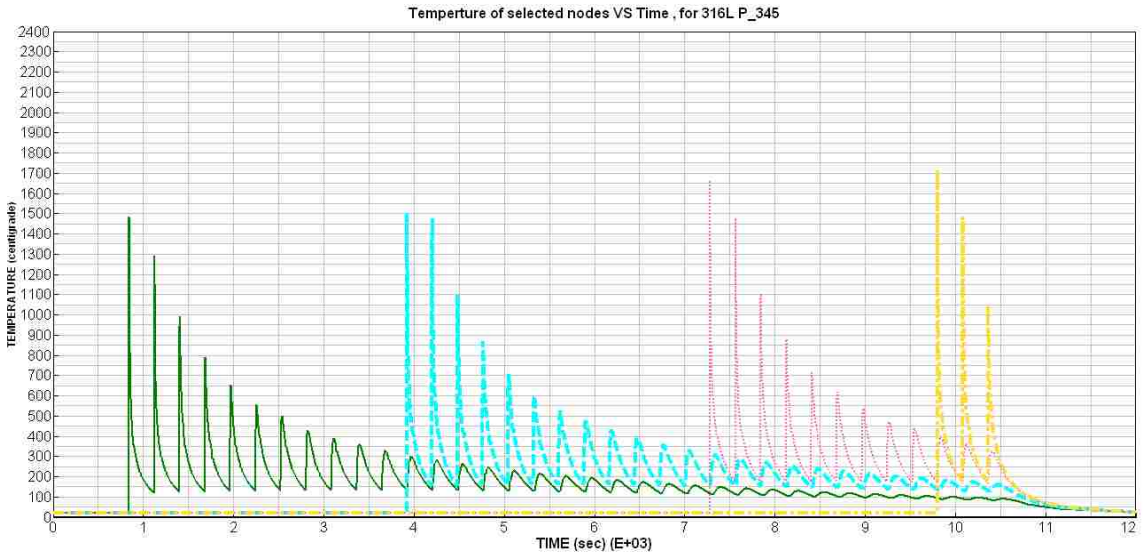

Figure 3.21 Temperature behavior of side-touch nodes for 316L, heat input 345 J/mm of Layers 5,16,28, and 37

The last temperature case is that of side nodes as in figure 3.22, which must melt at least once. In this case, with the new heat input, the peak temperature for these nodes reaches the melting point. For the second cycle, the temperature is lower than the melting temperature by around 200 degrees Celsius, as observed for each node.

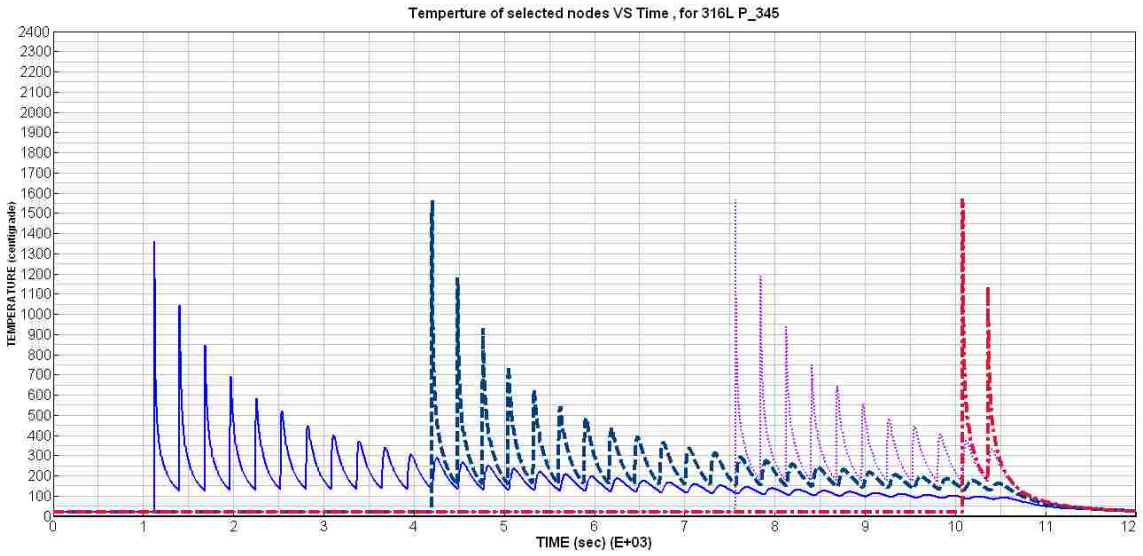

Figure 3.22 Temperature behavior of side nodes for 316L, heat input 345 J/mm of layers 5,16,28, and 37

σ_{XX} - Residual Stress result of austenitic stainless-steel grade 316L at heat input 345 J/mm

The main objective for repeating these simulations with different heat inputs was to observe the difference between the residual stresses of the sample nodes, whether they meet the melting-point temperature or not. For exhibiting σ_{XX} residual stress, it would suffice to present the last three figures of the previous section. Comparing information between figure sets 3.9, 3.10, 3.11 and 3.23, 3.24, 3.25, it seems they are similar in terms of contours and regions. Therefore, for σ_{XX} residual stress the melting-point temperature does not affect the final result of the stress, as long as the peak temperature of the nodes reaches near the melting-point temperature.

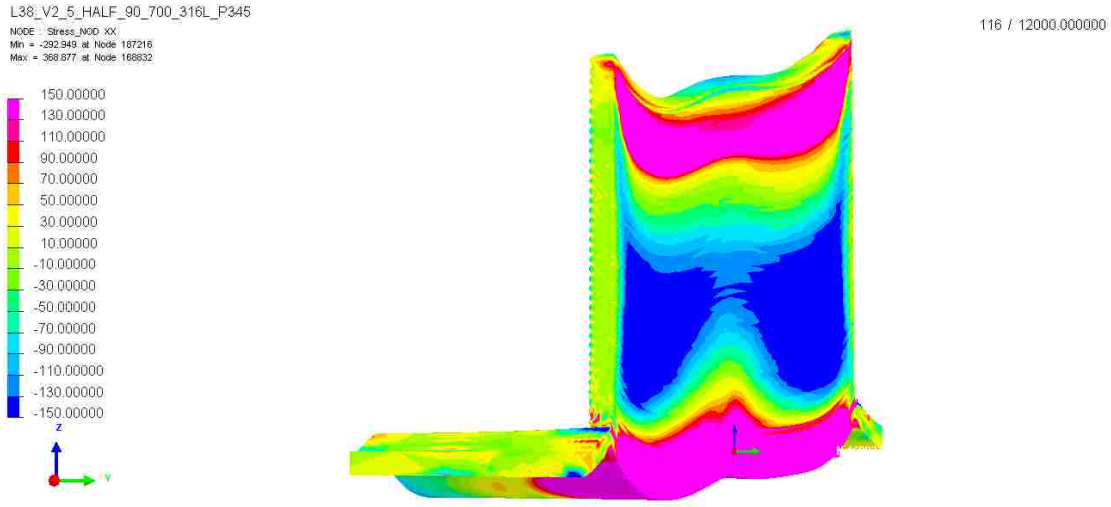

Figure 3.23 σ_{XX} - Longitudinal Residual stress of 3D printed 316L at heat input 345 J/mm Y-Z plane -cross section view

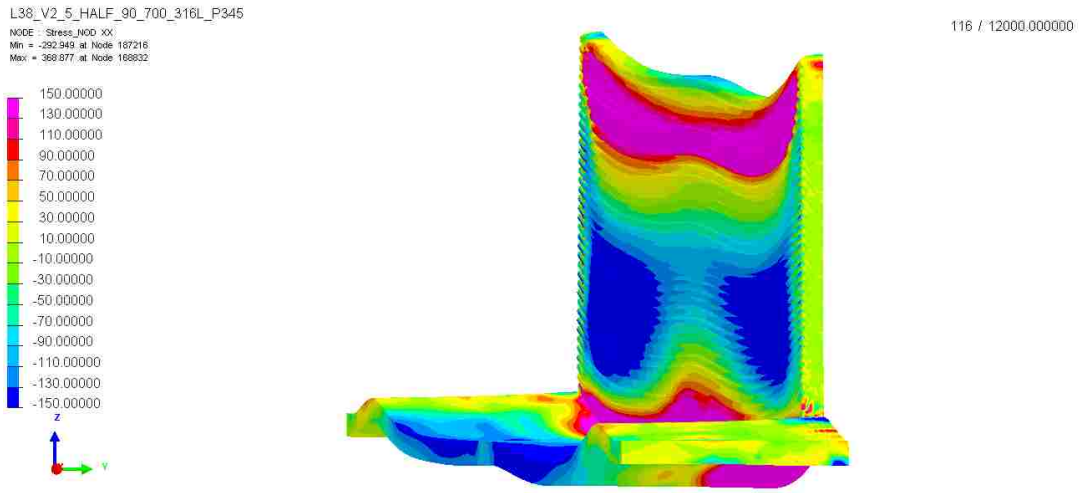

Figure 3.24 σ_{XX} - Longitudinal Residual stress of 3D printed 316L at heat input 345 J/mm Y-Z plane view

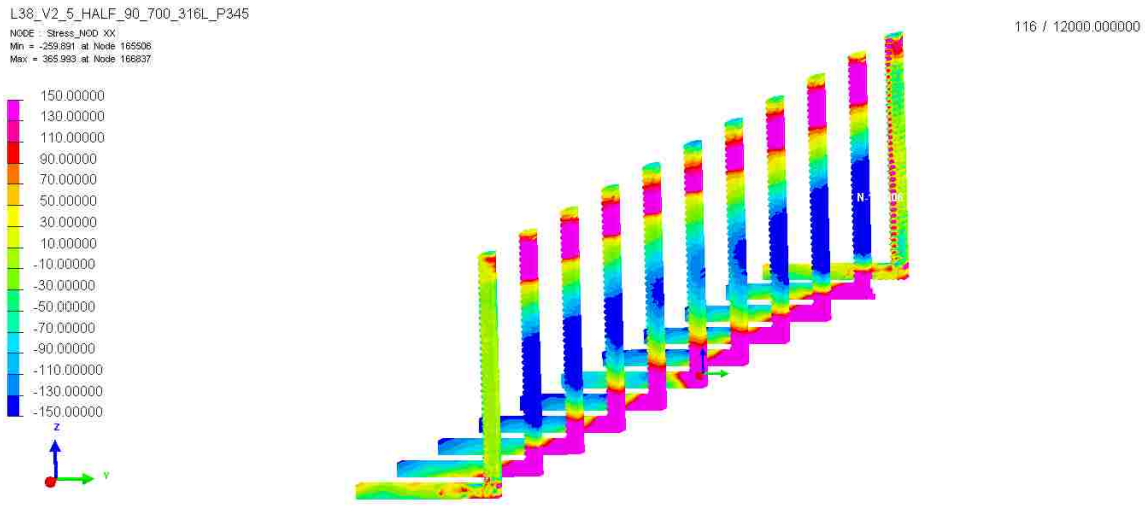

Figure 3.25 σ_{XX} -Longitudinal Residual stress of 3D printed 316L at heat input 345 J/mm Isometric-section-sliced view

First principle Residual Stress result of austenitic stainless-steel grade 316L at heat input 345 J/mm

Also, for first principle residual stresses, it does not need to compare each aspect. It is enough to compare three figures between these cases with different heat input. Comparing figure sets 3.16, 3.17, 3.18 and 3.26, 3.27, 3.28, they look similar as well. So as in σ_{XX} stress, the First principle does not alter much across different heat inputs.

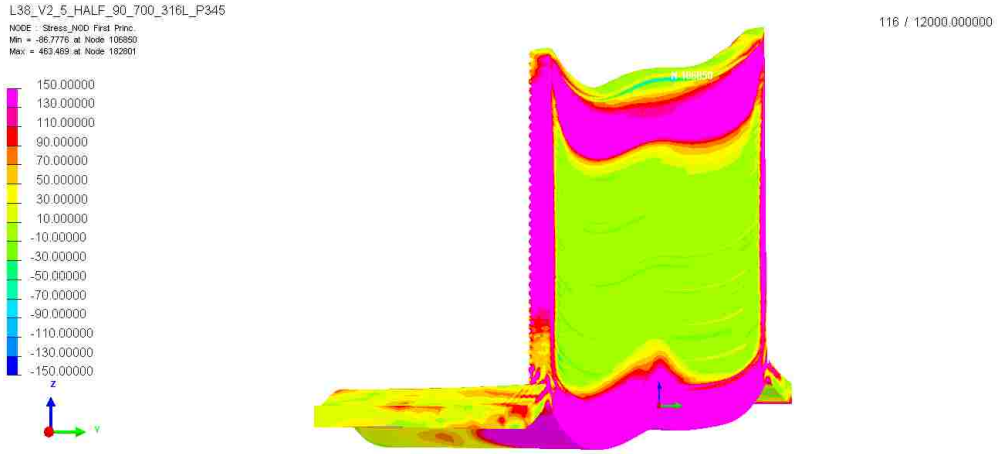

Figure 3.26 First Principal Residual stress of 3D printed 316L at heat input 345 J/mm Y-Z plane -cross section view

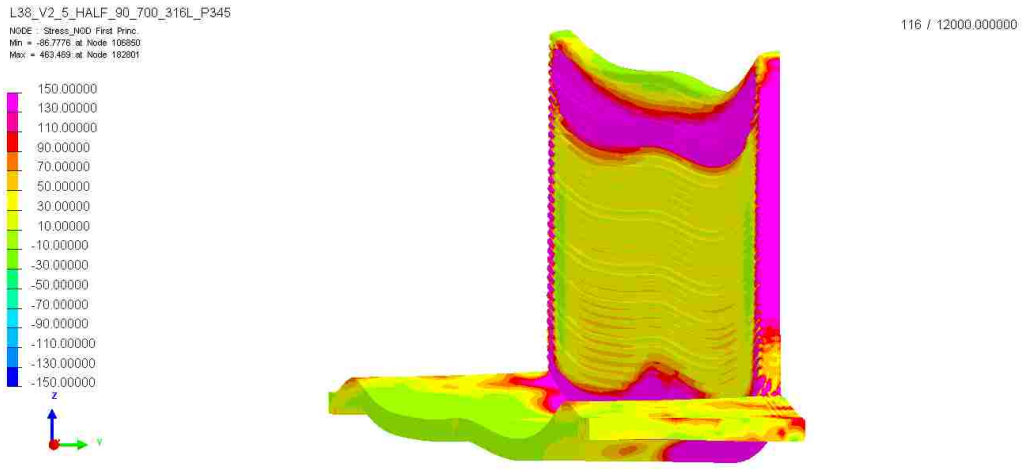

Figure 3.27 First Principal Residual stress of 3D printed 316L at heat input 345 J/mm Y-Z plane view

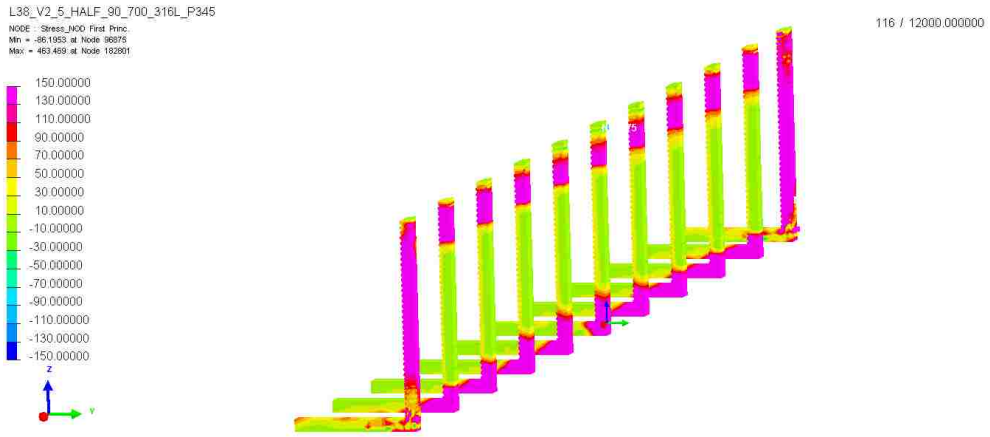

Figure 3.28 First Principal Residual stress of 3D printed 316L at heat input 345 J/mm Isometric-section-sliced view

In addition to the above comparisons, between figure 3.23 and figure 3.28, it is observed that, in general, the displacement curves' shapes are the same. However, there is a difference at node ID 150. The concave of the case with heat input 345 J/mm is slightly lower than the case where the heat input is 325 J/mm. The reason could be the increase in heat input. However, they follow the same pattern, as seen in the graphs.

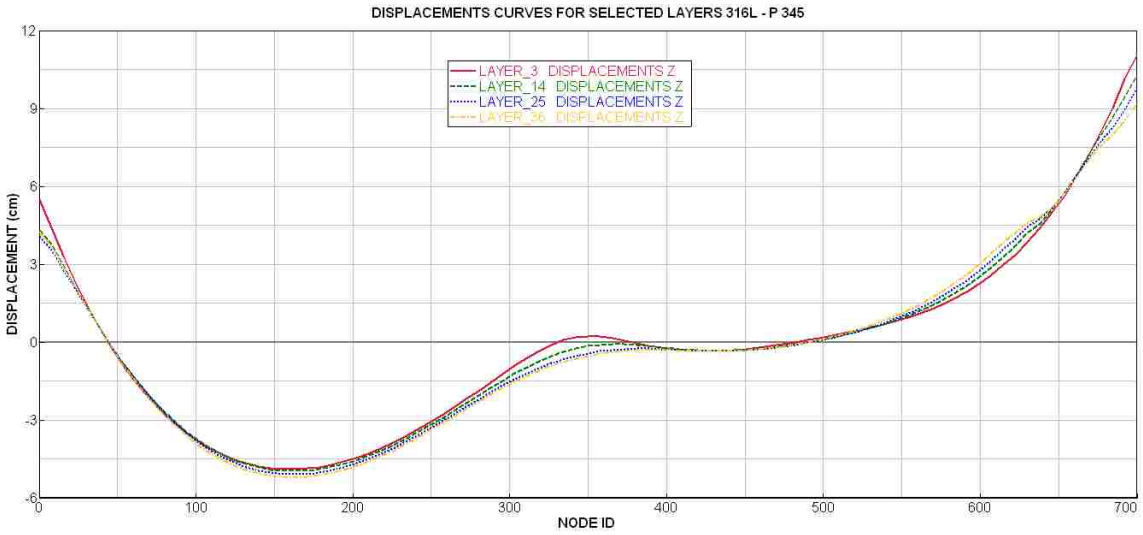

Figure 3.29 Displacements curves for Layers 3-14-25-36 of 316L , heat input 345 /mm after printing

Results for Low carbon steel S355J2G3 at heat input 405 J/mm

The third case is that of a 3D printing simulation process for the same parameters as in the first case and as shown in table 3.1. This is with a different material - Low Carbon Steel S355J2G3. This material melts around 1500°C, so it needs a higher heat input, the appropriate heat input value for this case is 405 J/mm. Table 3.4 shows the chemical composition of Low Carbon Steel S355J2G3, as it is used in the simulation software SYSWELD. Also, it has the mechanical properties shown in Table 3.5.

Table 3.4 : Chemical composition of Low carbon steel S355J2G3 from ESI database

Element	C	Mn	P	S	Si
%	0.18	1.6	0.035	0.035	0.55

Table 3.5 : Mechanical Properties of Low carbon steel S355J2G3

Element	Tensile strength, min		Yield strength, min		Hardness, max	
S355J2G3	ksi	MPa	ksi	MPa	Brinell	Rockwell
	98	680	50	345	187	90

For the same procedure, the nodes described in figure 3.1 have a temperature description for the layers. Figure 3.30 shows the temperature behavior of the middle nodes for layers 5,16,28, and 37 in this case. As the material melts around 1500°C, the peak temperature of the layers exceeds 2200°C and in the second cycle it reaches 1800°C, both of which are above the melting point. But for the third cycle, the temperature of the middle nodes for all layers reach 1250°C, which is below the melting point. This is the objective for re-melting the center of the layers for combining any two layers.

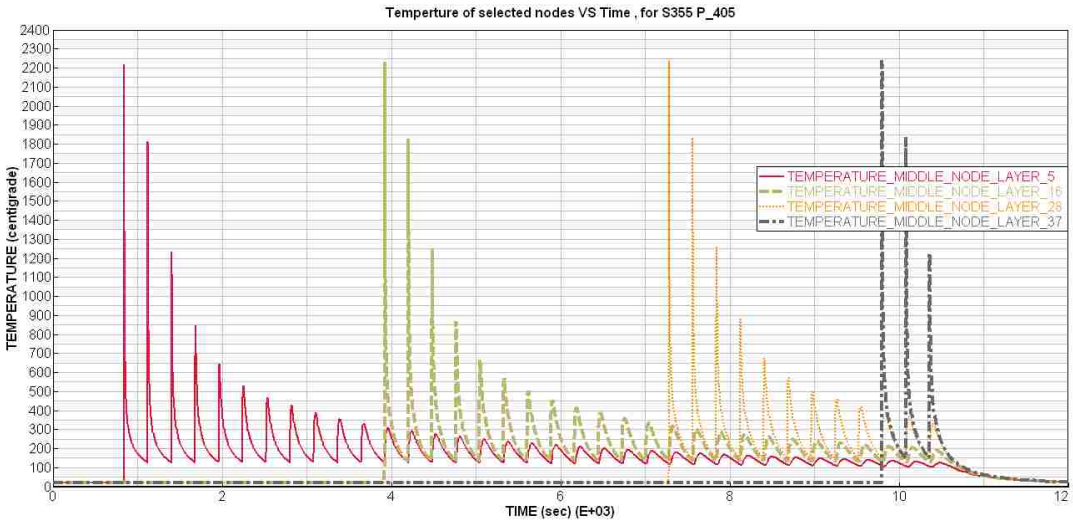

Figure 3.30 Temperature behavior of Middle nodes for S355, heat input 405 J/mm of Layers 5,16,28, and 37

Figure 3.31 describes the temperature for the side-touch nodes, as described in the earlier figure 3.1. These nodes must reach the melting point twice as the middle nodes but with a lower temperature rate. The curves in figure 3.31 are represented for layers 5, 16, 28 and 37. These nodes reach 1700°C for the first deposit and 1500°C for the second deposit. This means that the nodes melted twice. But for the third cycle all the layers do not exceed 1050°C, which is below the melting point.

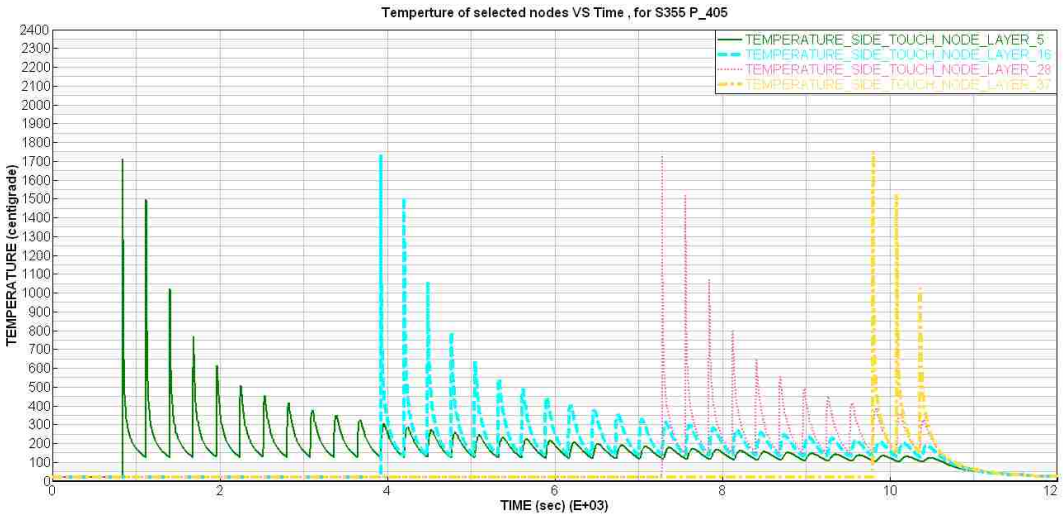

Figure 3.31 Temperature behavior of side-touch nodes for S355, heat input 405 J/mm of Layers 5,16,28, and 37

In contrast to the middle and side-touch nodes, side nodes must melt once. If the side nodes melt again, it means that the heat input is too high, and which makes the layers to not fit into each other. Figure 3.32 describes the temperature of these nodes for the selected layers - 5, 16, 28, and 37. All these layers exceed the melting point by a 100 degree Celsius. But for the second cycle none of the layers go beyond 1150°C, which is below the melting point by 300 degree Celsius.

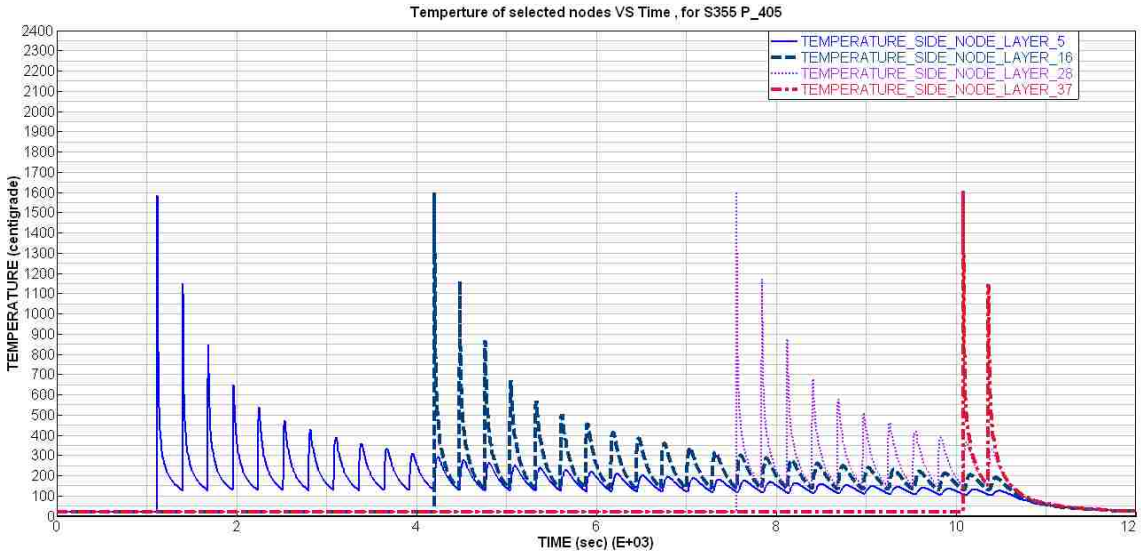

Figure 3.32 Temperature behavior of side nodes for S355, heat input 405 J/mm of layers 5,16,28, and 37

σ_{XX} - Residual Stress result of Low carbon steel S355J2G3 at heat input 405 J/mm

The most important residual stresses in any welding processes are the longitudinal residual stress which is σ_{XX} residual stress in this case. So, the first result of this case is for σ_{XX} residual stress. Figure 3.33 shows a color contour plot that describes the distribution of the σ_{XX} residual stress around the sample. In figure 3.33 the stress has a more complex distribution than in the case of stainless steel 316L. The maximum residual stress is 593.29 in tension and the minimum is -545.052. In compression, these values are higher than the yielding stress. This figure below shows the symmetric plane of the middle, around the X-axis. The last three deposited layers of the sample have stress in comparison, while the layers underneath them are in tension. That happens directly without any gradual changes in the stress values. The most dominant stress type is tension with a small area of compression on the sides. Also, there is a hump on the center which may be caused by the clamps because the clamps prevent the printed part from distortion, which is to stress. In fact, after cooling, when the clamps are removed the stresses could not change the shape of the sample, thereby, turning to residual stresses.

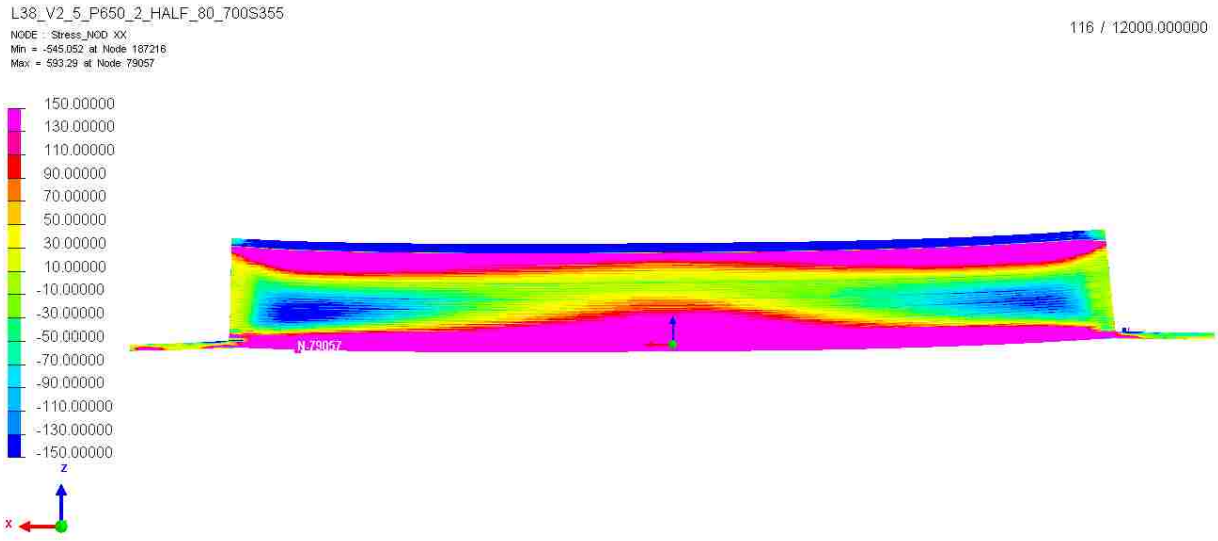

Figure 3.33 σ_{XX}- Longitudinal Residual stress of 3D printed S355 at heat input 405 J/mm X-Z plane -cross section view

Figure 3.34 shows different dominant stress types from outside the sample, this side of the sample on the figure generally in compression state. Also, it has the last three deposited layers, but with a sharp little gradual transformation between compression and tension states. The effect of the clamps still exists on this side as well.

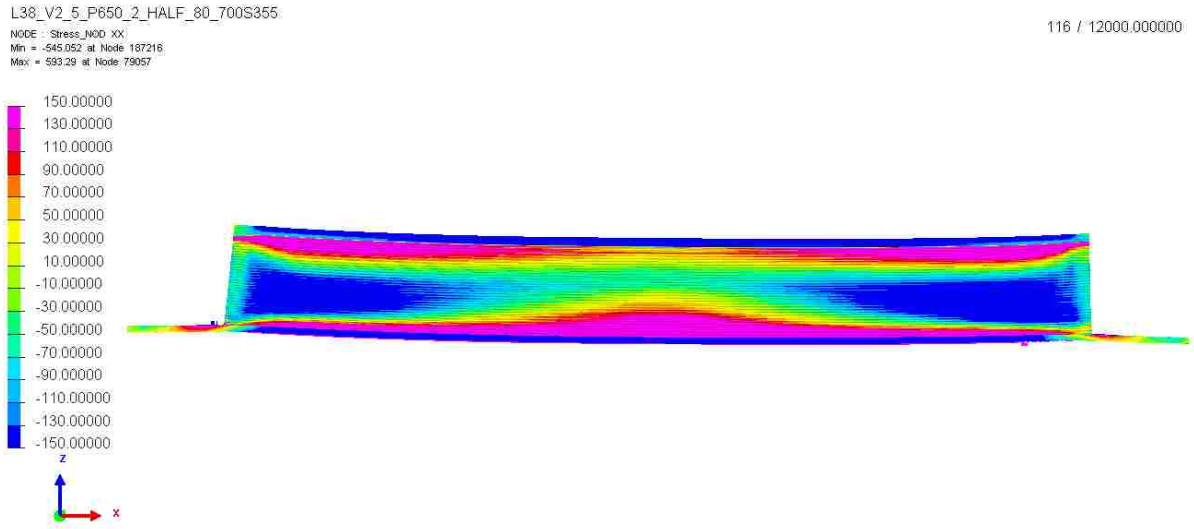

Figure 3.34 σ_{XX}- Longitudinal Residual stress of 3D printed S355 at heat input 405 J/mm X-Z plane view

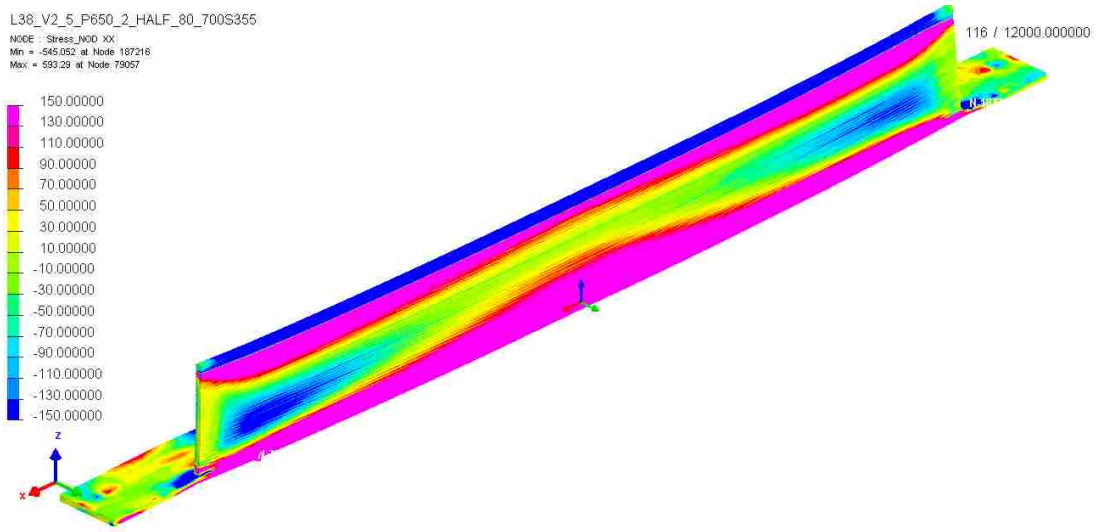

Figure 3.35 σ_{XX}- Longitudinal Residual stress of 3D printed S355 at heat input 405 J/mm Isometric-cross section view

Figures 3.35 and 3.36 are isometric views for the sample, from these figures it is clear that the start and the end of the printing (welding) path have the most effects on the base. The base generally in compression state, which makes sense; because the melting layers shrink and grab the sides of the base with it. While the ends of the base are in a low value of stresses comparing to the center of it.

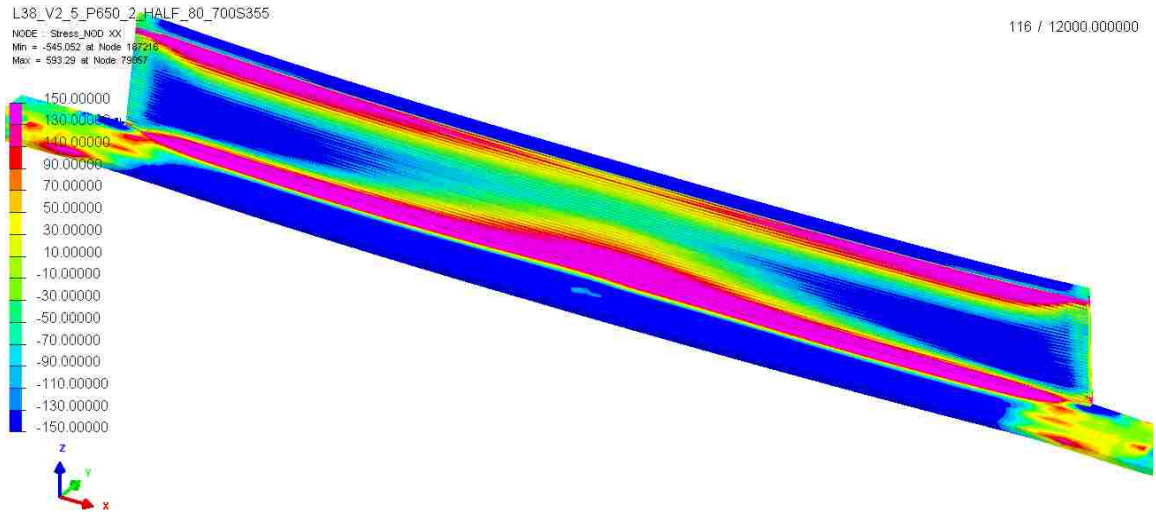

Figure 3.36 σ_{XX}- Longitudinal Residual stress of 3D printed S355 at heat input 405 J/mm Isometric view

Figures 3.37 and 3.38 describe the plane Z-Y with little of rotation. For the same data σ_{XX} residual stress, these figures describe clearly how the tension stresses grow up from outside of the plate to inside it; while the last three layers are in different pattern. Also, these figures show the displacements of the base and the plate as one curve; which is not the case in the sample of 316L. Furthermore, the range of the distortion is lower than the sample of 316L.

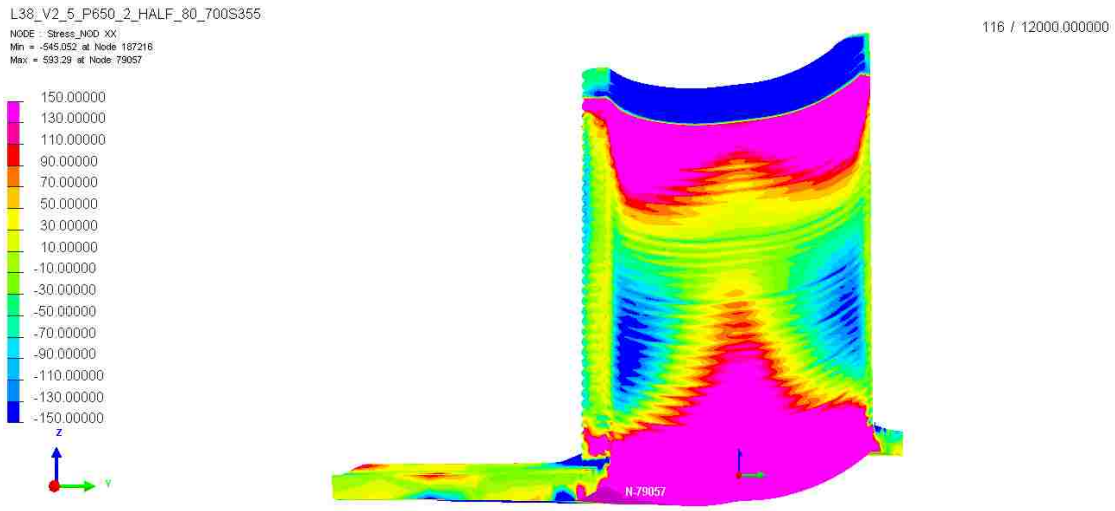

Figure 3.37 σ_{XX}- Longitudinal Residual stress of 3D printed S355 at heat input 405 J/mm Y-Z plane -cross section view

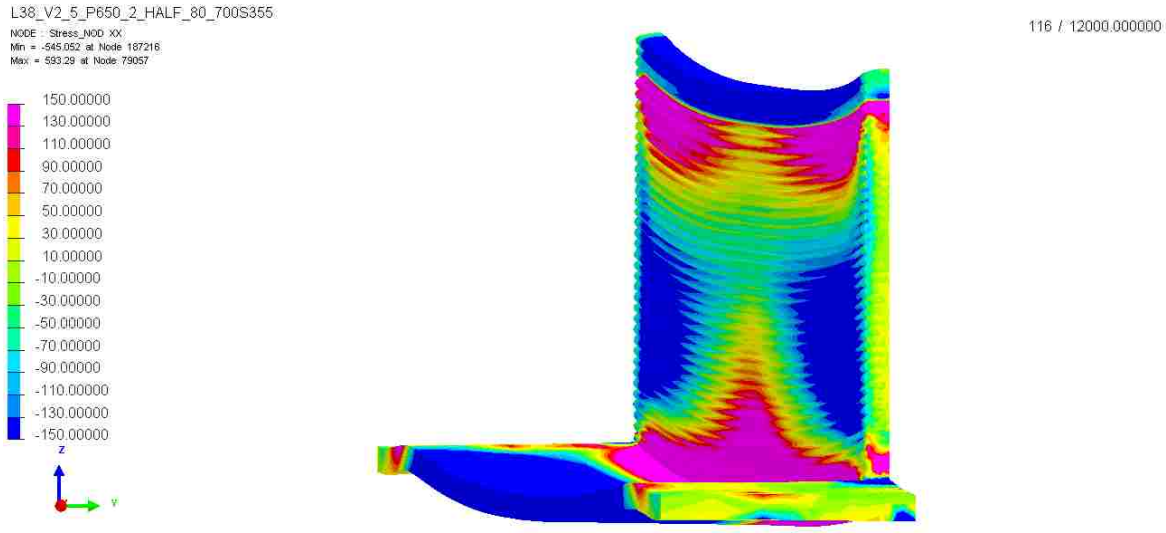

Figure 3.38 σ_{XX}- Longitudinal Residual stress of 3D printed S355 at heat input 405 J/mm Y-Z plane view

Figure 3.39 is a sliced parts of the isometric view of the σ_{XX} residual stress. It seems that the residual stresses inside the cuts are not encompassing the four regions. The contact area between the base and the printed part is in tension, while the second region is in compression and the third region is in tension below the last three layers. The last three layers have a pattern that is different from the others. So, it may be the same as in 316L for the divided regions pattern, but with different range of stress value.

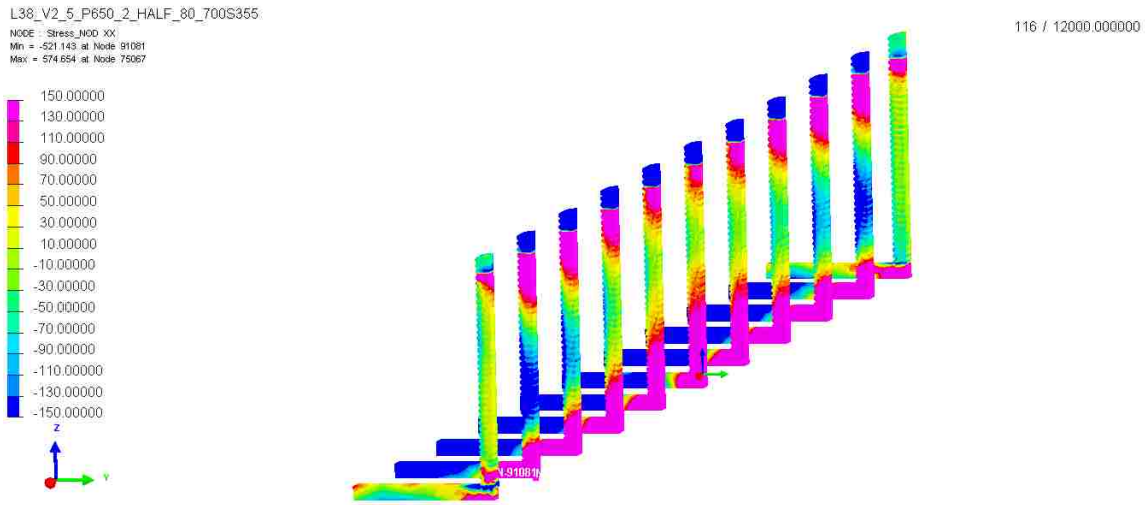

Figure 3.39 σ_{XX}-Longitudinal Residual stress of 3D printed S355 at heat input 405 J/mm Isometric-section-sliced view

First principle Residual Stress result of Low carbon steel S355J2G3 at heat input 405 J/mm

Figure 3.40 is a contour representing the First principle residual stress for internal face from the cross section at the center of the sample. In this figure the stresses are divided into three regions. The last three layers, as in σ_{XX} residual stress, have the lowest rate as compared to other regions. The second region is a frame surrounding the center with tension stresses and it gets high at the origin because of the clamps. The third region is the center which is in between tension and compression states. The maximum stress point is 593.291, in tension, and the minimum is -208.029, in compression.

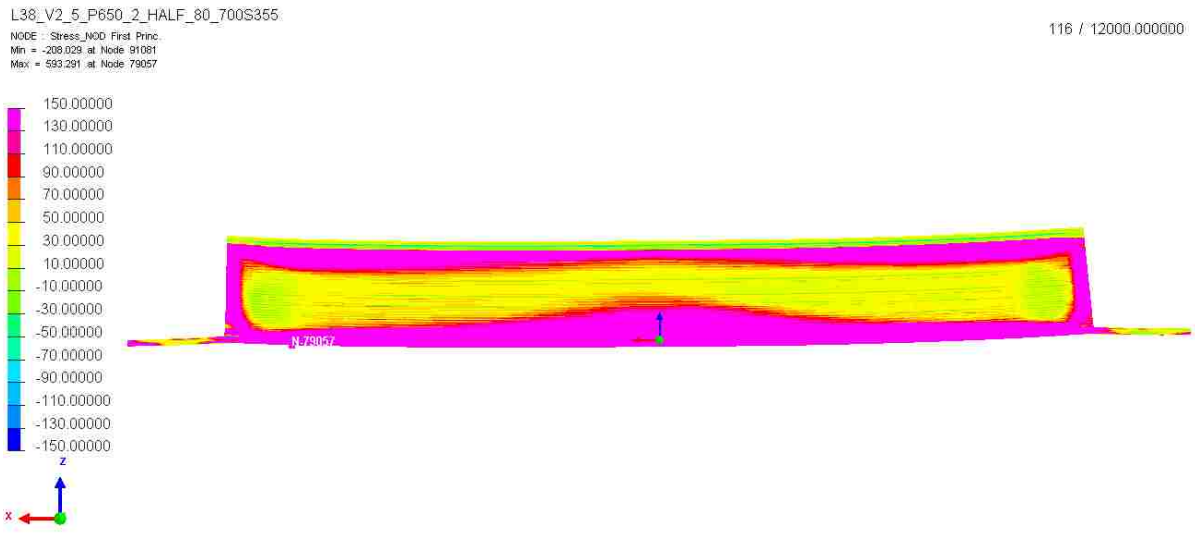

Figure 3.40 First Principal Residual stress of 3D printed S355 at heat input 405 J/mm X-Z plane -cross section view

Figure 3.41 describes the external face of the sample which is the opposite face of figure 3.40. Figure 3.41 has the same divided regions, but with different dimensions. Moreover, the stress rate of the internal face is in contrast to the external face. In other words, the external surface

of the sample has the First principle residual stress in low compression, while the inside of the printed part is in tension state.

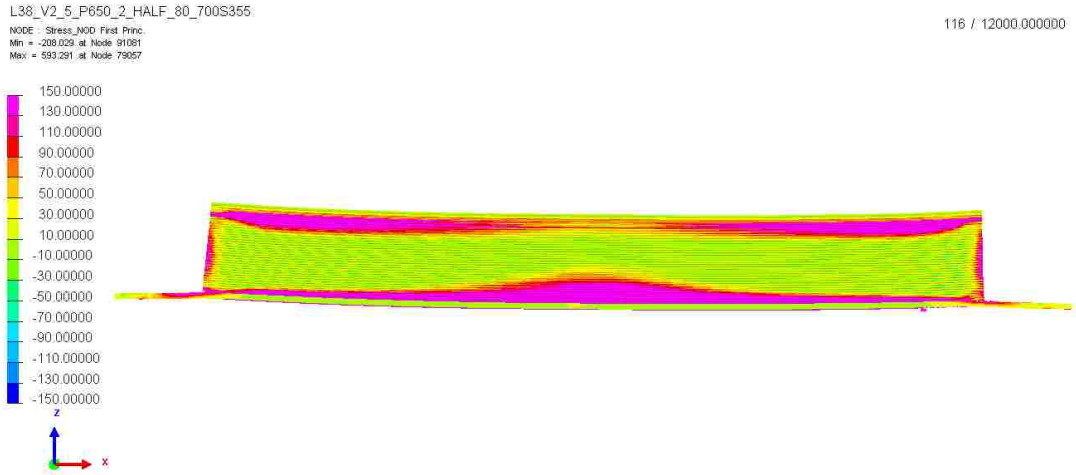

Figure 3.41 First Principal Residual stress of 3D printed S355 at heat input 405 J/mm X-Z plane view

Figure 3.42 and 3.43 are isometric views of the same sample. In these two figures, the base area around the printed part is in tension, while the rest of the base area is in low compression, except the ends of the base, which have a combined stress.

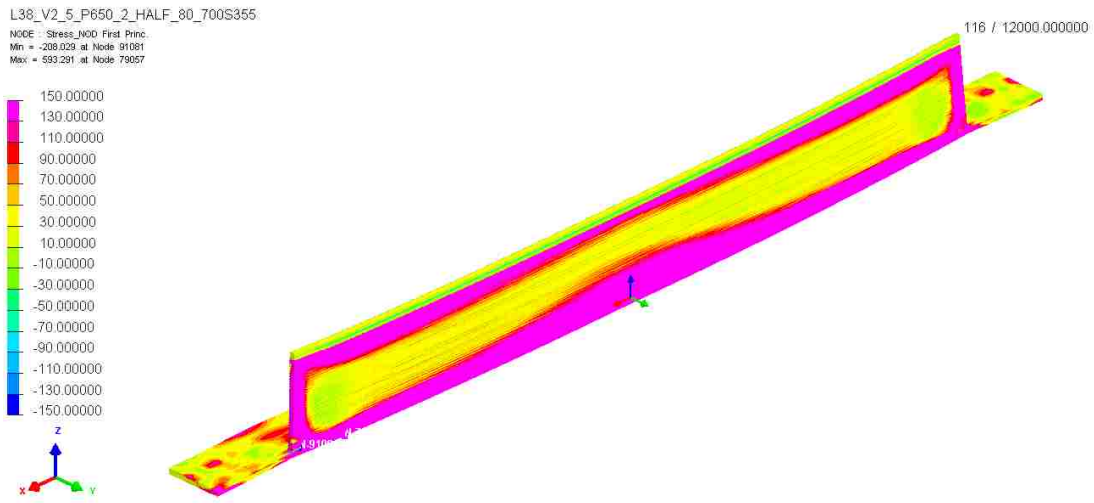

Figure 3.42 First Principal Residual stress of 3D printed S355 at heat input 405 J/mm Isometric-cross section view

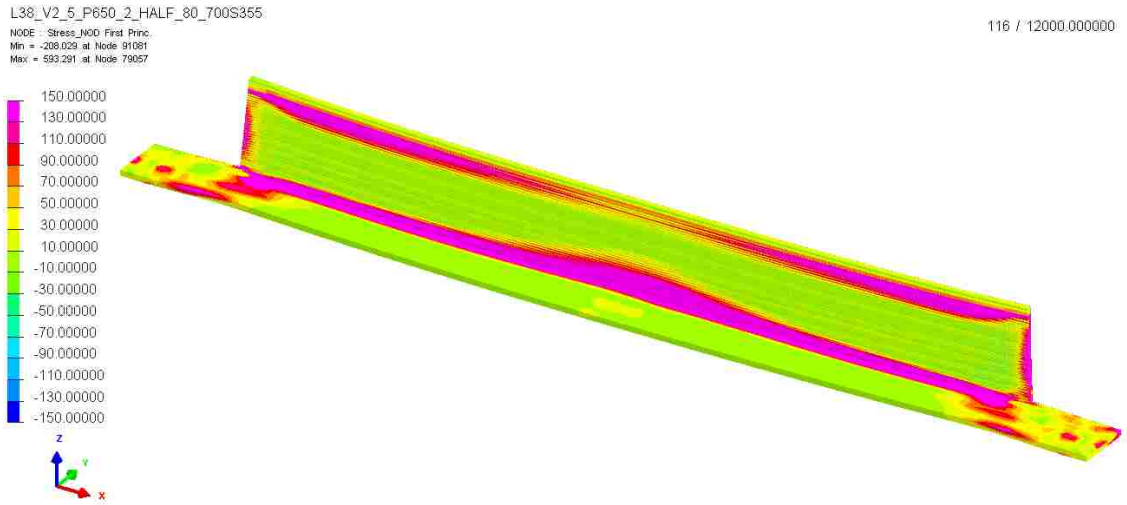

Figure 3.43 First Principal Residual stress of 3D printed S355 at heat input 405 J/mm Isometric view

Figures 3.44 and 3.45 show the last three layers clearly in a different pattern, as what happens in longitudinal stress. Also, in these two figures, the boundaries of any layer are in a state different from the layer itself. This may be because of the re-melting processes during printing. Also, it is observed that the ends of the printed part are in complete tension state.

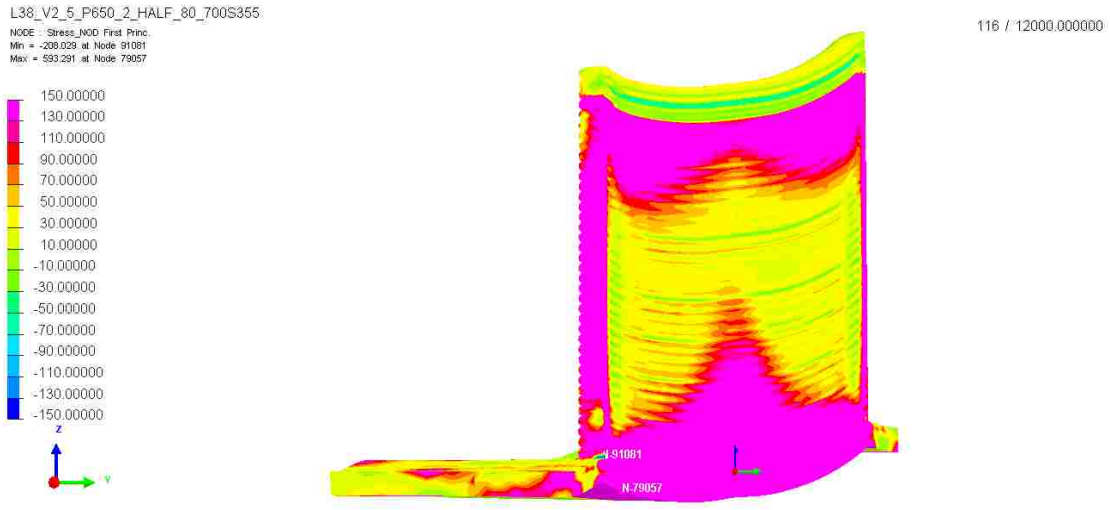

Figure 3.44 First Principal Residual stress of 3D printed S355 at heat input 405 J/mm Y-Z plane -cross section view

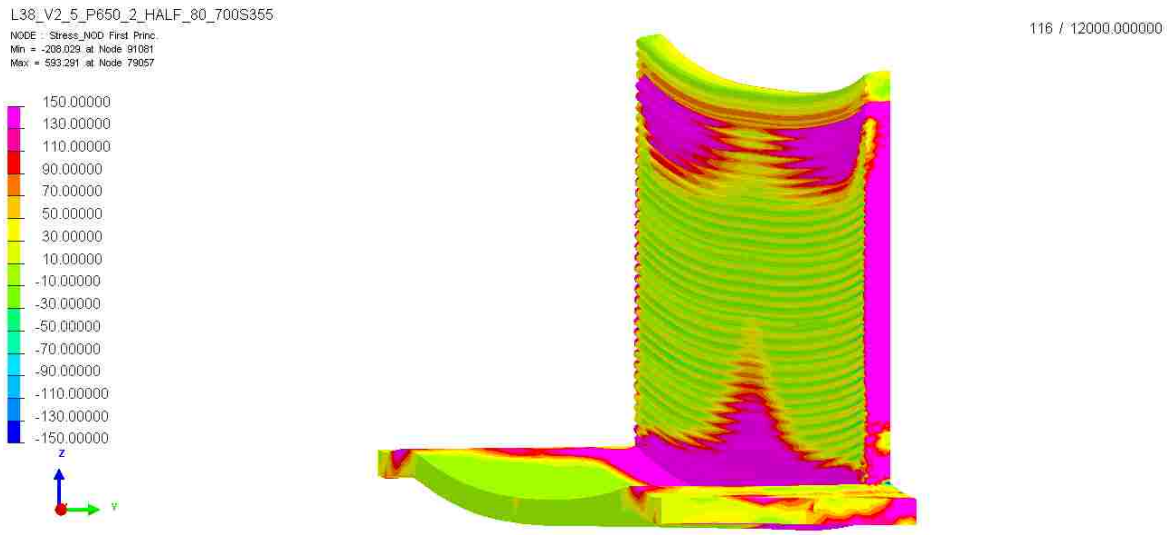

Figure 3.45 First Principal Residual stress of 3D printed S355 at heat input 405 J/mm Y-Z plane view

Figure 3.46 is a sliced parts of the sample. It shows how the stresses transform from the outside of the surface to the inside. Also, it shows how the base holds the printed part using tension stress. In fact, the ends of the printed part are in complete tension stress state. So, the frame is not a rectangular but resembles that of sunglasses, somewhat.

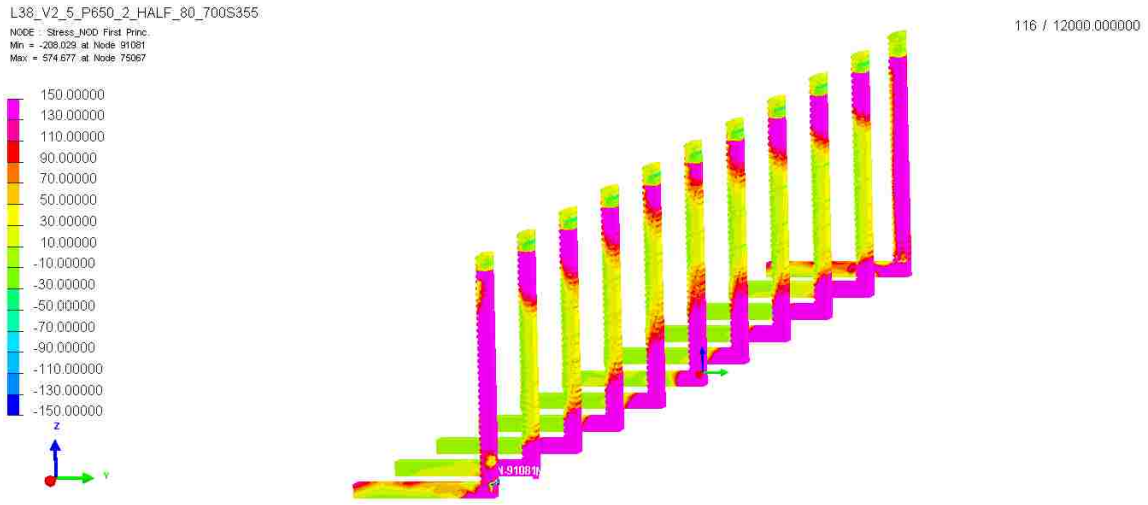

Figure 3.46 First Principal Residual stress of 3D printed S355 at heat input 405 J/mm Isometric-sectioncut-sliced view

Figure 3.47 has curves of Z-axis displacement of selected layers 3-14-25-36. These curves take an arc shape with little distortion in the middle. The sample moves to the negative Z-axis, which is practically impossible, since in real life there would be some support, for e.g. a table holding it. But in simulation processes, the clamps are free after the 3D printing processes is over, which is the cause for the negative sign. If this is factored, the maximum displacement would be around 8 cm, which is 1% of the total sample length.

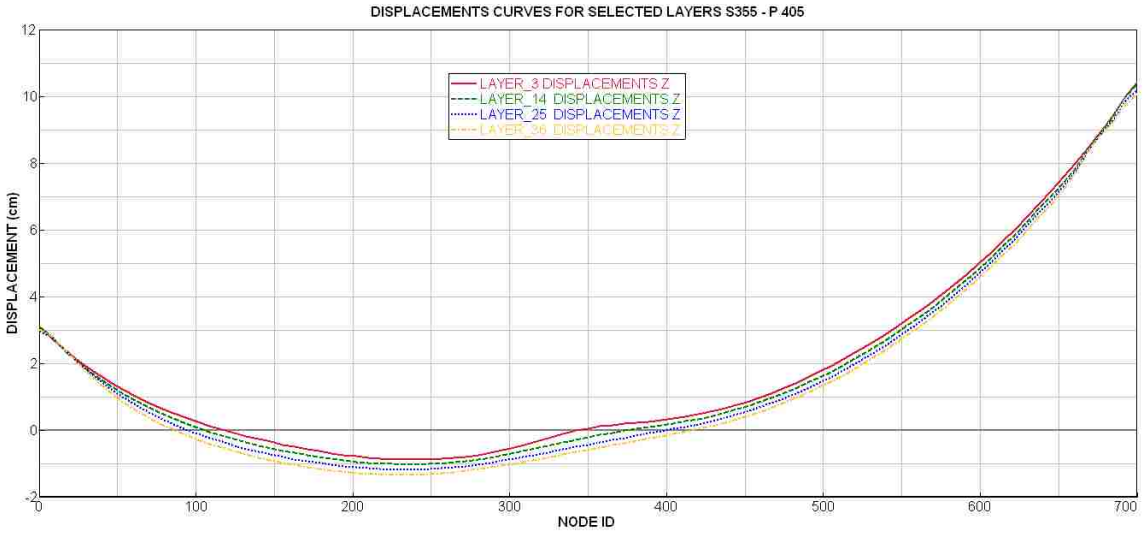

Figure 3.47 Displacements curves for Layers 3-14-25-36 of S355 , heat input 405 /mm after printing

Discussion

These results are made to compare between the residual stresses behaviors of two types of materials. In this case, they were - Austenitic stainless-steel grade 316L and Low carbon steel S355J2G3. These will be tested and validated subsequently with reference to an experimental sample in the future. There are two individuals' sections – one for austenitic stainless-steel grade 316L and the other for Low carbon steel S355J2G3.

In this study, there were two result sections for the austenitic stainless-steel grade 316L - one had heat input rate of 325 J/mm and the other one had 345 J/mm. For lower heat input, the sample nodes did not meet the melting temperature in certain cases, for e.g. the side nodes. Therefore, for these two results, the temperature of the nodes did not affect the final residual stress result so long as the temperature of the nodes reach close to a difference of less than almost200 degree Celsius. In general, the result looks similar but are really not identical; In fact, for the maximum and the minimum temperatures, they appear the same.

In conclusion, the methodology of employing the Welding heat input law or using Smart Weld software are very useful means to predict the appropriate heat input required to produce an explainable result for evidencing residual stresses.

So, the comparison is between two results, instead of three, since the heat input does not impact the result. In general, the stainless-steel result depicts the effect of lower longitudinal and first principle residual stress more, as compared to carbon steel. Though in both materials the residual stress types exceed the yielding strength, they do not suffice the tensile strength parameters.

For the longitudinal residual stress, in this case σ_{XX} residual stress being the longitudinal, the stainless-steel result has more compression stress while the carbon steel was observed to be in

complex distribution between the inside and outside surfaces. But in general, tension areas are on the top and on the bottom of the printed part for both materials. On the other side, compression area is the central area of the printed part. Furthermore, the clamps on Y-axis and zero X-axis increase the rate of the tension stresses of the printed part, which is parallel to these clamps. So, for σ_{XX} residual stresses, the tension stress is focused around the base and the top of the printed part for both materials. In contrast, the middle area is in compression. In addition, the inside surface of the printed part tends to have the opposite properties of the stresses type of the outside surface. Also, the clamps must be tested for other conditions in order to identify their effects on residual stresses.

The second kind of stress, namely the First principle residual stresses, shows lesser complexity among the σ_{XX} residual stresses. For this kind of stress, the colorful contours show two different clear areas. One is a frame around the second which is usually in a high rate of tension stress, while the second area is one which appears to be of compression stress type with a low rate, as compared to the frame area. In comparison with the yield strength, the frame area is in a state close to the yielding strength. The internal area, which is surrounded by the frame area, has a very low value relative to the yielding strength. As a conclusion, for 3D printing using WAAM, the active useful area is surrounded by a frame of high residual stress area. So, it is useful to predict the stress distribution by employing simulation processes before the actual printing and machining processes. For both kinds of stresses, the base holds the printed part by tension residual stresses which increase the tension area inside the printed part.

Also, it has to be mentioned that the last three layers of the carbon steel sample have different stress types from the area below them.

The last point is that of the Z-axis displacement in both cases. For stainless steel the distortion is higher than that in carbon steel. In stainless steel it may reach twice the displacement of carbon steel, after the cooling processes. They are both distorted at the ends of the printing path, which is understandable, since the ends are held by the center area of the printed part. Also, stainless steel has a concave area in the middle of the sample, while in the carbon steel sample, this area looks like an arc.

For the computation time for the simulation processes in SYSWELD with a workstation has 16 GB as RAM and around 600 GB as storages, each case took at least 5 days to simulate the 3D printing processes as WAAM; and for the memory requirements, it needs more than 400 GB for the data and the result. For more accuracy by using finer mesh size, the requirements should be higher than the mentioned numbers.

Bottom line is that while the austenitic stainless-steel grade 316L sample has lower longitudinal and first principle residual stresses, low carbon steel S355J2G3 sample has higher longitudinal and first principle residual stresses. In addition, the austenitic stainless-steel grade 316L sample has higher Z-axis displacement, while low carbon steel S355J2G3 sample has the lower Z-axis displacement.

Chapter 4 Conclusion and future work

WAAM 3D printing is one of the promising technologies of the future. For reducing expenses related to such printing, simulation processes are a very effective in predicting the properties of the printed parts after the entire process is done. WAAM is considered as one of the lower priced 3D printers for metals.

It should, however, be noted that before fully trusting this above-mentioned simulation processes, the methodology should undergo several tests as mentioned in the second chapter - Heat test, Path test, Mesh test, Penetration test, and Clamping test. These tests determine the appropriate conditions to be employed in the simulation processes. SYSWELD is a commercial welding simulation software and has one of the higher computational ability among software packages used for welding. Since WAAM is essentially a welding process, adopting SYSWELD in 3D printing is highly recommended.

A 3D printed plate has been printed in Lehigh 3D lab and tested for fatigue. Therefore, in this thesis, for most of the parameters of this experimental sample, a simulation sample has been subject to comprehensive tests. The test results should be applicable to and the sample would represent a range of many similar materials. One of the main objectives of this thesis is to show the residual stresses types in color contour plots for comprehensiveness and clarity. As mentioned earlier, the simulation samples used were austenitic stainless-steel grade 316L and Low carbon steel S355J2G3 as materials for the 3D printing processes.

The primary result is to demonstrate Longitudinal residual stress (σ_{XX}) and First principle residual stresses. The main outcome for longitudinal residual stress (σ_{XX}) is that the austenitic stainless-steel grade 316L sample has lower rate than Low carbon steel S355J2G3, and in both cases there

are three main areas of stress types. The top and the bottom areas are in the same residual stress type, and the middle area contrasts with these areas. In both the materials' samples, the residual stress exceeds the yielding strength, but not tensile strength.

A main finding for the First principle residual stresses is that in both samples, for the materials, namely austenitic stainless-steel grade 316L and Low carbon steel S355J2G3, the residual stress made a frame of tension stress around the middle area. This meant that the boundaries of the plate have a different residual stress type than the middle area. As in the longitudinal residual stress, the First principle residual stress exceeds the yielding strength in certain spots. Also, it is higher in Low carbon steel S355J2G3 than in austenitic stainless-steel grade 316L.

Lastly, the Z-axis displacement is high in the austenitic stainless-steel grade 316L sample and it is low in other sample of Low carbon steel S355J2G3. The main reason for this is that the ductility of stainless steel is higher than that of carbon steel. This allows the residual stress to deform the samples.

The next step for this research is to validate and verify the simulation sample with an experimental sample for the identical properties of WAAM. This would contribute, in great measure, a high trust factor in the simulation exercise. Also, based on observations from the simulation sample, the residual stresses were very high; this provides a great opportunity to look for a solution to reduce them by using heat treatment or modifying welding parameters. And for effecting physical changes, the dimension of the base could change the value of the residual stresses. Besides the exhibited and proven effects of the clamps, other clamping conditions could also alter the behavior of residual stresses.

Reference

[1] J. Du, Z. Wei, X. Wang, X. Fang, and G. Zhao, “A novel high-efficiency methodology for metal additive manufacturing,” *Appl. Phys. A Mater. Sci. Process.*, vol. 122, no. 11, pp. 1–10, 2016.

[2] I. Gibson, D. Rosen, and B. Stucker, “Additive Manufacturing Technologies,” pp. 351–374, 2015.

[3] W. Gao *et al.*, “The status, challenges, and future of additive manufacturing in engineering,” *CAD Comput. Aided Des.*, vol. 69, pp. 65–89, 2015.

[4] L. Yang *et al.*, *Additive Manufacturing of Metals: The Technology, Materials, Design and Production*. 2017.

[5] P. A. Colegrove, “High deposition rate high quality metal addi- tive manufacture using wire + are technology,” 2010.

[6] J. Ding *et al.*, “Thermo-mechanical analysis of Wire and Arc Additive Layer Manufacturing process on large multi-layer parts,” *Comput. Mater. Sci.*, vol. 50, no. 12, pp. 3315–3322, 2011.

[7] T. Wohlers and T. Gornet, “History of additive manufacturing Introduction of non-SL systems Introduction of low-cost 3D printers,” *Wohlers Rep. 2012*, pp. 1–23, 2012.

[8] D. Bourell *et al.*, “Materials for additive manufacturing,” *CIRP Ann. - Manuf. Technol.*, vol. 66, no. 2, pp. 659–681, 2017.

[9] Y. Zhai, D. A. Lados, and J. L. Lagoy, “Additive Manufacturing: Making imagination the major Limitation,” *Jom*, vol. 66, no. 5, pp. 808–816, 2014.

[10] B. A. Szost *et al.*, “A comparative study of additive manufacturing techniques: Residual stress and microstructural analysis of CLAD and WAAM printed Ti-6Al-4V components,” *Mater. Des.*, vol. 89, pp. 559–567, 2016.

[11] J. Ding, P. Colegrove, J. Mehnen, S. Williams, F. Wang, and P. S. Almeida, “A computationally efficient finite element model of wire and arc additive manufacture,” *Int. J. Adv. Manuf. Technol.*, vol. 70, no. 1–4, pp. 227–236, 2014.

[12] A. Busachi, J. Erkoyuncu, P. Colegrove, F. Martina, C. Watts, and R. Drake, “A review of Additive Manufacturing technology and Cost Estimation techniques for the defence sector,” *CIRP J. Manuf. Sci. Technol.*, vol. 19, pp. 117–128, 2017.

[13] D. Yang, C. He, and G. Zhang, “Forming characteristics of thin-wall steel parts by double electrode GMAW based additive manufacturing,” *J. Mater. Process. Technol.*, vol. 227, pp. 153–160, 2016.

[14] M. Seifi, A. Salem, J. Beuth, O. Harrysson, and J. J. Lewandowski, “Overview of Materials Qualification Needs for Metal Additive Manufacturing,” *Jom*, vol. 68, no. 3, pp. 747–764, 2016.

[15] D. Ding, Z. Pan, C. Dominic, and H. Li, “Robotic Welding, Intelligence and Automation,” vol. 88, 2011.

[16] C. Dordlofva, A. Lindwall, and P. Törlind, “Opportunities and Challenges for Additive Manufacturing in Space Applications,” *Proc. Nord. 2016*, 2016.

[17] H. Bikas, P. Stavropoulos, and G. Chryssolouris, “Additive manufacturing methods and modeling approaches: A critical review,” *Int. J. Adv. Manuf. Technol.*, vol. 83, no. 1–4, pp. 389–405, 2016.

[18] D. Ding, Z. Pan, D. Cuiuri, and H. Li, “A tool-path generation strategy for wire and arc additive manufacturing,” *Int. J. Adv. Manuf. Technol.*, vol. 73, no. 1–4, pp. 173–183, 2014.

[19] J. Ruan, T. E. Sparks, Z. Fan, J. K. Stroble, and A. Panackal, “No Title,” pp. 233–245.

[20] X. Bai, H. Zhang, and G. Wang, “Improving prediction accuracy of thermal analysis for weld-based additive manufacturing by calibrating input parameters using IR imaging,” *Int. J. Adv. Manuf. Technol.*, vol. 69, no. 5–8, pp. 1087–1095, 2013.

[21] N. Guo and M. C. Leu, “Additive manufacturing: Technology, applications and research needs,” *Front. Mech. Eng.*, vol. 8, no. 3, pp. 215–243, 2013.

[22] T. Abe and H. Sasahara, “Dissimilar metal deposition with a stainless steel and nickel-based alloy using wire and arc-based additive manufacturing,” *Precis. Eng.*, vol. 45, pp. 387–395, 2016.

[23] C. M. Lee, W. S. Woo, J. T. Baek, and E. J. Kim, “Laser and arc manufacturing processes: A review,” *Int. J. Precis. Eng. Manuf.*, vol. 17, no. 7, pp. 973–985, 2016.

[24] J. Džugan and Z. Nový, “Powder Application in Additive Manufacturing of Metallic Parts,” L. A. B. T.-P. M.-F. and C. S. Dobrzanski, Ed. Rijeka: InTech, 2017, p. Ch. 08.

[25] M. Megahed, H.-W. Mindt, N. N’Dri, H. Duan, and O. Desmaison, *Metal additive-manufacturing process and residual stress modeling*, vol. 5, no. 1. Integrating Materials and Manufacturing Innovation, 2016.

[26] J. J. Yan *et al.*, “Selective laser melting of H13: microstructure and residual stress,” *J. Mater. Sci.*, vol. 52, no. 20, pp. 12476–12485, 2017.

[27] Z. Fan and F. Liou, “Numerical Modeling of the Additive Manufacturing (AM) Processes of Titanium Alloy,” *Titan. Alloy. - Towar. Achiev. Enhanc. Prop. Divers. Appl.*, no. March 2015, 2012.

[28] D. Ding, Z. Pan, D. Cuiuri, and H. Li, “A multi-bead overlapping model for robotic wire and arc additive manufacturing (WAAM),” *Robot. Comput. Integr. Manuf.*, vol. 31, pp. 101–110, 2015.

[29] Y. Ma, D. Cuiuri, N. Hoye, H. Li, and Z. Pan, “Effects of wire feed conditions on in situ alloying and additive layer manufacturing of titanium aluminides using gas tungsten arc welding,” *J. Mater. Res.*, vol. 29, no. 17, pp. 2066–2071, 2014.

[30] Z. Pan, D. Ding, B. Wu, and D. Cuiuri, “Arc Welding Processes for Additive Manufacturing: A Review,” no. 2, pp. 3–24, 2018.

[31] W. J. Sames, F. A. List, S. Pannala, R. R. Dehoff, and S. S. Babu, “The metallurgy and processing science of metal additive manufacturing,” *Int. Mater. Rev.*, vol. 61, no. 5, pp. 315–360, 2016.

[32] Y. Zhang *et al.*, “Additive Manufacturing of Metallic Materials: A Review,” *J. Mater. Eng. Perform.*, vol. 27, no. 1, 2018.

[33] M. J. Bermingham, D. Kent, H. Zhan, D. H. Stjohn, and M. S. Dargusch, “Controlling the microstructure and properties of wire arc additive manufactured Ti-6Al-4V with trace boron additions,” *Acta Mater.*, vol. 91, pp. 289–303, 2015.

[34] D. Ding, Z. Pan, D. Cuiuri, and H. Li, “Wire-feed additive manufacturing of metal components: technologies, developments and future interests,” *Int. J. Adv. Manuf. Technol.*, vol. 81, no. 1–4, pp. 465–481, 2015.

[35] D. Herzog, V. Seyda, E. Wycisk, and C. Emmelmann, “Additive manufacturing of metals,” *Acta Mater.*, vol. 117, pp. 371–392, 2016.

[36] C. Shen, Z. Pan, D. Cuiuri, J. Roberts, and H. Li, “Fabrication of Fe-FeAl Functionally Graded Material Using the Wire-Arc Additive Manufacturing Process,” *Metall. Mater. Trans. B*, vol. 47, no. 1, pp. 763–772, 2016.

[37] O. Yilmaz and A. A. Ugla, “Development of a cold wire-feed additive layer manufacturing system using shaped metal deposition method,” *J. Mech. Sci. Technol.*, vol. 31, no. 4, pp. 1611–1620, 2017.

[38] F. Montevecchi, G. Venturini, A. Scippa, and G. Campatelli, “Finite Element Modelling of Wire-arc-additive-manufacturing Process,” *Procedia CIRP*, vol. 55, pp. 109–114, 2016.

[39] H. Geng, J. Xiong, D. Huang, X. Lin, and J. Li, “A prediction model of layer geometrical size in wire and arc additive manufacture using response surface methodology,” *Int. J. Adv. Manuf. Technol.*, vol. 93, no. 1–4, pp. 175–186, 2017.

[40] J. Donoghue, A. A. Antonysamy, F. Martina, P. A. Colegrove, S. W. Williams, and P. B. Prangnell, “The effectiveness of combining rolling deformation with Wire-Arc Additive Manufacture on β-grain refinement and texture modification in Ti-6Al-4V,” *Mater. Charact.*, vol. 114, pp. 103–114, 2016.

[41] F. Xu *et al.*, “Multi-Sensor System for Wire-Fed Additive Manufacture of Titanium Alloys,” *26th Int. Conf. Flex. Autom. Intell. Manuf. (FAIM 2016)*, no. January 2017, p. Article in Press, 2016.

[42] G. Venturini, F. Montevecchi, A. Scippa, and G. Campatelli, “Optimization of WAAM Deposition Patterns for T-crossing Features,” *Procedia CIRP*, vol. 55, pp. 95–100, 2016.

[43] J. Xiong, Z. Yin, and W. Zhang, “Forming appearance control of arc striking and extinguishing area in multi-layer single-pass GMAW-based additive manufacturing,” *Int. J. Adv. Manuf. Technol.*, vol. 87, no. 1–4, pp. 579–586, 2016.

[44] J. Gockel and J. Beuth, “Understanding Ti-6Al-4V Microstructure Control in Additive Manufacturing via Process Maps Joy Gockel and Jack Beuth Department of Mechanical Engineering, Carnegie Mellon University, Pittsburgh, PA 15213,” *Solid Free. Fabr. Proc.*, pp.

666–674, 2013.

[45] G. Manogharan, B. Yelamanchi, R. Aman, and Z. Mahbooba, “Experimental Study of Disruption of Columnar Grains During Rapid Solidification in Additive Manufacturing,” *Jom*, vol. 68, no. 3, pp. 842–849, 2016.

[46] Y. Liu, Y. Yang, and D. Wang, “A study on the residual stress during selective laser melting (SLM) of metallic powder,” *Int. J. Adv. Manuf. Technol.*, pp. 1–10, 2016.

[47] Sarah Saunders, “After Successful Testing and Verification, 3D Printed WAAMpeller is Introduced to the Public,” 2017. [Online]. Available: https://3dprint.com/195791/3d-printed-waampeller-verified/.

[48] A. Busachi, J. Erkoyuncu, P. Colegrove, F. Martina, and J. Ding, “Designing a WAAM based manufacturing system for defence applications,” *Procedia CIRP*, vol. 37, no. 2013, pp. 48–53, 2015.

[49] A. Haboudou, P. Peyre, A. B. Vannes, and G. Peix, “Reduction of porosity content generated during Nd: YAG laser welding of A356 and AA5083 aluminium alloys,” *Mater. Sci. Eng. A*, vol. 363, no. 1–2, pp. 40–52, 2003.

[50] S. W. Williams, F. Martina, A. C. Addison, J. Ding, G. Pardal, and P. Colegrove, “Wire + Arc Additive Manufacturing,” *Mater. Sci. Technol.*, vol. 32, no. 7, pp. 641–647, 2016.

[51] J. Y. Bai, C. L. Yang, S. B. Lin, B. L. Dong, and C. L. Fan, “Mechanical properties of 2219-Al components produced by additive manufacturing with TIG,” *Int. J. Adv. Manuf. Technol.*, vol. 86, no. 1–4, pp. 479–485, 2016.

[52] PandeyM. and Pulak, “Rapid prototyping technologies, applications and part deposition planning,” *Retrieved Oct.*, no. June, p. 15, 2010.

[53] X. Zhou and C. Liu, “Three-dimensional Printing for Catalytic Applications: Current Status and Perspectives,” *Adv. Funct. Mater.*, vol. 1701134, p. 1701134, 2017.

[54] W. World, L. E. Soudage, D. Le, T. Guwahati, and T. Bombay, “In Fusion Welding Process Simulation EFFICIENT ESTIMATION OF VOLUMETRIC HEAT SOURCE IN FUSION WELDING PROCESS SIMULATION,” vol. 56, no. January 2016, pp. 88–97, 2013.

[55] P. Pratt, S. D. Felicelli, L. Wang, and C. R. Hubbard, “Residual stress measurement of laser-engineered net shaping AISI 410 thin plates using neutron diffraction,” *Metall. Mater. Trans. A Phys. Metall. Mater. Sci.*, vol. 39, no. 13, pp. 3155–3163, 2008.

[56] T. Kik, M. Slovacek, J. Moravec, and M. Vanek, “Numerical Simulations of Heat Treatment Processes,” *Appl. Mech. Mater.*, vol. 809–810, pp. 799–804, 2015.

[57] M. Moradi Eshkafti, “Influence of various welding sequence schemes on the load bearing capacity of square hollow section T-joint.,” vol. 35, no. 4, pp. 41–50, 2017.

[58] C. V. Haden, G. Zeng, F. M. Carter, C. Ruhl, B. A. Krick, and D. G. Harlow, “Wire and arc additive manufactured steel: Tensile and wear properties,” *Addit. Manuf.*, vol. 16, pp. 115–123, 2017.

[59] V. M. J. Varghese, M. R. Suresh, and D. S. Kumar, “Recent developments in modeling of

heat transfer during TIG welding—a review," *Int. J. Adv. Manuf. Technol.*, vol. 64, no. 5–8, pp. 749–754, 2013.

[60] D. Deng and H. Murakawa, "Numerical simulation of temperature field and residual stress in multi-pass welds in stainless steel pipe and comparison with experimental measurements," *Comput. Mater. Sci.*, vol. 37, no. 3, pp. 269–277, 2006.

[61] G. Casalino and A. D. Ludovico, "Finite element simulation of high speed pulse welding of high specific strength metal alloys," *J. Mater. Process. Technol.*, vol. 197, no. 1–3, pp. 301–305, 2008.

[62] S. Murugan, S. Rai, and P. Kumar, "Temperature distribution and residual stresses due to multipass welding in type 304 stainless steel and low carbon steel weld pads," *Int. J. …*, vol. 78, no. 4, pp. 307–317, 2001.

[63] R. K. Chin, J. L. Beuth, and C. H. Amon, "Successive deposition of metals in solid freeform fabrication processes, Part 1: thermomechanical models of layers and droplet columns," *J. Manuf. Sci. Eng.*, vol. 123, no. 4, pp. 623–631, 2001.

[64] R. K. Chin, J. L. Beuth, and C. H. Amon, "Successive Deposition of Metals in Solid Freeform Fabrication Processes, Part 2: Thermomechanical Models of Adjacent Droplets," *J. Manuf. Sci. Eng.*, vol. 123, no. 4, pp. 632–638, May 2000.

[65] J. Mehnen, J. Ding, H. Lockett, and P. Kazanas, "Global Product Development," pp. 721–727, 2011.

[66] D. Yang, G. Wang, and G. Zhang, "Thermal analysis for single-pass multi-layer GMAW based additive manufacturing using infrared thermography," *J. Mater. Process. Technol.*, vol. 244, pp. 215–224, 2017.

[67] S. Suryakumar, K. P. Karunakaran, U. Chandrasekhar, and M. A. Somashekara, "A study of the mechanical properties of objects built through weld-deposition," *Proc. Inst. Mech. Eng. Part B J. Eng. Manuf.*, vol. 227, no. 8, pp. 1138–1147, 2013.

[68] M. P. Mughal, H. Fawad, and R. A. Mufti, "Three-dimensional finite-element modelling of deformation in weld-based rapid prototyping," *Proc. Inst. Mech. Eng. Part C J. Mech. Eng. Sci.*, vol. 220, no. 6, pp. 875–885, 2006.

[69] P. A. Colegrove *et al.*, "Microstructure and residual stress improvement in wire and arc additively manufactured parts through high-pressure rolling," *J. Mater. Process. Technol.*, vol. 213, no. 10, pp. 1782–1791, 2013.

[70] J. Ding, "Thermo-mechanical Analysis of Wire and Arc Additive Manufacturing Process," no. January, p. 216, 2012.

[71] X. Qiu, "Effect of rolling on fatigue crack growth rate of Wire and Arc Additive Manufacture (WAAM) processed Titanium," no. November, pp. 2012–2013, 2013.

[72] Z. Feng, *Processes and mechanisms of welding residual stress and distortion*. Elsevier, 2005.

[73] P. Staron, M. Koçak, S. Williams, and A. Wescott, "Residual stress in friction stir-welded A1 sheets," *Phys. B Condens. Matter*, vol. 350, no. 1–3 SUPPL. 1, pp. 491–493, 2004.

[74] D. A. Price *et al.*, “Distortion control in welding by mechanical tensioning,” *Sci. Technol. Weld. Join.*, vol. 12, no. 7, pp. 620–633, 2007.

[75] J. Altenkirch, A. Steuwer, P. J. Withers, S. W. Williams, M. Poad, and S. W. Wen, “Residual stress engineering in friction stir welds by roller tensioning,” *Sci. Technol. Weld. Join.*, vol. 14, no. 2, pp. 185–192, 2009.

[76] S. W. Wen, P. A. Colegrove, S. W. Williams, S. A. Morgan, A. Wescott, and M. Poad, “Rolling to control residual stress and distortion in friction stir welds,” *Sci. Technol. Weld. Join.*, vol. 15, no. 6, pp. 440–447, 2010.

[77] C. L. Tsai, S. C. Park, and W. T. Cheng, “Welding Distortion of a Thin-Plate Panel Structure,” *Am. Weld. Soc. - Weld. J.*, no. May, pp. 156–165, 1999.

[78] T. L. Teng, P. H. Chang, and W. C. Tseng, “Effect of welding sequences on residual stresses,” *Comput. Struct.*, vol. 81, no. 5, pp. 273–286, 2003.

[79] I. Sattari-Far and Y. Javadi, “Influence of welding sequence on welding distortions in pipes,” *Int. J. Press. Vessel. Pip.*, vol. 85, no. 4, pp. 265–274, 2008.

[80] Y. A. Song, S. Park, and S. W. Chae, “3D welding and milling: Part II - Optimization of the 3D welding process using an experimental design approach,” *Int. J. Mach. Tools Manuf.*, vol. 45, no. 9, pp. 1063–1069, 2005.

[81] A. H. Nickel, D. M. Barnett, and F. B. Prinz, “Thermal stresses and deposition patterns in layered manufacturing,” *Mater. Sci. Eng. A*, vol. 317, no. 1–2, pp. 59–64, 2001.

[82] M. P. Mughal, R. A. Mufti, and H. Fawad, “The mechanical effects of deposition patterns in welding-based layered manufacturing,” *Proc. Inst. Mech. Eng. Part B J. Eng. Manuf.*, vol. 221, no. 10, pp. 1499–1509, 2007.

[83] M. V. Deo and P. Michaleris, “Mitigation of welding induced buckling distortion using transient thermal tensioning,” *Sci. Technol. Weld. Join.*, vol. 8, no. 1, pp. 49–54, 2003.

[84] N. W. Klingbeil, J. L. Beuth, R. K. Chin, and C. H. Amon, “Residual stress-induced warping in direct metal solid freeform fabrication,” *Int. J. Mech. Sci.*, vol. 44, no. 1, pp. 57–77, 2002.

[85] R. Jendrzejewski, G. Śliwiński, M. Krawczuk, and W. Ostachowicz, “Temperature and stress fields induced during laser cladding,” *Comput. Struct.*, vol. 82, no. 7–8, pp. 653–658, 2004.

[86] P. Michaleris and A. Debiccari, “Prediction of welding distortion,” *Am. Weld. Soc. - Weld. J.*, vol. 76, no. April, p. 172–s, 1997.

[87] K. Masubuchi, *Analysis of welded structures: residual stresses, distortion, and their consequences*, vol. 33. Elsevier, 2013.

[88] K. Li, J. Chen, and Y. Zhang, “Double-electrode GMAW process and control,” *Weld. J.*, pp. 231–237, 2007.

[89] K. H. Li and Y. M. Zhang, “Consumable Double-Electrode GMAW — Part l : The Process,” *Weld. J.*, vol. 87, no. January, p. 11s–17s, 2008.

[90] K. Li and Y. M. Zhang, “Consumable Double-Electrode GMAW Part II: Monitoring, Modeling, and Control,” *Control*, pp. 1–34, 2007.

[91] Y. M. Zhang, M. Jiang, and W. Lu, “Double electrodes improve GMAW heat input control,” *Weld. J.*, vol. 83, no. 11, pp. 39–41, 2004.

[92] X. Bai, H. Zhang, and G. Wang, “Modeling of the moving induction heating used as secondary heat source in weld-based additive manufacturing,” *Int. J. Adv. Manuf. Technol.*, vol. 77, no. 1–4, pp. 717–727, 2015.

[93] P. Mercelis and J. Kruth, “Residual stresses in selective laser sintering and selective laser melting,” *Rapid Prototyp. J.*, vol. 12, no. 5, pp. 254–265, 2006.

[94] H. Zhao, G. Zhang, Z. Yin, and L. Wu, “A 3D dynamic analysis of thermal behavior during single-pass multi-layer weld-based rapid prototyping,” *Journal of Materials Processing Technology*, vol. 211, no. 3. 2011.

[95] H. Zhao, G. Zhang, Z. Yin, and L. Wu, “Three-dimensional finite element analysis of thermal stress in single-pass multi-layer weld-based rapid prototyping,” *J. Mater. Process. Technol.*, vol. 212, no. 1, pp. 276–285, 2012.

[96] M. P. Mughal, H. Fawad, R. A. Mufti, and M. Siddique, “Deformation modelling in layered manufacturing of metallic parts using gas metal arc welding: effect of process parameters,” *Model. Simul. Mater. Sci. Eng.*, vol. 13, no. 7, p. 1187, 2005.

[97] M. P. Mughal, H. Fawad, and R. Mufti, “Finite element prediction of thermal stresses and deformations in layered manufacturing of metallic parts,” *Acta Mech.*, vol. 183, no. 1–2, pp. 61–79, 2006.

[98] J. D. Spencer, P. M. Dickens, and C. M. Wykes, “Rapid prototyping of metal parts by three-dimensional welding,” *Proc. Inst. Mech. Eng. Part B J. Eng. Manuf.*, vol. 212, no. 3, pp. 175–182, 1998.

[99] J. Fessler, R. Merz, A. Nickel, F. Prinz, and L. Weiss, “Laser deposition of metals for shape deposition manufacturing,” *Solid Free. Fabr. Symp. Proceedings, Univ. Texas Austin*, pp. 117–124, 1996.

[100] R. Jendrzejewski and G. Śliwiński, “Investigation of temperature and stress fields in laser cladded coatings,” *Appl. Surf. Sci.*, vol. 254, no. 4, pp. 921–925, 2007.

[101] L. Costa, R. Vilar, T. Reti, and A. M. Deus, “Rapid tooling by laser powder deposition: Process simulation using finite element analysis,” *Acta Mater.*, vol. 53, no. 14, pp. 3987–3999, 2005.

[102] E. R. Denlinger, J. C. Heigel, P. Michaleris, and T. A. Palmer, “Effect of inter-layer dwell time on distortion and residual stress in additive manufacturing of titanium and nickel alloys,” *J. Mater. Process. Technol.*, vol. 215, pp. 123–131, 2015.

[103] W. C. Spencer DJ, Dickens PM, “Rapid prototyping of metal parts by three dimentional welding,” *Mech E J. Eng. Manuf.*, vol. 212, pp. 175–182, 1998.

[104] J. Xiong, G. Zhang, Z. Qiu, and Y. Li, “Vision-sensing and bead width control of a single-bead multi-layer part: Material and energy savings in GMAW-based rapid manufacturing,” *J. Clean. Prod.*, vol. 41, pp. 82–88, 2013.

[105] J. Xiong and G. Zhang, “Adaptive control of deposited height in GMAW-based layer

additive manufacturing," *J. Mater. Process. Technol.*, vol. 214, no. 4, pp. 962–968, 2014.

[106] Y. M. Zhang, P. Li, Y. Chen, and A. T. Male, "Automated system for welding-based rapid prototyping," *Mechatronics*, vol. 12, no. 1, pp. 37–53, 2002.

[107] Y. M. Zhang, Y. Chen, P. Li, and A. T. Male, "Weld deposition-based rapid prototyping: A preliminary study," *J. Mater. Process. Technol.*, vol. 135, no. 2–3 SPEC., pp. 347–357, 2003.

[108] Y. A. Song and S. Park, "Experimental investigations into rapid prototyping of composites by novel hybrid deposition process," *J. Mater. Process. Technol.*, vol. 171, no. 1, pp. 35–40, 2006.

[109] X. W. Bai, H. O. Zhang, and G. L. Wang, "Electromagnetically confined weld-based Additive Manufacturing," *Procedia CIRP*, vol. 6, pp. 515–520, 2013.

[110] J. V. Gordon, C. V. Haden, H. F. Nied, R. P. Vinci, and D. G. Harlow, "Fatigue crack growth anisotropy, texture and residual stress in austenitic steel made by wire and arc additive manufacturing," *Mater. Sci. Eng. A*, vol. 724, no. March, pp. 431–438, 2018.

Vita

Abdulrahman Alrumayh is born in Unaizah, Saudi Arabia on January 2nd, 1991. He is the third son for his parents Amer and Ruqayyah.

He received a bachelor's degree from Qassim University in 2014, and he started his master program in Lehigh University in January 2017.